

# Important Notice

This copy may be used only for the purposes of research and private study, and any use of the copy for a purpose other than research or private study may require the authorization of the copyright owner of the work in question. Responsibility regarding questions of copyright that may arise in the use of this copy is assumed by the recipient.

UNIVERSITY OF CALGARY

Model-based inversion of broadband seismic data

by

Patricia Esperanza Gavotti

A THESIS

SUBMITTED TO THE FACULTY OF GRADUATE STUDIES  
IN PARTIAL FULFILMENT OF THE REQUIREMENTS FOR THE  
DEGREE OF MASTER OF SCIENCE

DEPARTMENT OF GEOSCIENCE

CALGARY, ALBERTA

JANUARY, 2014

© Patricia Gavotti 2014

## **Abstract**

Three study cases were used to evaluate the influence of broadband seismic data in inversion studies. In the first case, seismic data recorded in the Hussar Experiment showed the advantage of preserving the low-frequency component from acquisition through data processing. Processing performed on data from the Project Pioneer, proved the importance of taking special care of noise attenuation processes. The radial filter demonstrated to be useful in suppressing coherent noise while retaining low-frequency signal. In both cases, lateral variation in the inversion results are associated to the presence of low-frequency signal in the seismic data suggesting that the seismic reflections are controlling the impedance response. In the third study, 2D seismic modelling was performed to simulate the CO<sub>2</sub> injection scenario in the Nisku Formation in the Wabamun area. A decrease in the impedance values of ~7% is observed in the post-injection scenario and the identification of the CO<sub>2</sub> plume is more evident in the inverted result than in stacked section.

## **Acknowledgements**

I would like to thank my supervisor, Dr. Don C. Lawton, for all his guidance and support during my M.Sc. Program. I am immensely grateful for having the opportunity of working with him and, especially for his knowledge and positivism.

Thanks to all CREWES professors and staff for their support during my journey within this extraordinary research group. Thanks to Dr. Larry Lines for his encouraging words and availability. Special thanks to Helen Isaac for all the help during the seismic processing of this thesis. Also, thanks to Dave Henley for helping me understanding the radial filter and Gabor deconvolution processes. Many thanks to Kevin Hall and Rolf Maier for helping me with several technical issues. Thanks to Kevin Bertram and Malcom Bertram for their willingness and patience in teaching us seismic acquisition programs. Thanks to Laura Baird for her great administrative work and for her unconditional support.

Thanks to my CREWES fellows Shahin Moradi and Raul Cova for helping me with the modelling software, and clarifying me some processing doubts. Also, thanks to Shahin Jabbari, Babatunde Arenrin, Rafael Asuaje, Michelle Montano, Samuel Aquino, Nisael Solano, Liliana Zuleta, Faranak Mahmoudian, Mahdi Almutlaq, Virginia Vera, Liliana Zambrano, Thais Guirigay, Steve Kim, Heather Lloyd, Andrew Nicol, Byron Kelly and Jessie Arthur for their collaboration during my stay at U of C. I am grateful of

meeting such a wonderful and smart people that made my graduate school experience interesting and fun!

Special thanks to CREWES sponsors and Carbon Management Canada (CMC) for their financial support. Thanks to TransAlta Corporation and Schlumberger for providing the data, Landmark Graphics Corporation, Norsar-2D and Hampson-Russell for providing the software used in this thesis.

Special thanks to Dr. Brian Russell for valuable discussions about seismic inversion and for his kindness. I feel proud to consider him a friend.

Finally, thanks to my family for their unconditional support in every decision I have made in my life including moving abroad to pursue a better future.

## **Dedication**

*To my family: Velia Duque (mom), Eduardo Gavotti (dad), my siblings (Luis, Velia, Claudia, Eduardo (Bebo), Jesus Eduardo and Jaqueline), and my nephews (Maite, Mouhibe, Feryal, Santiago y Samuel).*

## Table of Contents

|  |      |
|--|------|
| Abstract .....   | ii   |
| Acknowledgements .....   | iii  |
| Dedication .....   | v    |
| Table of Contents .....  | vi   |
| List of Tables .....   | viii |
| List of Figures and Illustrations .....  | ix   |
| List of Symbols, Abbreviations and Nomenclature .....  | xvii |
| <br>   |      |
| CHAPTER 1: INTRODUCTION .....  | 1    |
| 1.1 Seismic Inversion and Applications .....   | 1    |
| 1.1.1 Method Description .....   | 1    |
| 1.1.2 Seismic Inversion as a Monitoring Technique in CO <sub>2</sub> Sequestration<br>Programs ..... | 8    |
| 1.2 Area of Study .....  | 12   |
| 1.2.1 Hussar Experiment Location .....   | 12   |
| 1.4 Thesis Objectives: .....   | 13   |
| 1.5 Thesis Outline: .....  | 15   |
| 1.6 Software: .....  | 16   |
| <br>   |      |
| CHAPTER 2: THE HUSSAR EXPERIMENT .....   | 17   |
| 2.1 The Hussar Experiment Overview .....   | 17   |
| 2.1.1 Introduction .....   | 17   |
| 2.1.2 Geology Overview .....   | 17   |
| 2.2 Hussar Experiment Data .....   | 21   |
| 2.2.1 Seismic Processing Considerations .....  | 25   |
| 2.2.2 Vertical Resolution .....  | 26   |
| 2.2.3 Cross plot Analysis .....  | 27   |
| 2.2.4 Seismic-Well Ties .....  | 29   |
| 2.3 Model-based Inversion .....  | 33   |
| 2.3.1 The Initial Model .....  | 33   |
| 2.3.2 Inversion Analysis .....   | 35   |
| 2.3.3 Inversion Results .....  | 45   |
| 2.4 Summary .....  | 47   |
| <br>   |      |
| CHAPTER 3: NISKU SEISMIC DATA .....  | 49   |
| 3.1 Wabamun Area CO <sub>2</sub> Sequestration Project Overview .....                                | 49   |
| 3.1.1 Introduction .....   | 49   |
| 3.1.2 Geology Overview .....   | 50   |
| 3.2 2D Seismic Data: Highvale and Violet Grove .....   | 54   |
| 3.2.1 Project Pioneer Data .....   | 54   |
| 3.2.2 Survey Data .....  | 56   |
| 3.2.3 2D Seismic Processing .....  | 58   |

|   |     |
|---|-----|
| 3.3 Highvale Seismic Inversion .....                      | 72  |
| 3.3.1 Introduction: .....                                 | 72  |
| 3.3.2 Well Log Analysis .....                             | 74  |
| 3.3.3 Initial Model for Inversion .....                   | 81  |
| 3.3.4 Inversion Analysis .....                            | 83  |
| 3.3.5 Inversion Results .....                             | 86  |
| 3.4 Discussion .....                                      | 90  |
| <br>  |     |
| CHAPTER 4: 2D SEISMIC MODELLING .....                     | 92  |
| 4.1 Introduction .....                                    | 92  |
| 4.2 2D Geological Modelling .....                         | 92  |
| 4.3 CO <sub>2</sub> Plume Simulation .....                | 94  |
| 4.4 2D Seismic Modelling .....                            | 97  |
| 4.5 2D Seismic Monitoring Results .....                   | 101 |
| 4.5.1 Seismic Amplitudes Direct Comparison: .....         | 101 |
| 4.5.2 Impedance Comparison after Seismic Inversion: ..... | 103 |
| 4.6 Discussion .....                                      | 111 |
| <br>  |     |
| CHAPTER 5: CONCLUSIONS .....                              | 113 |
| 5.1 Conclusions .....                                     | 113 |
| 5.2 Recommendations .....                                 | 115 |
| <br>  |     |
| REFERENCES .....  | 117 |

## List of Tables

|  |    |
|--|----|
| Table 3.1: 2D seismic lines main parameters .....  | 55 |
| Table 3.2: Processing flow applied to the seismic lines Highvale and Violet Grove .....  | 58 |
| Table 3.3: Physical properties of the Nisku Formation in the Wabamun Area. The values with an asterisk (*) were obtained from the Well 8-17. ....  | 76 |
| Table 4.1: Geological model parameters. The target formation is indicated in red.....  | 93 |
| Table 4.2: Velocities and density values of the CO <sub>2</sub> plume. The percentages change was obtained from the Gassmann fluid substitution analysis performed by Alshail (2011). .... | 97 |

## List of Figures and Illustrations

|   |    |
|---|----|
| Figure 1.1: Comparison of a sonic log with its corresponding series of reflection and resulting synthetic seismogram to illustrate the effect of bandwidth reduction on seismic signals (Lindseth, 1979: <a href="http://dx.doi.org/10.1190/1.1440922">http://dx.doi.org/10.1190/1.1440922</a> ). .....   | 3  |
| Figure 1.2: Illustration of missing low-frequency components in synthetic sonic logs obtained from inverting seismic data. A sonic log may be considered as a low-frequency function modulated by a higher-frequency function. The low-frequency part can be used in the initial guess (Lindseth, 1979: <a href="http://dx.doi.org/10.1190/1.1440922">http://dx.doi.org/10.1190/1.1440922</a> ). .....  | 4  |
| Figure 1.3: Comparison of the three post-stack inversion methods: a) band-limited, b) sparse-spike, and c) model-based (modified from STRATA user guide, 2009).....   | 5  |
| Figure 1.4: Project Pioneer Carbon Storage illustration. CO <sub>2</sub> generated in a coal-fired power plant station could have been injected in the Niku saline Formation and sealed by the Calmar Formation cap rock (modified from Project Pioneer, 2013: <a href="http://www.transalta.com/sites/default/files/Project%20Pioneer_Final%20Report_Executive%20Summary_2013.pdf">http://www.transalta.com/sites/default/files/Project%20Pioneer_Final%20Report_Executive%20Summary_2013.pdf</a> ). ..... | 9  |
| Figure 1.5: Location of study areas in Alberta, Canada. Hussar Experiment (yellow star) and Project Pioneer (green star) (modified from Natural Resources Canada, 2013: <a href="http://atlas.nrcan.gc.ca/site/english/maps/reference/provinceterritories/alberta">http://atlas.nrcan.gc.ca/site/english/maps/reference/provinceterritories/alberta</a> ). ...  | 13 |
| Figure 2.1: Stratigraphic column of the Mannville Group in Central Alberta. The red star indicates the target formation (modified from Core Lab Petroleum Services, 2012: <a href="http://www.landman.ca/pdf/CORELAB.pdf">http://www.landman.ca/pdf/CORELAB.pdf</a> ). .....  | 18 |
| Figure 2.2: Cross-section of the Mannville Group in Central Alberta showing the main stratigraphic units (modified from Mossop and Shetsen, 1994). .....  | 20 |
| Figure 2.3: Location of the seismic line with the well locations nearby (modified from Margrave et al., 2012). .....  | 21 |
| Figure 2.4: 10 Hz dynamite Hussar migrated section with wells 14-35, 14-27 and 12-27. The amplitude spectrum of the unfiltered seismic data is also shown, with energy down to 4 Hz. ....   | 22 |
| Figure 2.5: Well 14-35. The blue rectangle highlights the Glauconitic Formation characterised with low values of gamma ray (GR), density, V <sub>P</sub> and Z <sub>P</sub> logs. ....  | 23 |
| Figure 2.6: Well 14-27. The blue rectangle highlights the Glauconitic Formation characterised with low values of gamma ray (GR), density and V <sub>P</sub> logs. ....  | 24 |

|   |    |
|---|----|
| Figure 2.7: Well 12-27. The blue rectangle highlights the Glauconitic Formation.....  | 25 |
| Figure 2.8: Minimum bed thickness calculation based on Rayleigh's criterion where $Z$ is the minimum thickness, $V_P$ is the P-wave interval velocity, $f_d$ is the dominant frequency, $t_p$ is the P-wave travel time and $T$ is the wavelength period. ....  | 26 |
| Figure 2.9: Cross-plot $V_P$ vs. $V_S$ (Color: GR) in well 12-27. The red polygon highlights the Glauconitic Formation with high values for $V_S$ and relatively high values for $V_P$ (~3700-4300 m/s). ....   | 27 |
| Figure 2.10: Cross-plot $Z_P$ vs. $Z_S$ (Color: GR) in well 12-27. The red polygon highlights the Glauconitic Formation with relatively high values for both, $Z_P$ and $Z_S$ (~ $9 \times 10^6$ and $5 \times 10^6$ m/s*kg/m <sup>3</sup> respectively).....   | 28 |
| Figure 2.11: Cross-plot $V_P$ vs. $V_P/V_S$ ratio (Color: GR) in well 12-27. The red polygon highlights the Glauconitic Formation with $V_P$ values > 3500 m/s and $V_P/V_S$ values < 1.8. ....   | 28 |
| Figure 2.12: Cross-plot $V_P/V_S$ vs. GR (Color: $\lambda_p$ ) in well 12-27. The red polygon highlights the porous Glauconitic Formation with low values for $V_P/V_S$ and GR. ..  | 29 |
| Figure 2.13: Multi-well wavelet extracted from wells 14-27 and 14-35 with its amplitude spectrum. The dotted line indicates the average phase of the wavelet. ...   | 31 |
| Figure 2.14: Final tie of well 12-27 with the multi-well wavelet. Blue traces represent the synthetic seismogram; red traces represent the extracted trace from the seismic data at the well location, and black traces shows the ten traces around the well location. Yellow bars show the correlation window..... | 31 |
| Figure 2.15: Final tie of well 14-27 with the multi-well wavelet. Blue traces represent the synthetic seismogram; red traces represent the extracted trace from the seismic data at the well location, and black traces shows the ten traces around the well location. Yellow bars show the correlation window..... | 32 |
| Figure 2.16: Final tie of well 14-35 with the multi-well wavelet. Blue traces represent the synthetic seismogram; red traces represent the extracted trace from the seismic data at the well location, and black traces shows the ten traces around the well location. Yellow bars show the correlation window..... | 32 |
| Figure 2.17: Seismic section with wells 14-35, 14-27 and 12-27 after seismic-wells tie process.....   | 33 |
| Figure 2.18: Filter panels assessing low frequency data present in the seismic data. The unfiltered seismic data are displayed for reference. The red curve is the GR log. The amplitude scalar is constant at 10.6528. ....  | 34 |

|   |    |
|---|----|
| Figure 2.19: Initial low frequency P-impedance model (3-5 Hz) using the Well 14-35 and the horizons Basal Belly River, Base Fish Scale and Stettler Salt. The inserted black curve is the GR log. ....  | 35 |
| Figure 2.20: Analysis of the post-stack inversion at Well 14-35 with the initial model cut-off of 0-3 Hz: a) filtered impedance log (blue), initial model (black), inversion result (red); b) synthetic trace from inversion (red) and extracted trace from the seismic (black), and c) RMS error between synthetic trace and seismic trace. .... | 37 |
| Figure 2.21: Analysis of the post-stack inversion at Well 14-35 with the initial model cut-off of 0-4 Hz: a) filtered impedance log (blue), initial model (black), inversion result (red); b) synthetic trace from inversion (red) and extracted trace from the seismic (black), and c) RMS error between synthetic trace and seismic trace. .... | 38 |
| Figure 2.22: Analysis of the post-stack inversion at Well 14-35 with the initial model cut-off of 0-5 Hz: a) filtered impedance log (blue), initial model (black), inversion result (red); b) synthetic trace from inversion (red) and extracted trace from the seismic (black), and c) RMS error between synthetic trace and seismic trace. .... | 39 |
| Figure 2.23: Analysis of the post-stack inversion at Well 14-35 with the initial model cut-off of 0-8 Hz: a) filtered impedance log (blue), initial model (black), inversion result (red); b) synthetic trace from inversion (red) and extracted trace from the seismic (black), and c) RMS error between synthetic trace and seismic trace. .... | 40 |
| Figure 2.24: Analysis of the post-stack inversion at Well 12-27: Impedance log (blue), inversion result (red) for each initial model. ....  | 41 |
| Figure 2.25: Analysis of the post-stack inversion at Well 14-27: Impedance log (blue), inversion result (red) for each initial model. ....  | 42 |
| Figure 2.26: Impedance log vs. Inverted impedance plots for Well 12-27 for each initial model: a) 0-3 Hz, b) 0-4 Hz, c) 0-5 Hz and d) 0-8 Hz. The correlation increases when a higher limit to the low-frequency component is added. ....   | 43 |
| Figure 2.27: Impedance log vs. Inverted impedance curve plots for Well 14-27 for each initial model: a) 0-3 Hz, b) 0-4 Hz, c) 0-5 Hz and d) 0-8 Hz. The correlation remains stable for all the cases. ....  | 44 |
| Figure 2.28: Impedance log vs. Inverted impedance curve plots for Well 14-35 for each initial model: a) 0-3 Hz, b) 0-4 Hz, c) 0-5 Hz and d) 0-8 Hz. The correlation increases when a higher limit to the low-frequency component is added. ....   | 44 |

|   |    |
|---|----|
| Figure 2.29: Inversion result of Hussar 10 Hz dynamite dataset showing the GR curve in black and the impedance log with a high-cut filter 60/85 Hz in color at the well locations for comparison. ....  | 46 |
| Figure 2.30: Inversion result of Hussar 10 Hz dynamite dataset with a band-pass filter of 10-15-60-85 Hz showing the GR curve in black and the impedance log with a high-cut filter 60/85 Hz in color at the well locations for comparison. Note the differences in continuity and character of the events with respect to the results on Figure 2.29. ....   | 47 |
| Figure 3.1: Regional geologic cross-section across the WASP study area (green polygon) in the northeast-southwest direction. The dashed line in the (A-A') in the map indicates the location of the section (modified from Alshuhail, 2011). ....   | 51 |
| Figure 3.2: Cross-section across the WASP study area with a northwest-southeast direction showing some of the lithofacies of the Nisku Formation. The dashed line (B-B') in the bottom map indicates the location of the section (modified from Alshuhail, 2011). ....  | 53 |
| Figure 3.3: Project Pioneer stratigraphic column in the Wabamun Lake area. The target aquifer is indicated by the red rectangle (after Project Pioneer, 2013: <a href="http://www.transalta.com/sites/default/files/Project%20Pioneer_Final%20Report_Executive%20Summary_2013.pdf">http://www.transalta.com/sites/default/files/Project%20Pioneer_Final%20Report_Executive%20Summary_2013.pdf</a> ). .... | 54 |
| Figure 3.4: Well 8-17 with its complete logs suite recorded through the target formation down to a depth of 1900 m. ....  | 55 |
| Figure 3.5: Highvale stacked section with Well 8-17. ....   | 56 |
| Figure 3.6: a) shot 183 from the Highvale 2D seismic line, and b) shot 48 from the Violet Grove 2D seismic line. AGC has been applied. ....   | 57 |
| Figure 3.7: Highvale line first break time gate on shot 104 and an example of the automated picked trough on shot 173. ....   | 59 |
| Figure 3.8: Highvale line shot 104 a) before and b) after statics correction. ....  | 60 |
| Figure 3.9: Highvale line shot 104 a) before and b) after amplitude recovery compensation. ....   | 61 |
| Figure 3.10: Shot 104 of the Highvale line a) after surface wave attenuation and b) after radial trace filtering. ....  | 63 |
| Figure 3.11: Shot 104 of the Highvale line a) before and b) after applying Gabor Deconvolution and a bandpass filter of 3-6-55-70 Hz. ....  | 65 |

|   |    |
|---|----|
| Figure 3.12: From left to right: semblance panel, CDP gather and velocity functions stack panels from the velocity analysis on the Highvale line. The final velocity function is shown with a white line on the semblance panel and a red line on the stack panel.....  | 67 |
| Figure 3.13: Velocity model obtained from the velocity analysis .....   | 67 |
| Figure 3.14: Highvale CDP stacked section. Clear reflections are easily identified across the section. ....   | 69 |
| Figure 3.15: Highvale stack section after applying conventional processes and Implicit Finite Difference Time Migration and F-X Deconvolution. No major changes are observed in terms on the position of the reflectors due to the flat character of the events.....  | 70 |
| Figure 3.16: Highvale stack section after applying special processes (Radial Filter and Gabor Deconvolution) and Implicit Finite Difference Time Migration and F-X Deconvolution. ....  | 71 |
| Figure 3.17: Violet Grove stack section after applying conventional processes and Implicit Finite Difference Time Migration and F-X Deconvolution. ....   | 72 |
| Figure 3.18: Comparison of processing results: a) previous processing b) current specialized sequence and c) current conventional sequence. Note the difference in frequency content, resolution and continuity of the events depending on the processing applied. The red dotted line shows the location of the Well 8-17. ....                                      | 73 |
| Figure 3.19: Frequency spectra of the datasets shown in figure 3.17 in a 700 ms window around the target formation. Note the low frequencies include 5-9 Hz in cases b) and c), while in case a) the frequency content includes 10-14 Hz. ....  | 74 |
| Figure 3.20: Nisku core sample and Calmar core plug recovered from Well 8-17 during the development of Project Pioneer. Diameter = 1 inch (modified from Carbon Management Canada, 2013: <a href="http://www.cmc-nce.ca/events/gallery/">http://www.cmc-nce.ca/events/gallery/</a> ). ....  | 75 |
| Figure 3.21: Cross plot between $Z_p$ and porosity and GR in the colour key. Note how Cleaner lithologies ( $GR < 10$ ) separates from more shaly lithologies with high values of P-impedance ( $Z_p > \sim 16 \times 10^6 \text{ kg}/(\text{s} \cdot \text{m}^2)$ ). The two yellow bars above the Nisku Formation correspond to Calmar and Graminia formations..... | 77 |
| Figure 3.22: Wavelet extracted from Well 8-17 in case a) with its amplitude spectrum. The dotted line indicates the average phase of the wavelet ( $-56^\circ$ ).....   | 78 |
| Figure 3.23: Final tie of Well 8-17 with the C&C dataset (case a). Blue traces represent the synthetic seismogram; red traces represent the extracted trace from  |    |

|  |    |
|--|----|
| the seismic data at the well location, and black traces shows the ten traces around the well location. Yellow bars show the correlation window. Correlation = 74% ..   | 78 |
| Figure 3.24: Wavelet extracted from Well 8-17 in case b) with its amplitude spectrum. The dotted line indicates the average phase of the wavelet ( $-7^\circ$ ).....   | 79 |
| Figure 3.25: Final tie of Well 8-17 with the case b) dataset. Blue traces represent the synthetic seismogram; red traces represent the extracted trace from the seismic data at the well location, and black traces shows the ten traces around the well location. Yellow bars show the correlation window. Correlation = 62% .....                  | 79 |
| Figure 3.26: Wavelet extracted from Well 8-17 in case c) with its amplitude spectrum. The dotted line indicates the average phase of the wavelet ( $102^\circ$ ). .....  | 80 |
| Figure 3.27: Final tie of Well 8-17 with the case c) dataset. Blue traces represent the synthetic seismogram; red traces represent the extracted trace from the seismic data at the well location, and black traces shows the ten traces around the well location. Yellow bars show the correlation window. Correlation = 47% .....                  | 80 |
| Figure 3.28: Initial low frequency P-impedance model (0-0-8-13 Hz) using Well 8-17 and the Second White Speckled Shale horizon. The inserted black curve is the $V_P$ log. ....  | 82 |
| Figure 3.29: Initial low frequency P-impedance model (0-0-6-10 Hz) using Well 8-17 and the Second White Speckled Shale horizon. The inserted black curve is the $V_P$ log. ....  | 82 |
| Figure 3.30: Analysis of the post-stack inversion at Well 8-17 with the initial model cut-off of 0-0-8-13 Hz: a) filtered impedance log (blue), initial model (black), inversion result (red); b) synthetic trace from inversion (red) and extracted trace from the seismic (black), and c) RMS error between synthetic trace and seismic trace..... | 84 |
| Figure 3.31: Analysis of the post-stack inversion at Well 8-17 with the initial model cut-off of 0-0-6-10 Hz: a) filtered impedance log (blue), initial model (black), inversion result (red); b) synthetic trace from inversion (red) and extracted trace from the seismic (black), and c) RMS error between synthetic trace and seismic trace..... | 85 |
| Figure 3.32: Inversion result of the Highvale seismic data based on previous processing (case a) showing the gamma ray curve in black and the impedance log with a high-cut filter 60/100 Hz in color at the well location for comparison. ..  | 87 |
| Figure 3.33: Inversion result of the Highvale seismic data based on new processing (case b) showing the gamma ray curve in black and the impedance log with a high-cut filter 60/100 Hz in color at the well location for comparison.....  | 87 |

|   |     |
|---|-----|
| Figure 3.34: Inversion result of Highvale line previous processing (case a) on Wabamun and Winterburn Groups with the gamma ray curve in black and the impedance log with a high-cut filter 60/100 Hz inserted in colour at the well location for comparison. ....  | 89  |
| Figure 3.35: Inversion result of Highvale line current processing (case b) on Wabamun and Winterburn Groups with the gamma ray curve in black and the impedance log with a high-cut filter 60/100 Hz inserted in colour at the well location for comparison. ....   | 89  |
| Figure 4.1: 2D geological model. The location of the injection zone in the Nisku Formation is indicated by the black rectangle. ....  | 94  |
| Figure 4.2: CO <sub>2</sub> plume designed. ....  | 95  |
| Figure 4.3: Monitor 2D geological model ( $V_P$ , $V_S$ and $\rho$ ). The rectangular CO <sub>2</sub> plume is inserted in the Nisku Formation. ....  | 96  |
| Figure 4.4: 2D seismic modelling survey design. The line is 17.38 km long with 80 m shots spacing and 20 m receivers spacing.....   | 97  |
| Figure 4.5: Shot gather 109 from baseline 2D modelling. 200 channels per shot. ....   | 98  |
| Figure 4.6: RMS P-wave velocity field converted from the interval velocity field defined in the 2D baseline geological model. ....  | 99  |
| Figure 4.7: a) Baseline CDP stack section, b) Monitor CDP stacked section. Injection zone is indicated in red square. ....  | 100 |
| Figure 4.8: Difference between baseline CDP stack and monitor stack. The red square highlights 100% CO <sub>2</sub> injection zone. ....  | 101 |
| Figure 4.9: Comparison of baseline (blue) and monitor (red) traces at CDP location 726. ....  | 102 |
| Figure 4.10: a) Wavelet extracted from synthetic well with the baseline CDP stacked section. b) Amplitude spectrum. The dotted line indicates the average phase of the wavelet (-14°). ....   | 103 |
| Figure 4.11: Tie process of synthetic $V_P$ and density logs with the baseline CDP stacked section. Blue traces represent the synthetic seismogram; red traces represent the extracted trace from the seismic data at the well location, and black traces shows the ten traces around the well location. Yellow bars show the correlation window. Correlation = 93%. .... | 104 |
| Figure 4.12: Analysis of the post-stack inversion at synthetic well location: a) filtered impedance log (blue), initial model (black), inversion result (red); b) synthetic   |     |

|   |     |
|---|-----|
| trace from inversion (red) and extracted trace from the seismic (black), and c) RMS error between synthetic trace and seismic trace. ....   | 105 |
| Figure 4.13: a) Baseline inversion, b) Monitor inversion. Distortion in the impedance values in the injection region and reflectors underneath is evident. ....   | 106 |
| Figure 4.14: Comparison of baseline (blue) and monitor (red) inverted traces at CDP location 726.....   | 107 |
| Figure 4.15: Difference between baseline inversion and monitor inversion. The black square highlights 100% CO <sub>2</sub> injection zone. ....   | 108 |
| Figure 4.16: Analysis of the post-stack inversion of the CDP stack section difference at synthetic well location: a) filtered impedance log (blue), initial model (black), inversion result (red); b) synthetic trace from inversion (red) and extracted trace from the seismic (black), and c) RMS error between synthetic trace and seismic trace. .... | 110 |
| Figure 4.17: a) Difference of impedance sections in Figure 4.13, and b) inversion of the difference on Figure 4.8. ....   | 111 |

## List of Symbols, Abbreviations and Nomenclature

| <b>Symbol</b>     | <b>Definition</b>  |
|-------------------|--|
| %                 | Percentage   |
| *                 | Convolution  |
| °                 | Degree   |
| $\mu\rho$         | Mu-Rho   |
| 2D                | Two-Dimensional  |
| 3C                | Three-Component  |
| 3D                | Three-Dimensional  |
| A                 | Area   |
| AERI              | Alberta Energy Research Institute                                |
| API               | American Petroleum Institute (Gamma Ray Units)                   |
| CCS               | Carbon Capture and Storage                                       |
| CDP               | Common Depth Point   |
| CMC               | Carbon Management Canada   |
| CNRL              | Canadian Natural Resources Limited                               |
| CO <sub>2</sub>   | Carbon Dioxide   |
| CREWES            | Consortium of Research in Elastic Waves Exploration Seismologist |
| D                 | Diameter   |
| E                 | Efficiency   |
| EOR               | Enhance Oil Recovery   |
| $f_d$             | Dominant Frequency   |
| g/cc              | Grams per Cubic Centimeter                                       |
| G <sub>CO2</sub>  | Volume of CO <sub>2</sub>  |
| GR                | Gamma Ray  |
| H                 | Integration Operator   |
| h                 | Thickness  |
| Hz                | Hertz  |
| kg/m <sup>3</sup> | Kilograms per Cubic Meter  |
| km                | Kilometer  |
| <i>m</i>          | Mass   |
| m                 | Meter  |
| m/s               | Meters per Seconds   |
| mD                | Millidarcy   |
| mm                | Millimeter   |
| ms                | Milliseconds   |
| N                 | Noise  |
| NMO               | Normal Move Out  |
| PHIT              | Total Porosity   |
| P-impedance       | Compressional Impedance  |
| P-wave            | Compressional Wave   |
| r                 | Radius   |
| R                 | Reflectivity   |

|                                |  |
|--------------------------------|--|
| RHOB                           | Bulk Density                                       |
| RMS                            | Root Mean Square                                   |
| S                              | Seismic Trace                                      |
| S <sub>O</sub>                 | Oil Saturation                                     |
| S <sub>W</sub>                 | Water Saturation                                   |
| S-wave                         | Shear Wave   |
| T                              | Period   |
| t <sub>P</sub>                 | P-wave Time  |
| V/V                            | Volumetric Scale (0-1)                             |
| V <sub>P</sub>                 | P-wave Velocity                                    |
| V <sub>P</sub> /V <sub>S</sub> | Ratio between P-wave and S-wave Velocity           |
| V <sub>S</sub>                 | S-wave Velocity                                    |
| V <sub>Shale</sub>             | Volume of Shale                                    |
| W                              | Wavelet  |
| WASP                           | Wabamun Area CO <sub>2</sub> Sequestration Project |
| WCSB                           | Western Canada Sedimentary Basin                   |
| Z                              | Impedance  |
| Z                              | Minimum Thickness                                  |
| Z <sub>P</sub>                 | Compressional Impedance                            |
| λρ                             | Lambda-Rho   |
| π                              | Pi   |
| ρ                              | Density  |
| φ                              | Porosity   |

## CHAPTER 1: INTRODUCTION

Seismic inversion is used widely in the processing and analysis of reflection seismic data for the purpose of estimate rock properties, particularly acoustic impedance. Seismic inversion is used for well planning, reservoir characterization and to monitor changes in rock properties in the reservoir during fluid injection or production (e.g. porosity and net pay).

### 1.1 Seismic Inversion and Applications

#### 1.1.1 Method Description

Inversion of seismic data is the process to produce an estimate of earth's acoustic impedance. The way in which the reflectivity can be extracted from the seismic data is based on the convolutional model of the seismic trace according to equation 1.1:

$$S = W * R + N \quad (1.1)$$

where S is the seismic trace, W is the wavelet, R is the reflectivity and N is noise. Noise is assumed to be random and uncorrelated with the signal.

Reflectivity is defined as the contrast in impedance between two interfaces (equation 1.2) where the impedance (Z) is simply the product between velocity and density:

$$R_i = \frac{Z_{i+1} - Z_i}{Z_{i+1} + Z_i} \quad (1.2)$$

Band-limited impedance inversion is commonly used with a classical recursive inversion algorithm, which ignores the effect of the seismic wavelet, and treats the trace

as a set of reflection coefficients (Lindseth, 1979). The inversion of seismic data is based upon rearranging the terms of (1.2) to give the impedance series:

$$Z_{i+1} = Z_i \left( \frac{1+R_i}{1-R_i} \right) \quad (1.3)$$

The inversion requires the initial value of  $Z$  to be known and the inherent bandwidth characteristic of the seismic adds a limitation to this technique (**Error! Reference source not found.**). The low-frequency component missing in the seismic must be added from another source, such as filtered sonic logs (Figure 1.2) to assure a more realistic result (Lindseth, 1979). Several authors have raised the importance of include an initial guess to accurate predict an impedance model and proposed different techniques to deal with this problem. Some of the suggested solutions involve linear programming algorithms and autoregressive process (Oldenburg et al., 1982), and generalized linear inversion (Cooke and Schneider, 1983). All these techniques suffer from non-uniqueness since there is more than one geological model consistent with the seismic response.

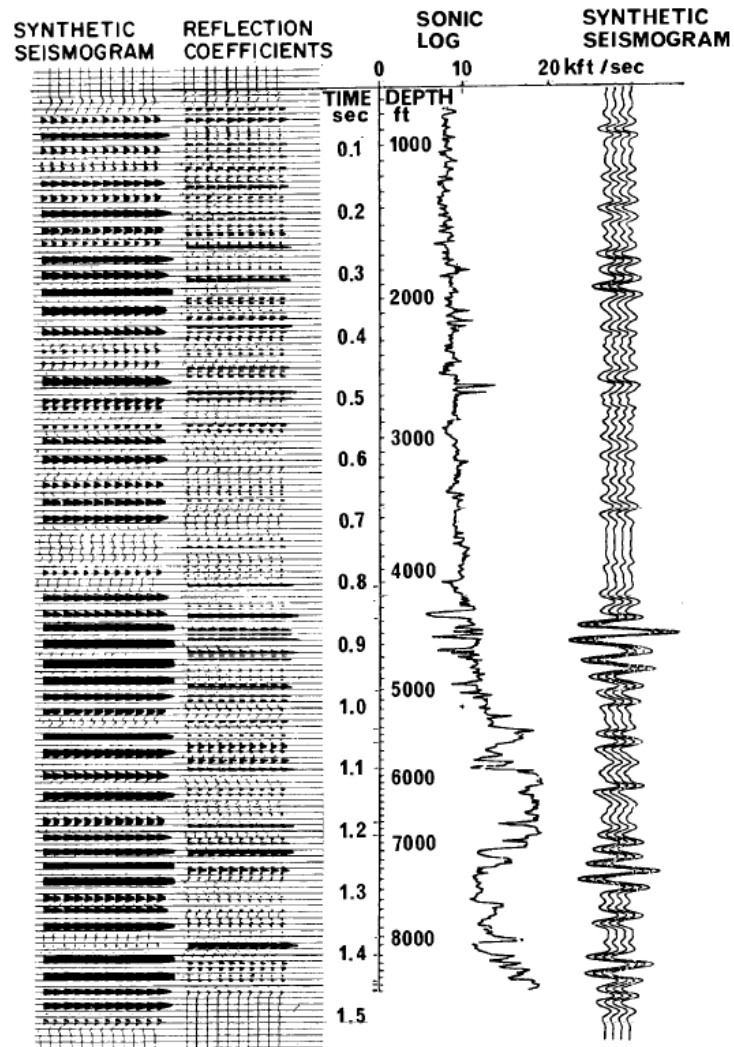
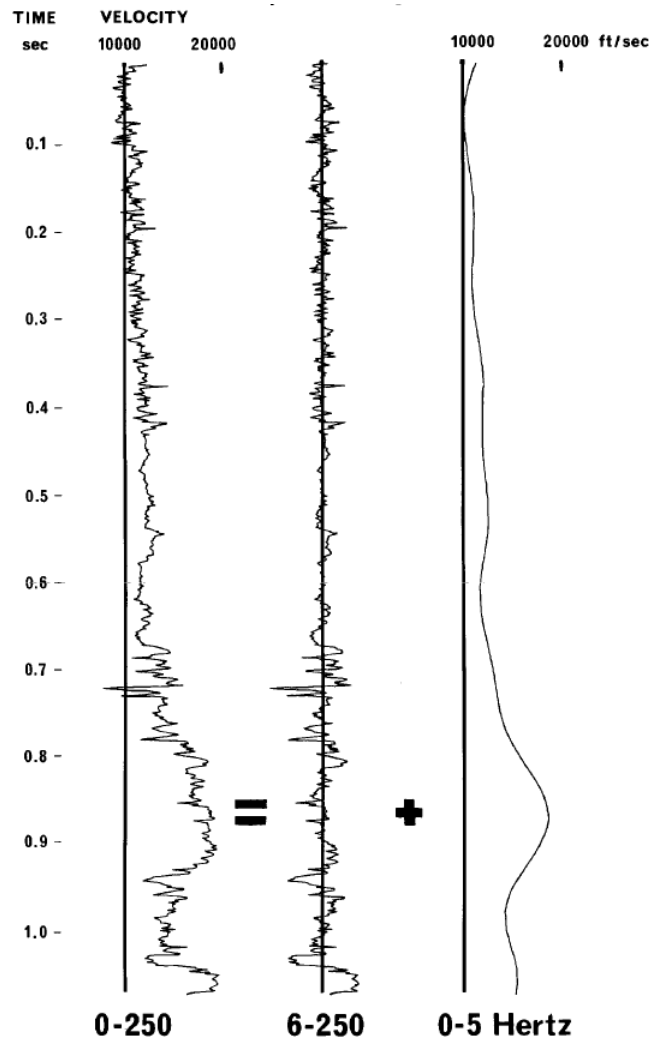


Figure 1.1: Comparison of a sonic log with its corresponding series of reflection and resulting synthetic seismogram to illustrate the effect of bandwidth reduction on seismic signals (Lindseth, 1979: <http://dx.doi.org/10.1190/1.1440922>).



**Figure 1.2: Illustration of missing low-frequency components in synthetic sonic logs obtained from inverting seismic data. A sonic log may be considered as a low-frequency function modulated by a higher-frequency function. The low-frequency part can be used in the initial guess (Lindseth, 1979: <http://dx.doi.org/10.1190/1.1440922>).**

Hampson and Russell (1991) described three post-stack inversion methods grouped in three categories: classical recursive or band-limited, sparse-spike and model-based. Band-limited inversion, discussed above, involves integrating the seismic data directly to produce a band-limited inverted trace incorporating the missing low frequency

trend from the geological model. The sparse-spike inversion method estimates a set of sparse reflection coefficients from the seismic data and constrains them with the model to produce the impedance from inverting these coefficients. In model-based inversion, an initial model of the earth's geology is designed and then perturbed until the derived synthetic seismic section best fits the observed seismic data. Hampson and Russell (1991) concluded that the band-limited approach was the most robust but it tended to produce a smoothed, frequency limited estimate of the impedance and failed in the case of a very "sparse" model. The sparse-spike and model-based methods produced similar results. The sparse-spike approach produced superior results for a complete "sparse" model, but produced lower resolution than model-based inversion when applied to real data. Model-based inversion appears to be the most intuitively appealing, but it has to be carefully constrained to minimize the problem of non-uniqueness. Figure 1.3 shows the result of using the three methods in the Blackfoot dataset (STRATA user guide, 2009).

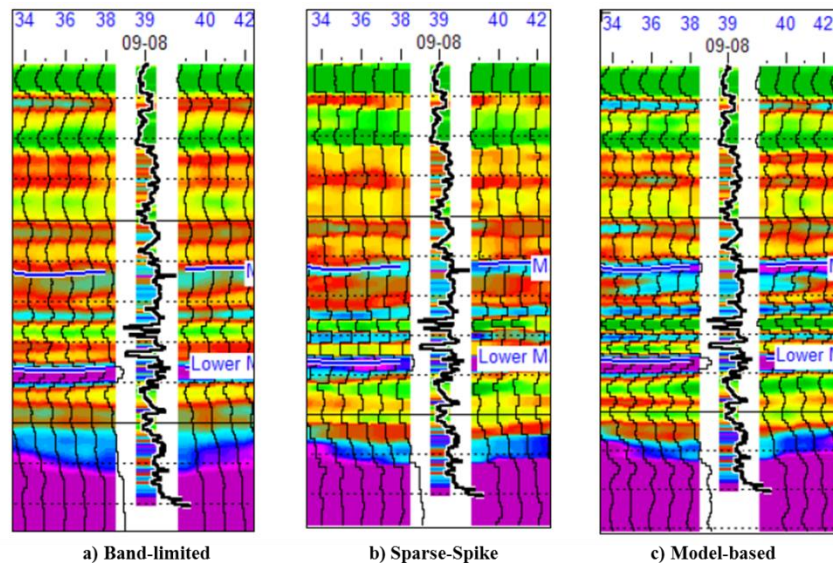


**Figure 1.3: Comparison of the three post-stack inversion methods: a) band-limited, b) sparse-spike, and c) model-based (modified from STRATA user guide, 2009).**

The approach applied in this thesis is based on the Hampson-Russell Software model-based inversion method to estimate acoustic impedance at two study areas, namely the Hussar Experiment and Project Pioneer in the Wabamun area, and also a 2D modelling case simulating the CO<sub>2</sub> injection in the Nisku Formation.

#### 1.1.1.1 Model-based inversion:

Model-based inversion (Russell and Hampson, 1991) uses a generalized linear inversion algorithm which assumes that the seismic trace (S) and the wavelet (W) are known and attempts to modify the initial model until the resulting synthetic matches the seismic trace (Cooke and Schneider, 1983). This method is effective when there is considerable knowledge about the geology and a reliable model can be created.

The basic approach is to minimize this function:

$$J = weight_1 \times (S - W * R) + weight_2 \times (M - H * R) \quad (4)$$

where S is the seismic trace, W the wavelet, R the final reflectivity, M the initial guess model and H the integration operator which convolves with the final reflectivity to produce the final impedance (\* = convolution). The first part models the seismic trace, while the second part models the initial guess impedance. The software implements a “Constrained Model Inversion”,  $weight_2$  is 0, where the final impedance values are set within upper and lower values (using a percentage of the average impedance for the log). This hard constraint prevents small amounts of noise in the data or modeling errors (STRATA user guide, 2009). Another option is to consider the additional information as a "soft" constraint, meaning that the initial guess impedance is considered as a separate

component which is added to the seismic trace. In general, the hard constraint is recommended.

The model-based approach is summarized as follows:

- It is assumed that the wavelet is known so its effect can be removed from the seismic. For instance, the seismic data does not have to be zero-phase as long as the wavelet has the same phase as the seismic data.
- Errors in the estimated wavelet will affect the inversion result.
- The resolution of the seismic data is enhanced.
- The result can be dependent on the initial model. The model can be filtered to reduce this effect so it includes the low-frequency component usually absent in the seismic data.
- The non-uniqueness problem persists; meaning that there is more than one geological model consistent with the seismic response. To reduce this uncertainty the initial model should be independent of the seismic data and must include information about the unknown geology (well logs, velocity fields, etc).

## *1.1.2 Seismic Inversion as a Monitoring Technique in CO<sub>2</sub> Sequestration Programs*

### 1.1.2.1 CO<sub>2</sub> Sequestration in Geologic Formations:

CO<sub>2</sub> sequestration is a possible solution for mitigating climate changes through the capture and secure storage of the carbon dioxide (Bachu et al., 2000). This technology has been designed to prevent large quantities of CO<sub>2</sub> from being released into the atmosphere by storing it in terrestrial ecosystems (soils and vegetation), oceans and geological media. Injection of CO<sub>2</sub> in geological formations is likely the most viable solution since has being already developed and used in the Oil & Gas production for enhanced oil recovery (EOR) processes (Bachu, 2001). In geological formations, the storage locations are made up of solid, porous rock filled with salty water and oil; the CO<sub>2</sub> can mix and dissolve in both the salty water and oil meaning that a portion of the CO<sub>2</sub> is no longer in a form that can escape. Also, cap rocks above the reservoir are required to prevent CO<sub>2</sub> from escaping.

Project Pioneer was an excellent initiative of this technology. Chapter 3 discusses with more details the specifications of this project, which unfortunately was cancelled in 2012. The objective was to capture some of the CO<sub>2</sub> from a coal-fired power plant (Keepills 3) in the Wabamun Lake area, then compress and transport it by pipeline to a sequestration site to be injected ~2 km underground into a saline formation (Nisku Formation).

Figure 1.4 illustrates this scenario (Project Pioneer, 2013: [http://www.transalta.com/sites/default/files/Project%20Pioneer\\_Final%20Report\\_Executive%20Summary\\_2013.pdf](http://www.transalta.com/sites/default/files/Project%20Pioneer_Final%20Report_Executive%20Summary_2013.pdf)).

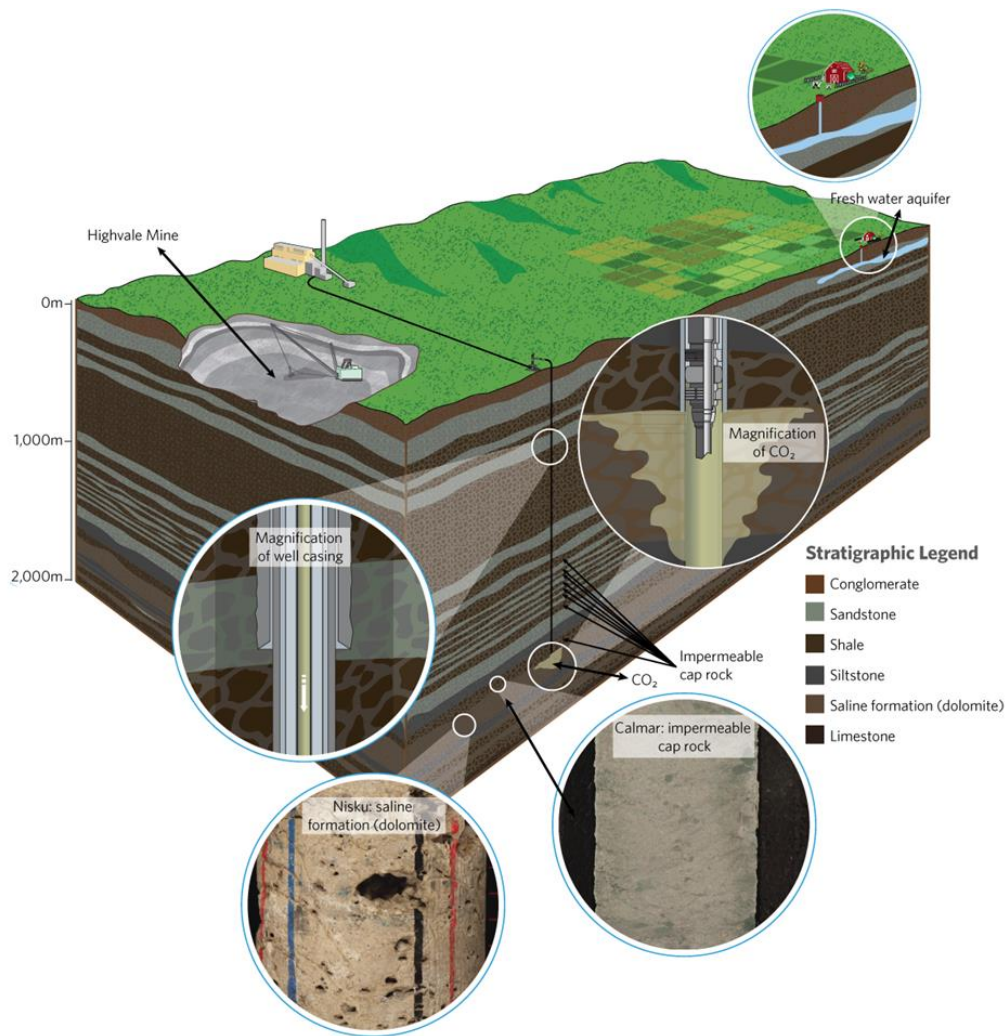


**Figure 1.4: Project Pioneer Carbon Storage illustration. CO<sub>2</sub> generated in a coal-fired power plant station could have been injected in the Nisku saline Formation and sealed by the Calmar Formation cap rock (modified from Project Pioneer, 2013: [http://www.transalta.com/sites/default/files/Project%20Pioneer\\_Final%20Report\\_Executive%20Summary\\_2013.pdf](http://www.transalta.com/sites/default/files/Project%20Pioneer_Final%20Report_Executive%20Summary_2013.pdf)).**

Carbon Capture and Storage (CCS) in geological formations is a viable solution for mitigating the effect that greenhouse gases are causing to the atmosphere and requires comprehensive analysis for a successful application. One of the important issues to be considered is how the injected gas will affect the surrounding formation (Alshuhail,

2011). Seismic modelling along with acoustic inversion will allow us to evaluate and monitor this effect.

#### 1.1.2.2 Seismic Inversion as a Monitoring Technique in CO<sub>2</sub> Sequestration Programs:

The effect of injecting CO<sub>2</sub> in a carbonate reservoir was studied by Wang et al., (1998). Laboratory measurements and a pilot injection project were undertaken in the Permian Grayburg Formation, McElroy field, west Texas. After injection, the velocity changes observed in the time-lapse surveys are consistent with laboratory measurements if the effects of changing pore pressure are taken into account. As CO<sub>2</sub> displaces the original reservoir fluid it decreases the bulk modulus with little change in the bulk density of the reservoir rock, causing the P-wave interval travel-time through the aquifer to increase.  $V_P$  decreases ~6% and this change is higher in high-porosity rocks. S-wave velocity is hardly affected since the magnitude of the shear modulus remains unchanged. The changes in  $V_S$  vary from 0.5% to 2% due to a small change in density. Depending on seismic resolution, these changes can be detected by P-wave seismic data.

Adam et al., (2011) analyzed the chemical interaction of CO<sub>2</sub> in basalts determining a change in  $V_P$  of -4.5% and an increment in  $V_S$  of 2.5% at early times where fluid substitution dominates the process as the CO<sub>2</sub> replaces the in-situ fluid. At later times, the mineralization precipitates carbonates in the pore space increasing the elastic moduli and velocity of the rock.

Seismic methods in monitoring CO<sub>2</sub> sequestration programs attempts to identify the CO<sub>2</sub> plume in seismic images by comparing the seismic data acquired before and after injection. From the difference in this time-lapse study it is expected a series of sub-

horizontal high amplitude reflections with an underlying velocity pushdown (Chadwick et al., 2006). The main goal of monitoring CO<sub>2</sub> storage is demonstrate the safe storage of the CO<sub>2</sub> in the selected geological site, image the location of the CO<sub>2</sub> plume, and early detection of any leakage. Results in this field have proved the effectiveness of the seismic methods as a monitoring tool in Alberta, Canada. Alshuhail (2011) modelled the CO<sub>2</sub> plume effect through Gassmann fluid substitution and seismic modelling and found that, in the Wabamun Area Sequestration Project, the reflection time change and NRMS amplitude change in the Nisku Formation caused by the CO<sub>2</sub> was of ~1.5 ms and ~24%, respectively. A similar approach was undertaken in the Paskapoo Formation, Priddis, Alberta. In this case, the reflection coefficient decreased approximately 30% and the time delay was determined to be about 1 ms (Vera, 2012). The time-lapse modelling carried out in the Shell Quest Project showed a time shift in the reflection at the bottom of the Basal Cambrian Sandstone Formation of 3 ms after injecting CO<sub>2</sub>. Also the RMS amplitude increased about 30% in the monitor section (Moradi, 2013).

Since  $V_P$ ,  $V_S$  and density change after injecting CO<sub>2</sub>, the effect on acoustic and shear impedances should also change as CO<sub>2</sub> saturation increases, especially if it is different from the surrounding stratigraphy (Sparlin, 2010). The recursive inversion and model-based inversion were applied to characterize the Nisku Formation in the Wabamun Area Sequestration Project. The Nisku Formation was separated from the Wabamun Group and the underlain units with higher acoustic impedance values (Alshuhail, 2011). The acoustic impedance effect results in an amplitude change that is stronger in magnitude and, therefore, should be more discernible and reliable than P-wave seismic data.

In this thesis, the model-based inversion technique will be applied in a 2D modelling case which will simulate the injection of a CO<sub>2</sub> plume in the Nisku Formation. Prior performing the 2D modelling study, real seismic data will be examined to evaluate the effect of broadband seismic in two inversion studies. The first case evaluates the low-frequency component gain in the Hussar experiment; whereas the second case focused on retain the low-frequency component during seismic processing using the Project Pioneer dataset.

## **1.2 Area of Study**

### *1.2.1 Hussar Experiment Location*

The Hussar experiment was carried out in September 2011 by CREWES with collaboration of Husky Energy, Geokinetics and INOVA, with the purpose of acquiring low frequency seismic data to be used in inversion methods (Margrave et al., 2012). The area of study is located near Hussar, central Alberta, about 100 km East of Calgary (Figure 1.5).

### *1.2.2 Project Pioneer Location*

In this second case, the study area is located in the Western Canada Sedimentary Basin (WCSB), approximately 70 km west of Edmonton, where the Wabamun Area CO<sub>2</sub> Sequestration Project (WASP) study was undertaken and Project Pioneer was planned to be built at the Keephills 3 power station (Figure 1.5).

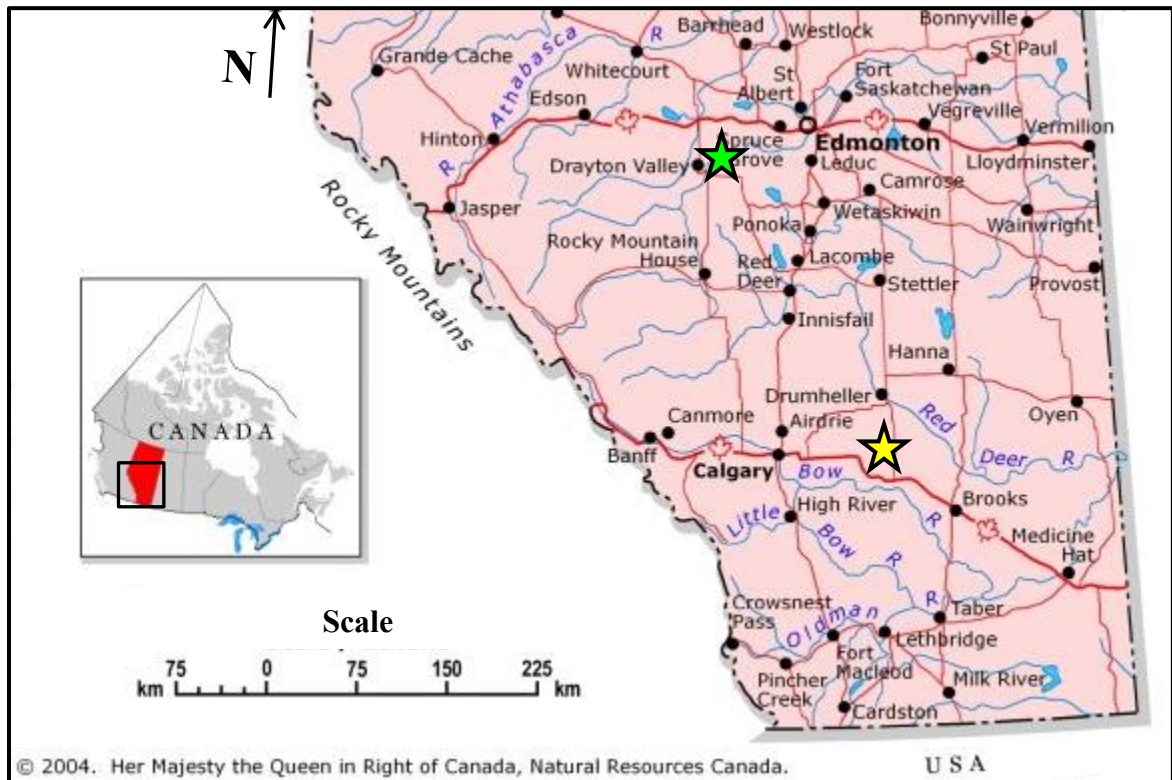


**Figure 1.5: Location of study areas in Alberta, Canada. Hussar Experiment (yellow star) and Project Pioneer (green star) (modified from Natural Resources Canada, 2013: <http://atlas.nrcan.gc.ca/site/english/maps/reference/provincesterritories/alberta>).**

#### 1.4 Thesis Objectives:

This thesis has contributed to improving seismic inversion studies by helping to understand the effect of having low-frequency content in the seismic data. Inversion methods are highly dependent on initial models that are built using the low-frequency trend from well logs. The lack of low-frequency content in the seismic data could lead to misinterpretations that could affect well planning among other things.

The principal goal of this thesis is to evaluate the influence of using broadband seismic data in inversion studies. The study was carried out by analyzing three datasets

from different areas within the Western Canada Sedimentary Basin (WCSB). To achieve the main goal, specific objectives were defined for each study case:

- The first case evaluated the low-frequency component gained during the Hussar Experiment by performing a model-based inversion study in a stacked section processed in CREWES. The focus of the analysis was to determine the lowest possible cut-off of the initial inversion model. This was accomplished by applying several frequency filters to identify the range of frequency values where coherent signal was no longer detectable. In addition, two out of three wells were used as blind test to accurately determine the quality of the inversion result.
- The second case compared the effect of using a dataset previously conditioned with a conventional processing flow versus applying a specialized processing flow focused on attaining coherent noise without compromising low-frequency signal. This study utilized data located in the Wabamun Lake area where several feasibility studies have been conducted to monitor CO<sub>2</sub> sequestration projects. Both datasets were inverted using the model-based inversion approach where the initial model in both cases was different based on their low-frequency content.
- The last case tested the inversion technique as a monitoring tool for CO<sub>2</sub> injection monitoring programs. To accomplish this goal a 2D seismic modelling was performed using the parameters of the dataset in case two. The target formation, identified as the Nisku saline aquifer, was modelled using well log information and reference parameters from a previous study in the same area. The time-lapse experiment evaluated the effect of the CO<sub>2</sub> plume by comparing changes in seismic amplitude and time shift before and after the injection. The model-based

inversion technique was applied to also measure the sensitivity in impedance changes. The result evidenced that the CO<sub>2</sub> plume is more easily identifiable by changes in impedance rather than changes in seismic patterns.

All three cases proved that there is a high influence of the initial inversion model which controls the inversion result; hence, the importance of using broadband seismic in inversion studies.

### **1.5 Thesis Outline:**

The thesis contains five chapters which discuss the research undertaken for the three study cases. Chapter 1 includes the seismic inversion theory background, area of study, objectives and software availability.

Chapter 2 discusses the first case study; namely the Hussar Experiment, starting with the project description and geologic overview, following with the data preparation and well log analysis to determine the feasibility of an inversion analysis and to investigate the influence of broadband seismic data for inversion studies. The inversion method was explained in detail from the seismic-well tie process to the initial model building and inversion results.

Chapter 3 describes the second case study, Project Pioneer. In this chapter, the seismic data was conditioned applying two full processing flows to evaluate the effect of noise attenuation methods while attempting to preserve low-frequency signal. After processing, a model-based inversion study was performed comparing previous processed stacks with the one processed in this research project.

Chapter 4 presents a 2D seismic modelling case to simulate a CO<sub>2</sub> injection scenario. First, 2D geological models were created before and after injection of the CO<sub>2</sub> plume. The models were used to compute synthetic seismic sections that represented the time-lapse seismic surveys. The seismic sections were compared to identify the CO<sub>2</sub> plume in terms of amplitude and impedance changes.

Chapter 5 discusses the results and conclusions from this thesis and provides some recommendations for further research projects.

## **1.6 Software:**

The work presented here was accomplished by the availability of the following software:

- ProMAX, Landmark 2D/3D seismic processing software (v. 5000.0.3.0).
- NORSAR-2D, a ray modelling package to create synthetic seismic data using ray tracing algorithms (v. 5.2).
- Hampson-Russell, a CGG company for 2D and 3D seismic interpretation and reservoir characterization services, including: seismic inversion, AVO analysis, Multi-attributes analysis, 4D and multi-component interpretation (v.9).
- Microsoft Office 2010, Microsoft Corporation office package (Word, Excel and PowerPoint).

## **CHAPTER 2: THE HUSSAR EXPERIMENT**

### **2.1 The Hussar Experiment Overview**

#### *2.1.1 Introduction*

As mentioned in Chapter 1, the Hussar experiment was carried out with the purpose of acquiring low frequency seismic data to be used in inversion methods. This chapter describes the methodology applied in performing a model-based inversion study in order to further investigate the effect of broadband seismic data in this inversion technique. The workflow includes: seismic processing, well logs analysis and seismic inversion.

#### *2.1.2 Geology Overview*

The geology of central Alberta is characterised by plains where the underlying surface formations are Cretaceous and Tertiary relatively soft and flat beds (Allan and Rutherford, 1934).

Oldest Cretaceous rocks belong to the Mannville Group (Mannville) and represent a major episode of subsidence and sedimentation following a long period of uplift, exposure and erosion of older strata (Mossop and Shetsen, 1994). A stratigraphic column encompassing the Mannville Group is shown in Figure 2.1. Mannville strata thickness ranges from less than 40 m in some areas of the plains to more than 700 m in the Rocky Mountain Foothills. Coals deposits are found on extensive coastal plains and are preserved primarily in the foothills and adjacent western plains (Smith et al., 1994). Oil and gas are trapped in fluvial reservoir sandstones in the south, and in shoreline sandstone units throughout northern and central regions (Smith et al., 1994). Natural gas

is extracted from the Ostracod and Glauconite beds in southern Alberta, and light oil is extracted from the Ellerslie Member in central and southern Alberta. The Mannville Group is disconformably overlain by the Joli Fou Formation shale of the Colorado Group (Figure 2.1) and it is underlay by older Paleozoic carbonates (Mossop and Shetsen, 1994).

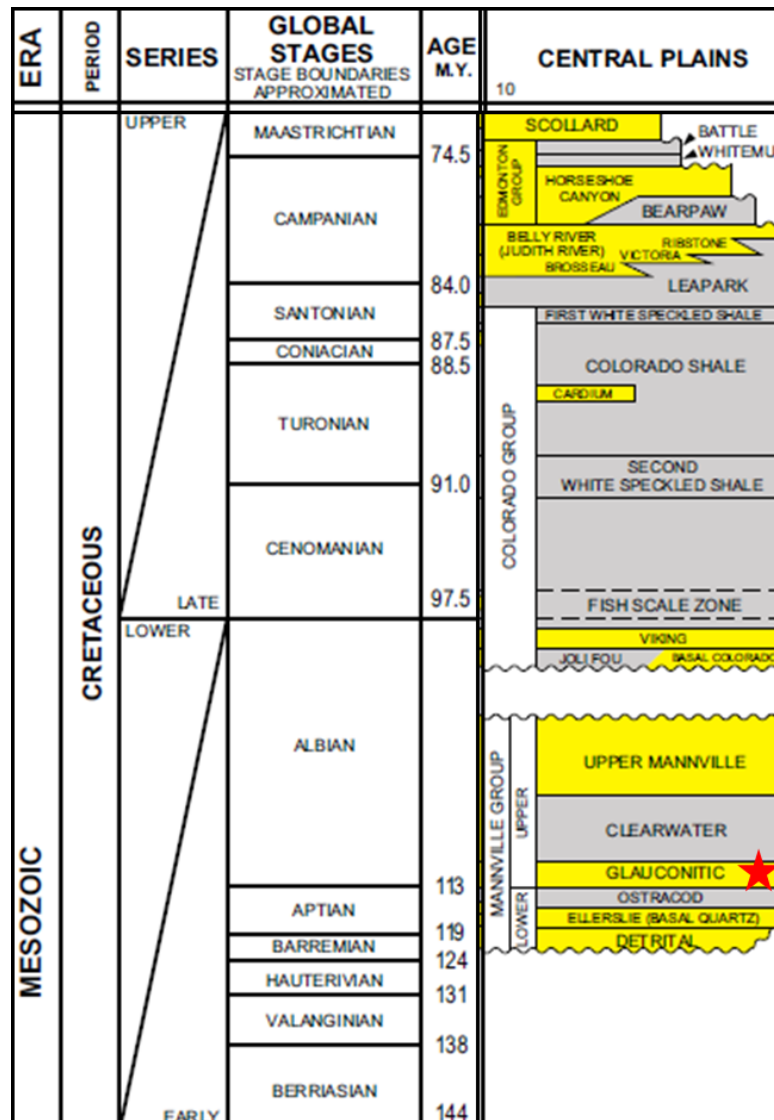


Figure 2.1: Stratigraphic column of the Mannville Group in Central Alberta. The red star indicates the target formation (modified from Core Lab Petroleum Services, 2012: <http://www.landman.ca/pdf/CORELAB.pdf>).

#### 2.1.2.1 Geological Framework:

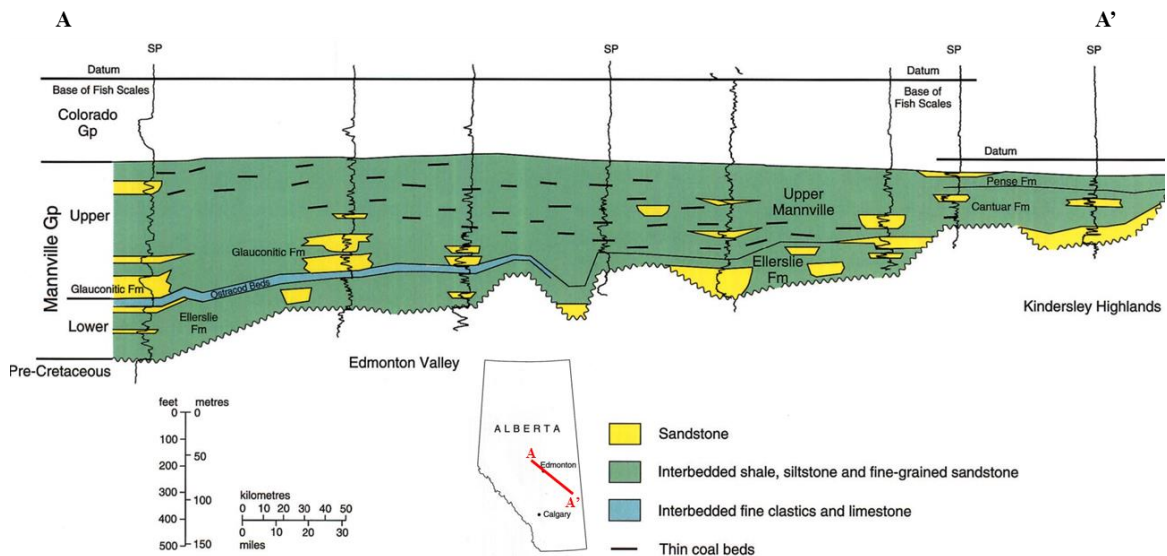
Smith (1994) summarized the geological framework as follows: Mannville strata are large deposits of sediments which form the second major clastic wedge of the foreland basin. During the Early Cretaceous, allochthonous terrains were accreted in the western Cordillera compressing older rocks and thrusting them on the continental margin. In result, these thrust sheets loaded the craton edge causing subsidence of the terrain, providing accommodation for this large volume of sediments. During the Early Albian, transgression of the Boreal Sea contributed with the deposition of more sediments. Several tectonic elements influenced Mannville sedimentation: the foredeep, where Mannville strata gets thicker westward from an eastern hingeline toward the foredeep; Peace River Arch, which is a block-faulted basement feature. The thickest Mannville section is preserved where the Peace River Arch and the foredeep converge in northeastern British Columbia; and Liard Basin, where a thick Mannville succession is also found. Mannville deposition took place over a deep unconformity surface that truncates strata from the Cretaceous in the foothills to lower Paleozoic at the eastern margin of the basin.

#### 2.1.2.2 Stratigraphic Units:

The Mannville lies on the sub-Mannville unconformity. Basal Mannville strata are continental of Albian age (Poulton et al., 1994). In the Alberta Plains, Mannville strata overly on Paleozoic carbonates and the Deville Member or "detrital" zone overlies the unconformity in some places (Williams, 1963). The Mannville Group consists of interbedded continental sand and shale in the base (Detrital and Ellerslie Member),

followed by a calcareous sandstone member and marine shale (Ostracod beds), Glauconitic Sandstone and marine shale and sandstone (Figure 2.2).

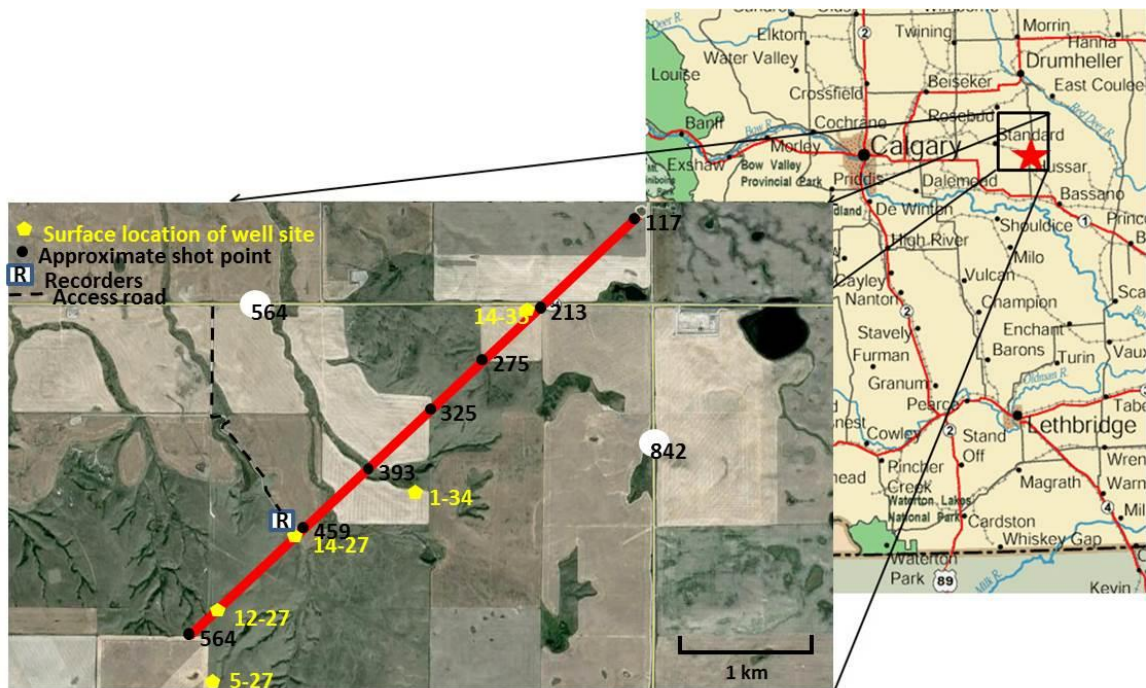
Glauconitic/Bluesky strata record the maximum transgression and subsequent early regressive stages of the Lower Cretaceous Sea in the southern and central parts of the basin. Marine evidence prevails in the Glauconitic Sandstone in Central Alberta and the Bluesky Formation in northern Alberta. In the South, Glauconitic Sandstone contains lacustrine sediments and channel sandstones (Wood and Hopkins, 1989). Some fluctuations in the sea level caused the deposition of a series of sandstones, shales and coals in the Upper Mannville.



**Figure 2.2: Cross-section of the Mannville Group in Central Alberta showing the main stratigraphic units (modified from Mossop and Shetsen, 1994).**

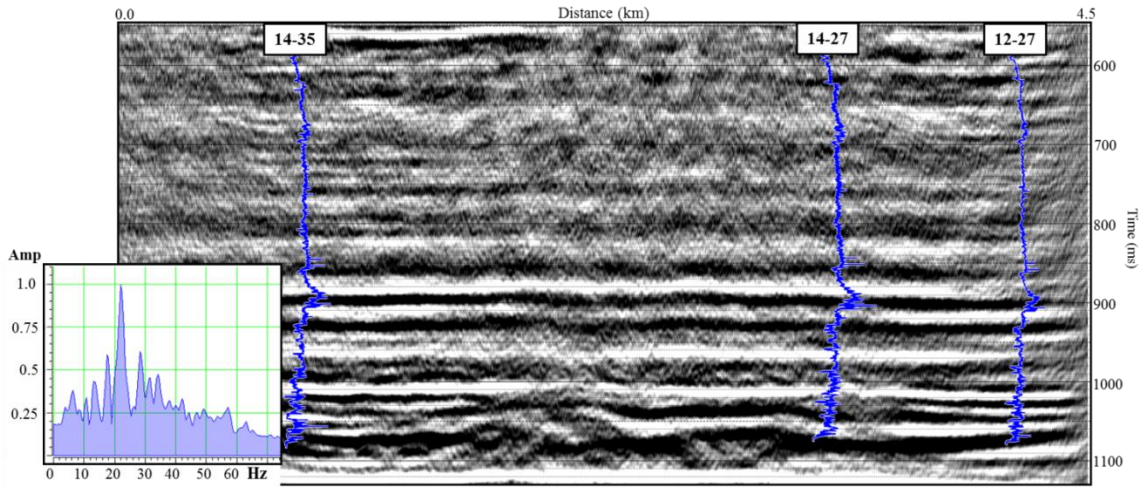
## 2.2 Hussar Experiment Data

The seismic data consist of a 2D line 4.5 km long. The line passes close to 3 wells owned by Husky Energy (wells 12-27, 14-27 and 14-35), (Figure 2.3). Four source types were used and each source was recorded by three receiver types (Margrave et al., 2012). The data used for this thesis shows the strongest low-frequency content from the following source and receiver combination: 2 kg dynamite recorded by 3C 10 Hz geophones (Margrave et al., 2012).



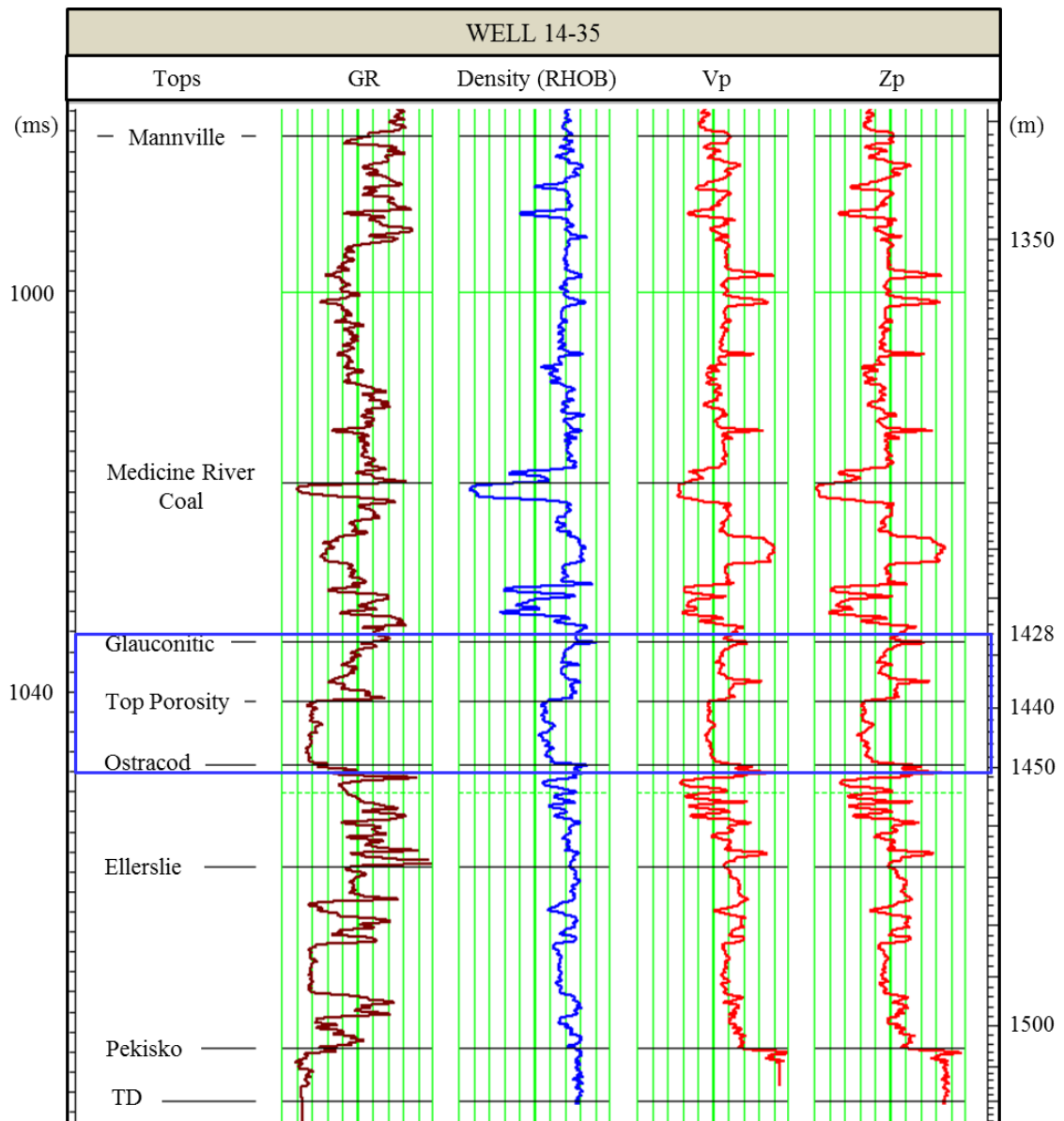
**Figure 2.3: Location of the seismic line with the well locations nearby (modified from Margrave et al., 2012).**

Figure 2.4 shows the migrated section and amplitude spectrum of the seismic line. The locations of the three wells are also shown. Isaac and Margrave (2011) analysed and processed the dataset and showed that the dominant signal band extends from about 10 Hz to 60 Hz with an increase in power from 4 to 10 Hz (Figure 2.4).



**Figure 2.4: 10 Hz dynamite Hussar migrated section with wells 14-35, 14-27 and 12-27. The amplitude spectrum of the unfiltered seismic data is also shown, with energy down to 4 Hz.**

The wells include complete logging suites including sonic and density logs. Well 12-27 is the only well that has an S-wave sonic log. Figure 2.5 shows the logging suite of well 14-35 where the Glauconitic Formation is found to be thickest and is characterised by low values of gamma ray (GR), density, P-wave velocity ( $V_P$ ) and P-impedance ( $Z_P$ ). Figure 2.6 and Figure 2.7 show the wells 14-27 and 12-27, respectively.



**Figure 2.5: Well 14-35. The blue rectangle highlights the Glauconitic Formation characterised with low values of gamma ray (GR), density,  $V_p$  and  $Z_p$  logs.**

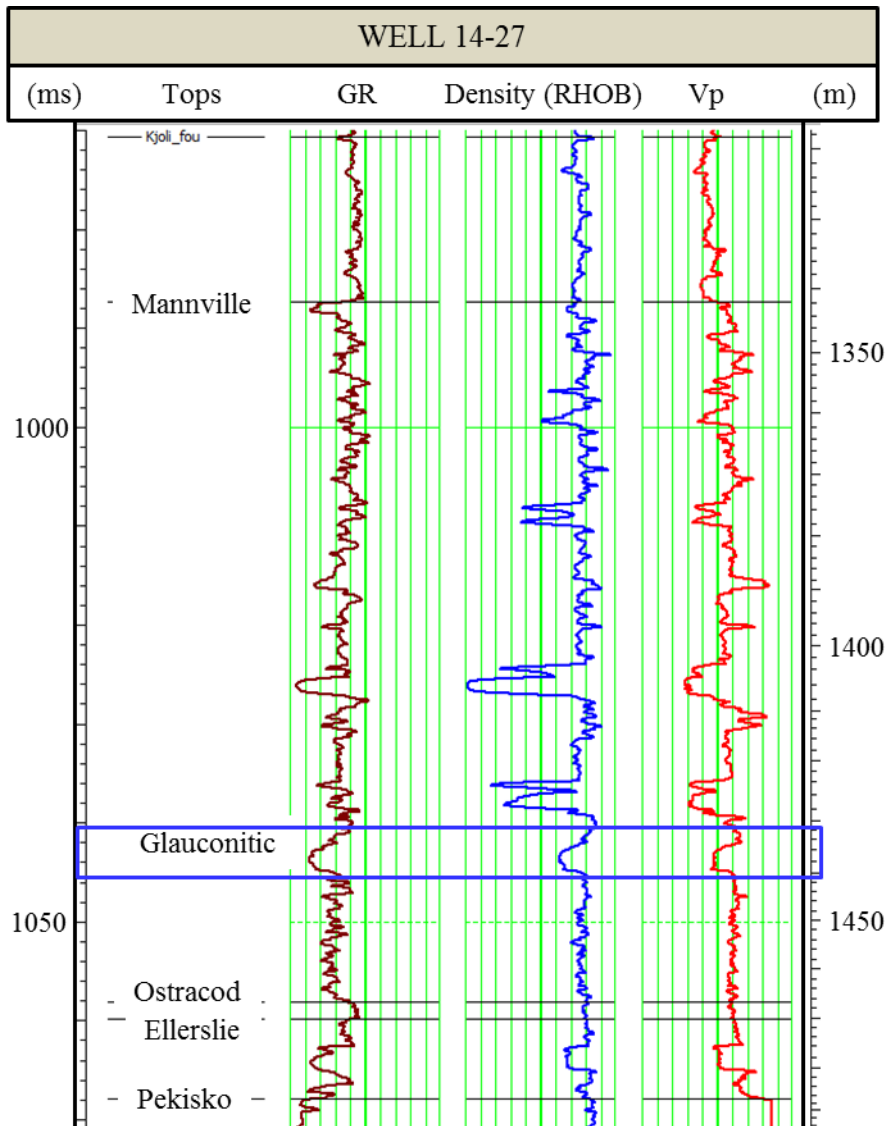


**Figure 2.6: Well 14-27. The blue rectangle highlights the Glauconitic Formation characterised with low values of gamma ray (GR), density and  $V_p$  logs.**

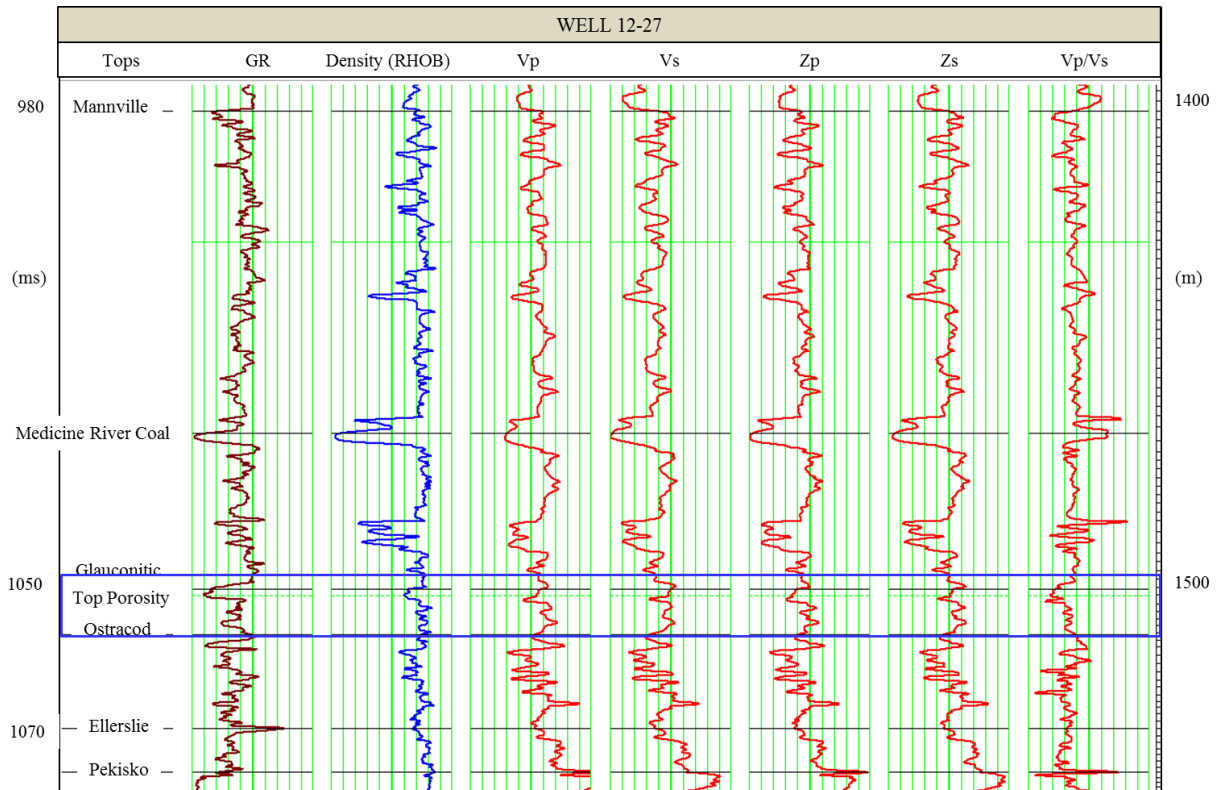


**Figure 2.7: Well 12-27. The blue rectangle highlights the Glauconitic Formation.**

### 2.2.1 Seismic Processing Considerations

The main focus was filtering the surface waves and undesired wavetrains while keeping or even enhancing the low frequency content of the reflection data. The initial unprocessed data show strong coherency down to 7.5 Hz and weak coherency to 5 Hz. Radial filter and Gabor deconvolution were applied by CREWES for noise attenuation. The data show good coherency down to 3 Hz but little in the range 0-3 Hz (Isaac and Margrave, 2011). Statics were applied and the data were post-stack Kirchhoff time migrated. As little processing as possible was applied so that the frequency content of the signal would not be compromised (Isaac and Margrave, 2011).

### 2.2.2 Vertical Resolution

The vertical resolution of the seismic data is related to the minimum resolvable bed thickness (Sheriff, 2002). The Rayleigh criterion establishes that the limit of an optical instrument to distinguish separate images of objects occurs when the two diffraction images are separated by the peak-to-trough distance of the diffraction pattern (Kallweit and Wood, 1982). Widess (1973) established the resolvability at about 1/8 of the dominant wavelength, and Sheriff (2001) defines the limit of resolution, based on the bed thickness, at 1/4 of the dominant wavelength. In this case, using an average velocity of 3400 m/s for the Glauconitic sandstone (from the P-wave velocity log), the vertical resolution in the zone of interest was determined to be ~21 m, as shown in Figure 2.8.

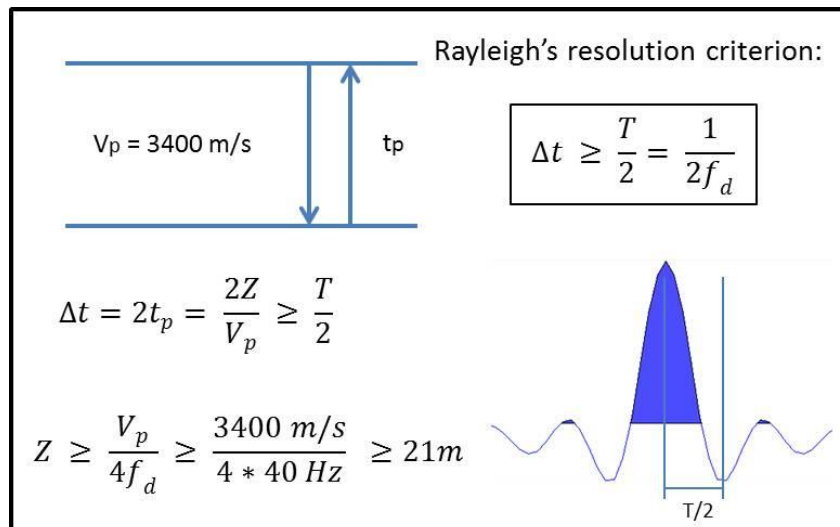


**Figure 2.8: Minimum bed thickness calculation based on Rayleigh's criterion where Z is the minimum thickness,  $V_P$  is the P-wave interval velocity,  $f_d$  is the dominant frequency,  $t_p$  is the P-wave travel time and T is the wavelength period.**

### 2.2.3 Cross plot Analysis

From a cross-plot analysis within the Mannville Group using the logs from well 12-27 it is possible to discriminate lithology and fluid content (Figures 2.9 to 2.12). The color key shows the gamma ray (GR) log where lower values (green < 50 API) correspond to cleaner sandstones (Figures 2.9 through 2.11). The red polygon highlights values for the Glauconitic Formation, with reasonably high values of  $V_P$  and  $V_S$ , P-impedance values  $\sim 9 \times 10^6 \text{ kg}/(\text{s} \cdot \text{m}^2)$  and low  $V_P/V_S$  (< 1.8) possibly indicating the presence of hydrocarbon.

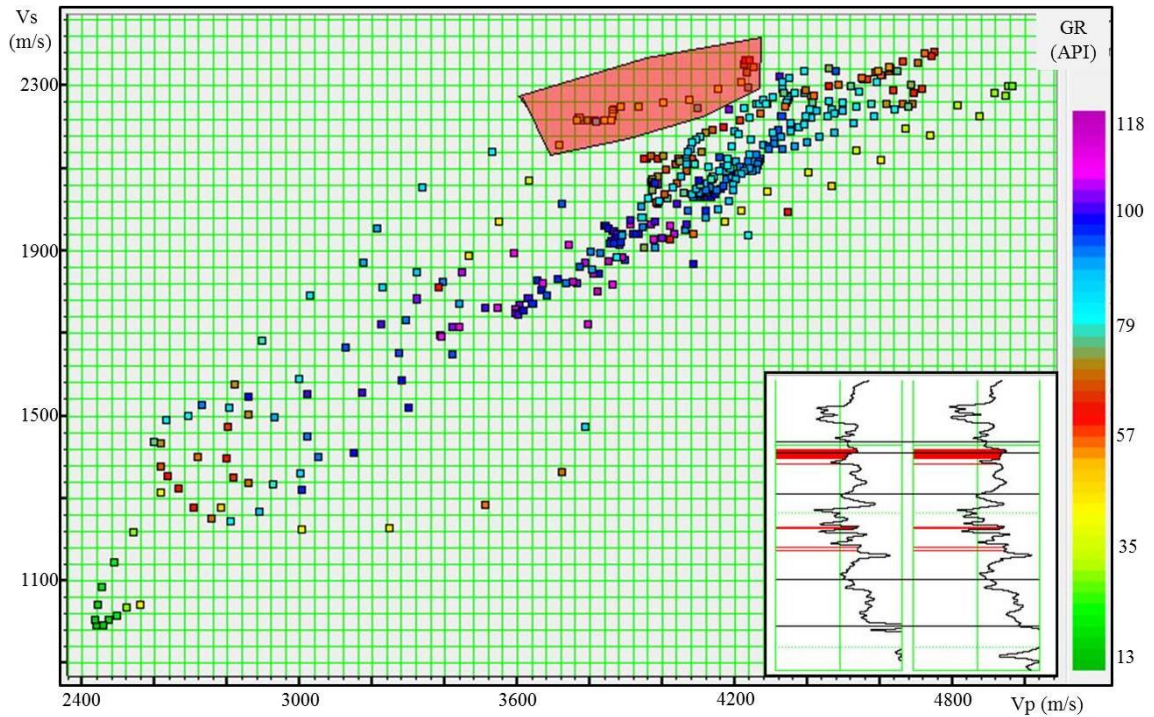


**Figure 2.9: Cross-plot  $V_P$  vs.  $V_S$  (Color: GR) in well 12-27. The red polygon highlights the Glauconitic Formation with high values for  $V_S$  and relatively high values for  $V_P$  ( $\sim 3700$ - $4300$  m/s).**

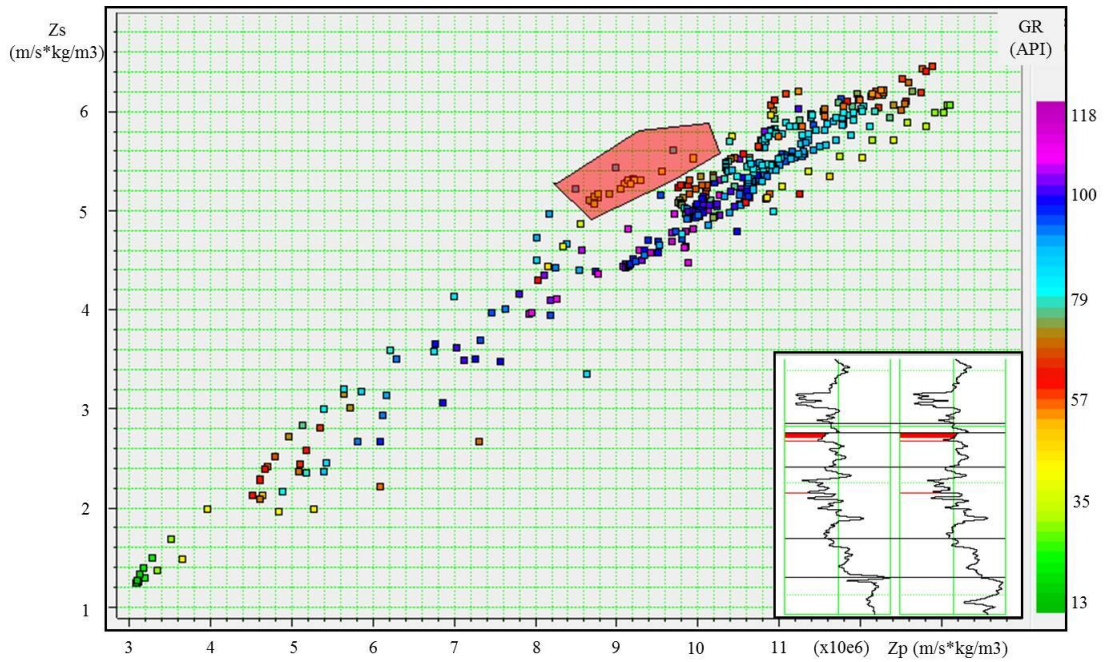


**Figure 2.10: Cross-plot  $Z_P$  vs.  $Z_S$  (Color: GR) in well 12-27. The red polygon highlights the Glauconitic Formation with relatively high values for both,  $Z_P$  and  $Z_S$  ( $\sim 9 \times 10^6$  and  $5 \times 10^6$   $kg/(s \cdot m^2)$  respectively).**

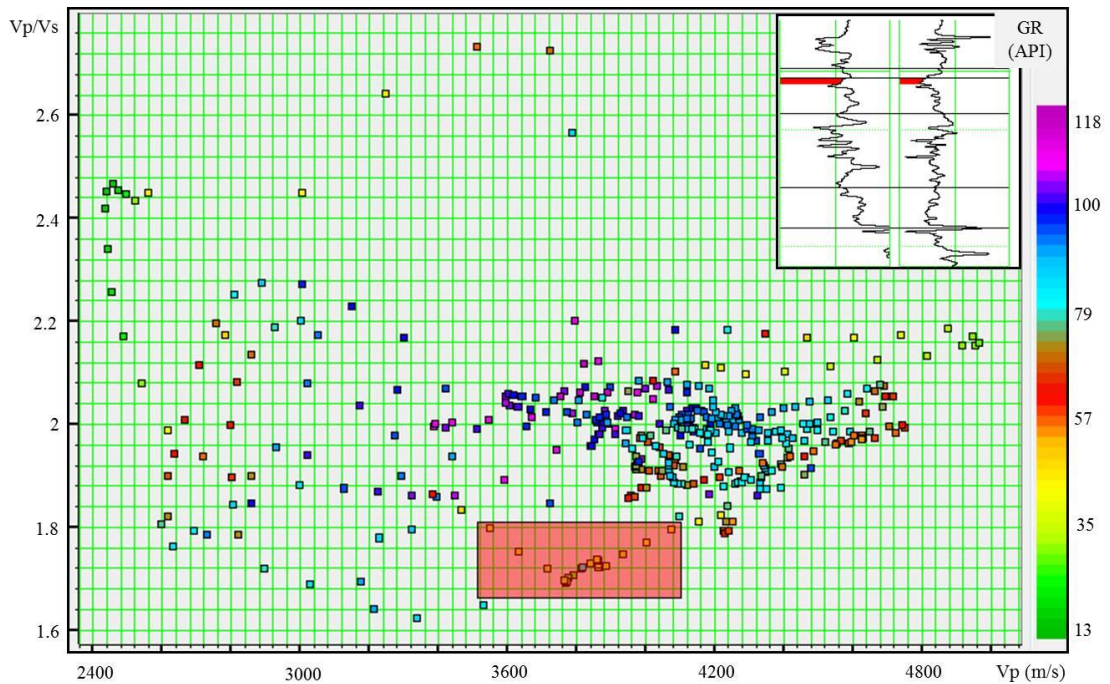


**Figure 2.11: Cross-plot  $V_P$  vs.  $V_P/V_S$  ratio (Color: GR) in well 12-27. The red polygon highlights the Glauconitic Formation with  $V_P$  values  $> 3500$   $m/s$  and  $V_P/V_S$  values  $< 1.8$ .**

Figure 2.12 shows  $V_p/V_s$  vs. GR with the lambda-rho ( $\lambda\rho$ ) property in the color bar. In this case, the isolation of the hydrocarbon producing formation is more evident with lower values for these properties; this suggests that a pre-stack inversion study may be successful for discriminating lithologies and/or fluid content by the estimation of rock properties along the seismic line such as: lambda-rho ( $\lambda\rho$ ), mu-rho ( $\mu\rho$ ),  $V_p/V_s$  and volume of shale ( $V_{Shale}$ ).

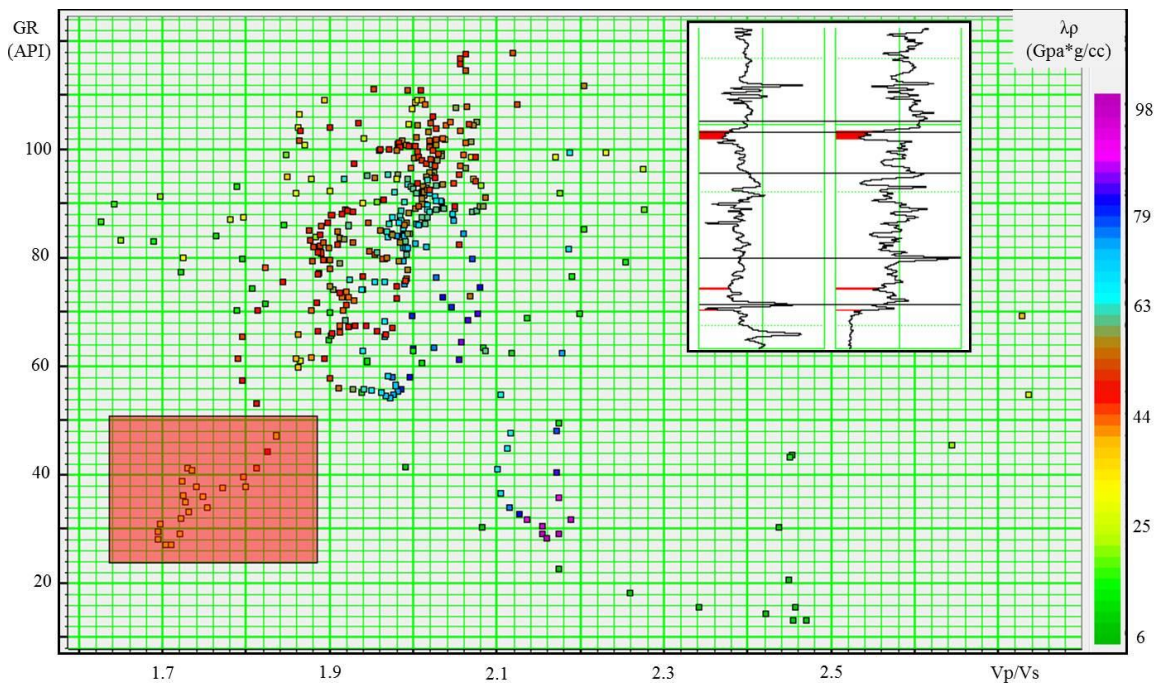


**Figure 2.12: Cross-plot  $V_p/V_s$  vs. GR (Color:  $\lambda\rho$ ) in well 12-27. The red polygon highlights the porous Glauconitic Formation with low values for  $V_p/V_s$  and GR.**

#### 2.2.4 Seismic-Well Ties

The seismic-well tie process is based in the correlation of a synthetic seismogram with the seismic data to best match the target log with the seismic attributes that will help in the interpretation of the horizons of interest. The process consists of applying a manual

check shot correction by applying bulk shifts and/or stretch and squeeze to the log and modifying the depth-to-time curve to match the P-wave seismic times.

The first step was to extract a constant phase statistical wavelet from the seismic data to start the correlation at each well. The next step was to extract a wavelet from each well and refine the correlation. The final step was extracting an optimum multi-well wavelet from well 14-27 and well 14-35 (Figure 2.13), due to the similarity in their phase ( $\sim 0^\circ$ ) and that these wells best tied the seismic data. The algorithm uses both the available wells and the seismic data near those wells. It extracts the wavelet by finding the operator which, when convolved with the reflectivity from the well, closely approximates the proximal seismic traces (Hampson-Russell Software help, 2009). The extraction time window was set from 500 to 1200 ms, with a wavelet length of 150 ms and a taper of 25 ms.

The final tie completed with this multi-well wavelet shows a good match between the synthetic seismograms and the seismic data of wells 12-27, 14-27 and 14-35. The correlation coefficient for each well is 0.801, 0.647 and 0.825, respectively. The tie is based on manually match peaks/trough of the geologic tops with the major reflectors interpreted in the seismic data plus some time shift to generally adjust the depth-time curve. Figure 2.14 to Figure 2.16 show the result of the seismic-well tie process.

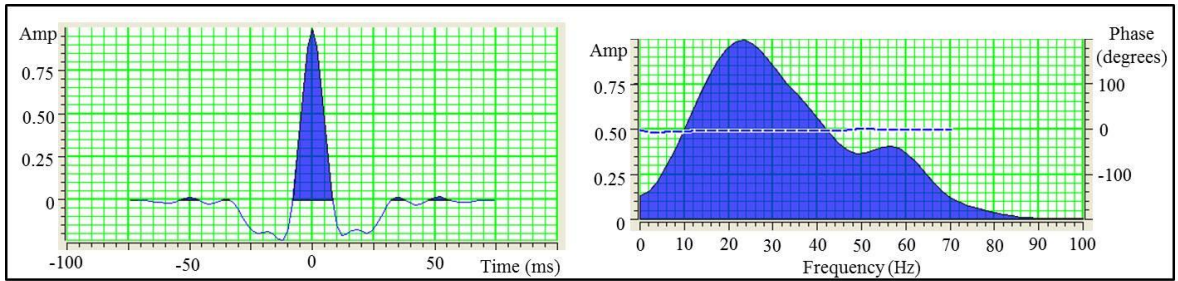


**Figure 2.13: Multi-well wavelet extracted from wells 14-27 and 14-35 with its amplitude spectrum. The dotted line indicates the average phase of the wavelet.**

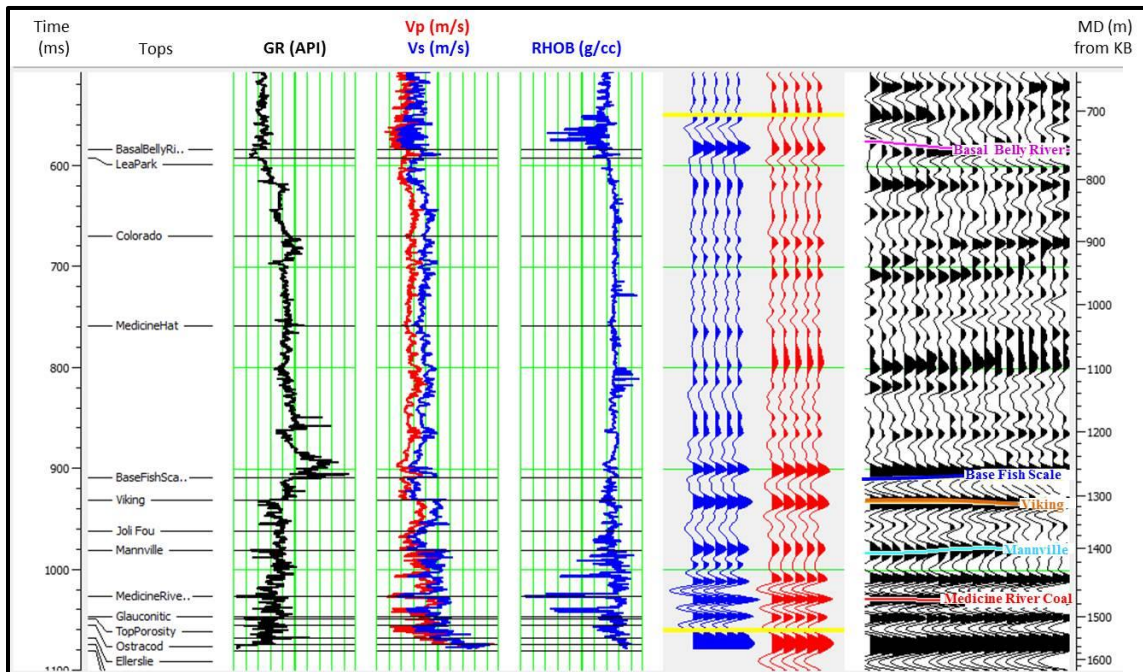


**Figure 2.14: Final tie of well 12-27 with the multi-well wavelet. Blue traces represent the synthetic seismogram; red traces represent the extracted trace from the seismic data at the well location, and black traces shows the ten traces around the well location. Yellow bars show the correlation window.**

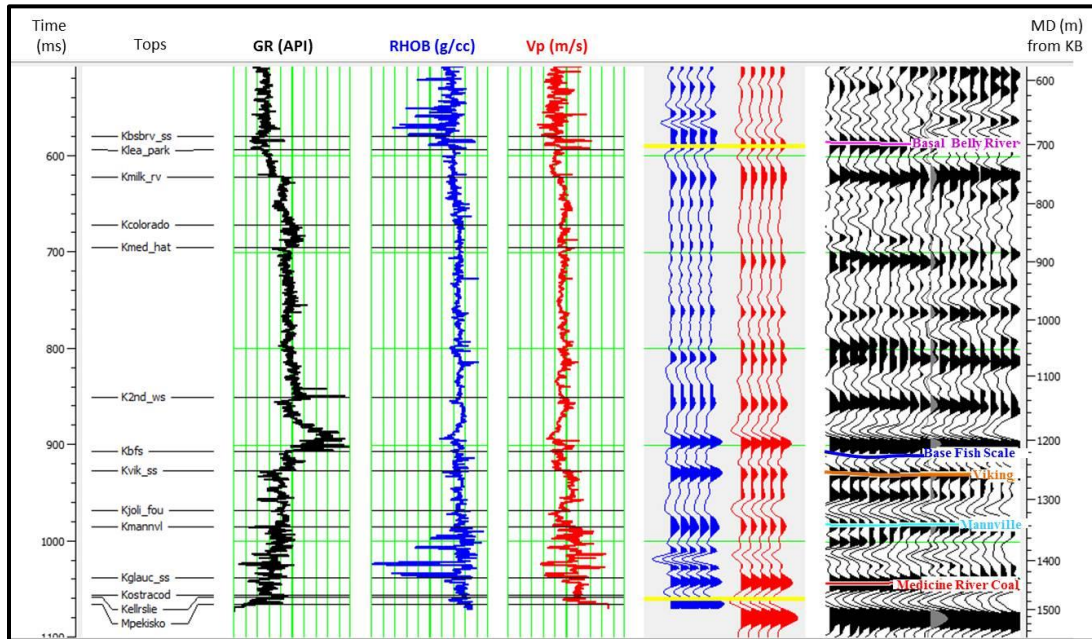


Figure 2.15: Final tie of well 14-27 with the multi-well wavelet. Blue traces represent the synthetic seismogram; red traces represent the extracted trace from the seismic data at the well location, and black traces shows the ten traces around the well location. Yellow bars show the correlation window.

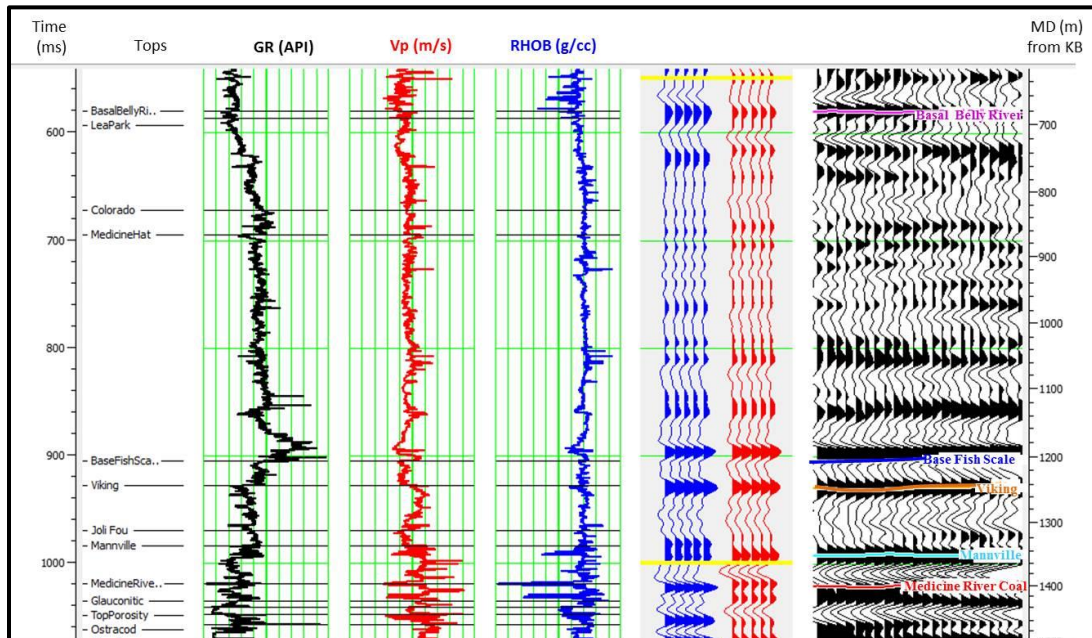
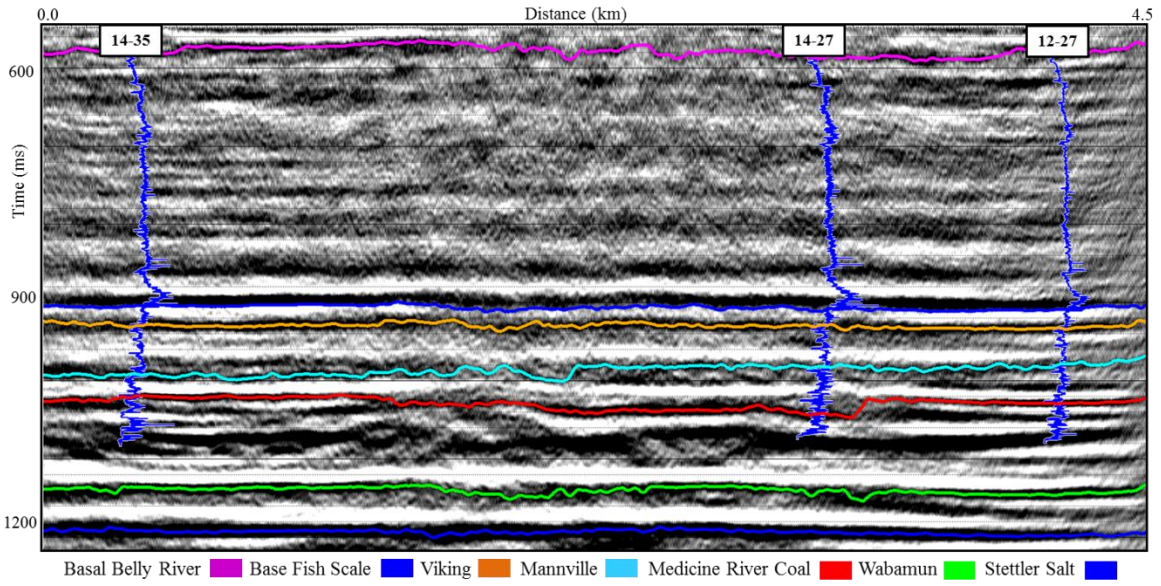


Figure 2.16: Final tie of well 14-35 with the multi-well wavelet. Blue traces represent the synthetic seismogram; red traces represent the extracted trace from the seismic data at the well location, and black traces shows the ten traces around the well location. Yellow bars show the correlation window.

The Glauconitic sandstone was hard to tie because it is probably masked by the Medicine River Coal which is a highly reflective marker in the area. Figure 2.17 shows the tie results of all the wells on the seismic section.



**Figure 2.17: Seismic section with wells 14-35, 14-27 and 12-27 after seismic-wells tie process.**

## 2.3 Model-based Inversion

### 2.3.1 The Initial Model

The initial background model was formed by blocking an impedance log from a well. The final result is dependent on the initial model so the model must be low-pass filtered to reduce this effect (Lindseth, 1979). Lloyd (2012) produced a good inversion result at the well 12-27 location using a low cut-off of 3 Hz for the 4.5 Hz geophone receivers and found that consistent low-frequency information is present in the dynamite data as low as 1 Hz. To identify an initial model low-frequency cut-off point, several band-pass filters were applied to the seismic data to best estimate which frequency range

is missing (Figure 2.18). Based on the amplitude spectrum and the filter tests, it is difficult to identify any coherent signal below 4 Hz, suggesting that our low-frequency cut-off can be defined around this value.

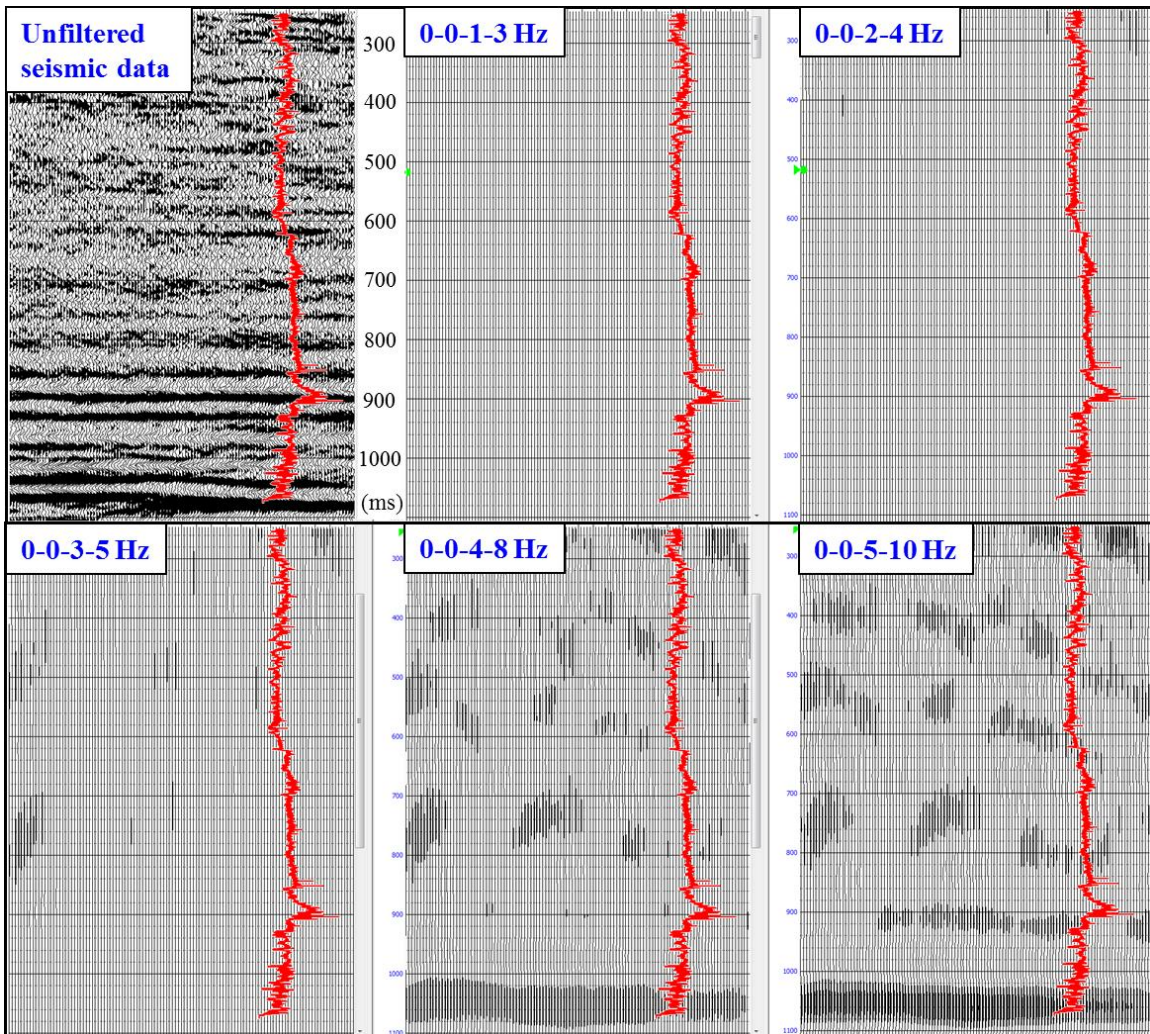


**Figure 2.18: Filter panels assessing low frequency data present in the seismic data. The unfiltered seismic data are displayed for reference. The red curve is the GR log. The amplitude scalar is constant at 10.6528.**

Figure 2.19 shows an example of the impedance ( $Z_p$ ) initial model generated using the P-impedance logs calculated from the sonic and density logs from well 14-35

with a low-pass filter of 0-0-3-5 Hz. P-impedances in the model range from  $6 \times 10^6$  to almost  $12 \times 10^6$  kg/(s\*m<sup>2</sup>). The 2D impedance model was generated by interpolating the impedance at the well location using the Basal Belly River, Base Fish Scale and Stettler Salt picked horizons to guide the interpolation. The extrapolation at the top and bottom of the well curve is based on compaction trends in the well. The program uses a least squares fit to determine a trend to use for the top and bottom of the well (Dutta et al., 2009).

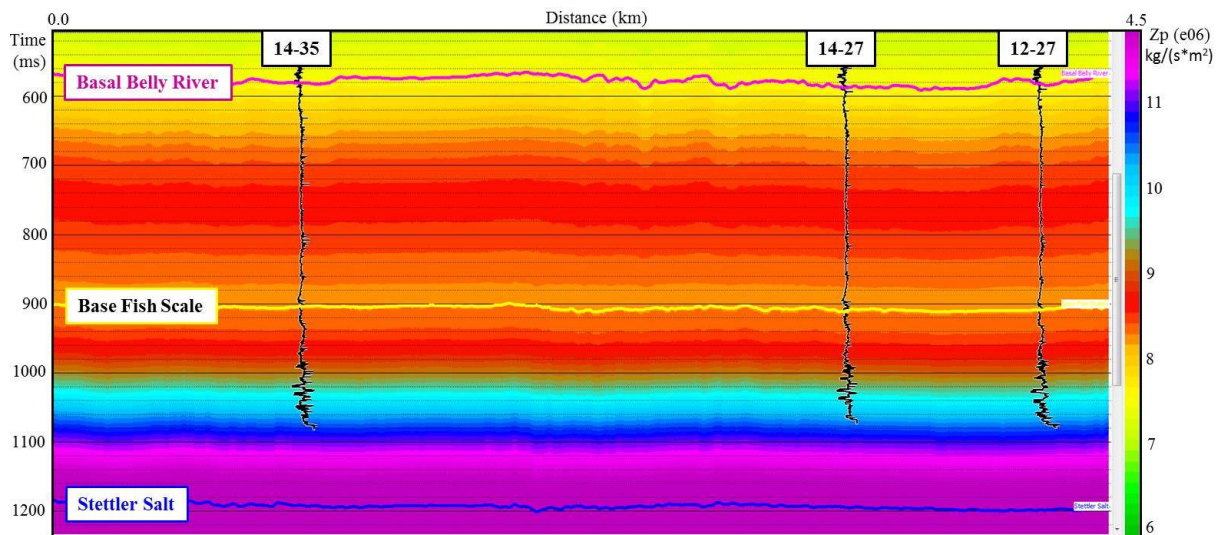


**Figure 2.19: Initial low frequency P-impedance model (0-0-3-5 Hz) using the Well 14-35 and the horizons Basal Belly River, Base Fish Scale and Stettler Salt. The inserted black curve is the GR log.**

### 2.3.2 Inversion Analysis

A post-stack inversion analysis was initially performed at the location of the well 14-35, focused on a window from 500 to 1100 ms, to evaluate the efficacy of the inversion by comparing the impedance at the well with the impedance inverted from the seismic data for each of 4 initial models (0-3 Hz, 0-4 Hz, 0-5 Hz and 0-8 Hz). The

impedance was inverted from a single trace at the well location and the resulting reflectivity sequence was then convolved with an extracted wavelet to produce a synthetic trace that was compared with the actual seismic trace at that location. The correlation between the synthetic (red) and the seismic trace (black) is good in all the cases with high correlations coefficients (over 0.99). The estimated RMS error between the synthetic trace and the seismic trace is 0.13. The estimated RMS errors between the inverted trace and the impedance log were  $8.11 \times 10^5$ ,  $7.35 \times 10^5$ ,  $7.30 \times 10^5$  and  $7.16 \times 10^5$   $\text{kg}/(\text{s} \cdot \text{m}^2)$  for each model, corresponding to 6.8, 6.1, 6 and 5.9 %, respectively; as shown in Figure 2.20 through Figure 2.23. As mentioned previously, the inversion result is band-limited and fails to reproduce the higher frequency details observed in the wells logs. To make a fair comparison, well logs were filtered using a high-cut filter of 60/85 Hz. Within the Colorado Group the inversion estimates values are very close to the actual impedance; meanwhile, within the Mannville Group the inverted impedance shows the general trend and some local variations, but several units within the Mannville Group are below the seismic vertical resolution (thicknesses  $< \sim 21$  m), in which case, the amplitudes of the recorded seismic data could be affected by interference effects from surrounding layer boundaries.

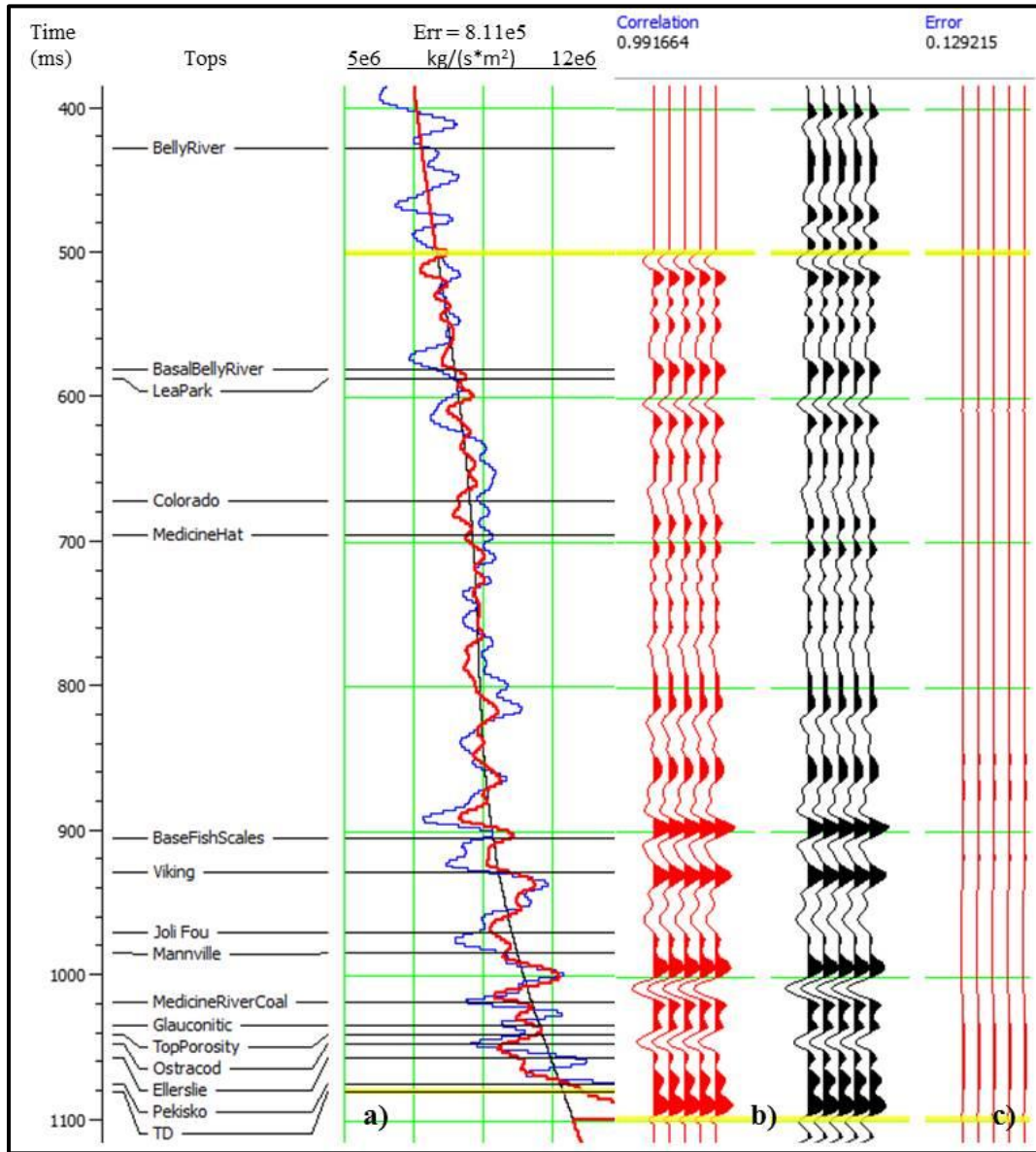


**Figure 2.20: Analysis of the post-stack inversion at Well 14-35 with the initial model cut-off of 0-3 Hz: a) filtered impedance log (blue), initial model (black), inversion result (red); b) synthetic trace from inversion (red) and extracted trace from the seismic (black), and c) RMS error between synthetic trace and seismic trace.**

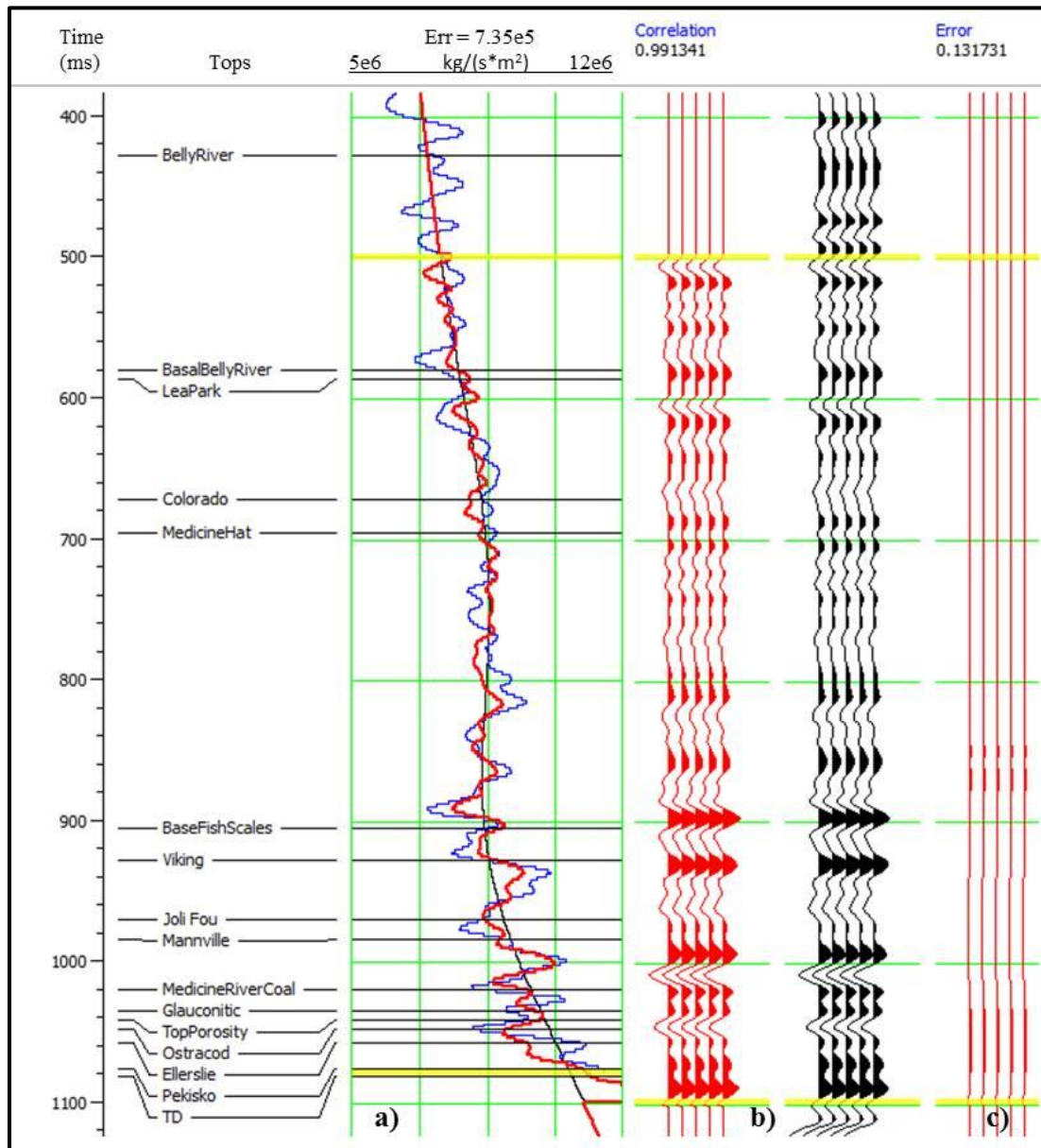


**Figure 2.21: Analysis of the post-stack inversion at Well 14-35 with the initial model cut-off of 0-4 Hz: a) filtered impedance log (blue), initial model (black), inversion result (red); b) synthetic trace from inversion (red) and extracted trace from the seismic (black), and c) RMS error between synthetic trace and seismic trace.**

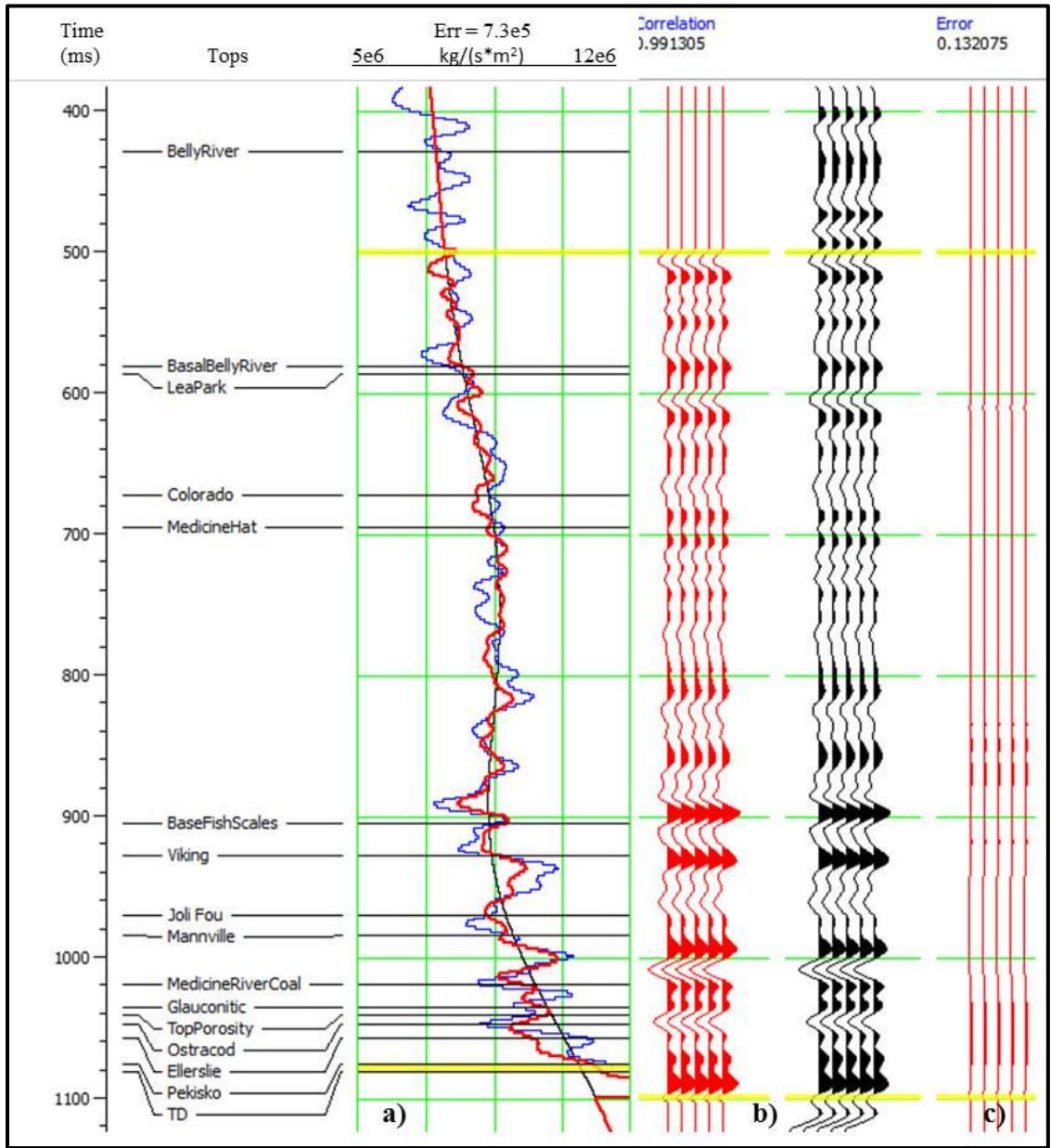


**Figure 2.22: Analysis of the post-stack inversion at Well 14-35 with the initial model cut-off of 0-5 Hz: a) filtered impedance log (blue), initial model (black), inversion result (red); b) synthetic trace from inversion (red) and extracted trace from the seismic (black), and c) RMS error between synthetic trace and seismic trace.**

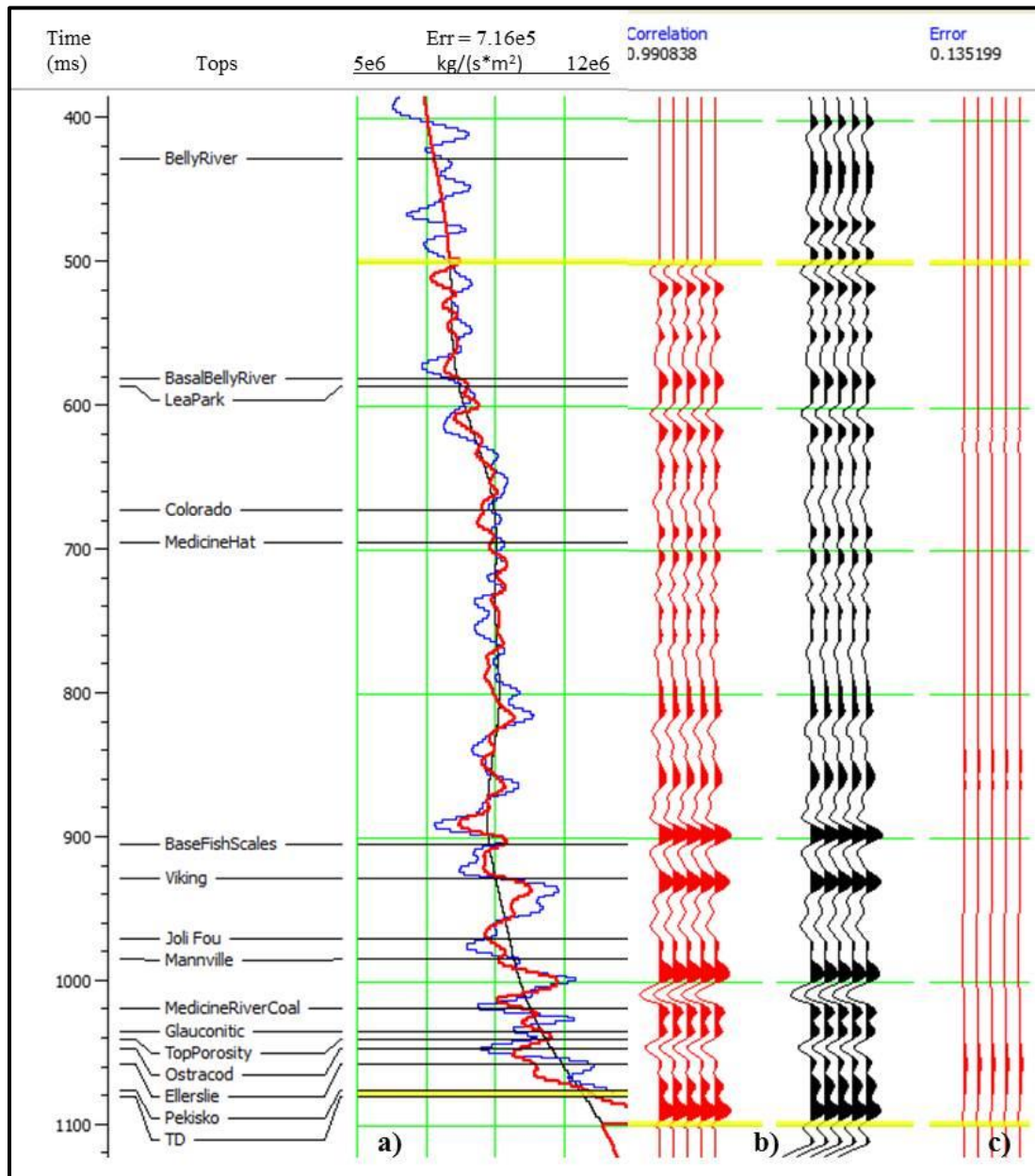


**Figure 2.23: Analysis of the post-stack inversion at Well 14-35 with the initial model cut-off of 0-8 Hz: a) filtered impedance log (blue), initial model (black), inversion result (red); b) synthetic trace from inversion (red) and extracted trace from the seismic (black), and c) RMS error between synthetic trace and seismic trace.**

To assess the inversion results elsewhere along the seismic line, a blind test was done with the wells that were not used to build the model or used in the inversion analysis. Figure 2.24 and Figure 2.25 shows the results for Well 12-27 and 14-27 respectively. The results look very similar for all the initial models.

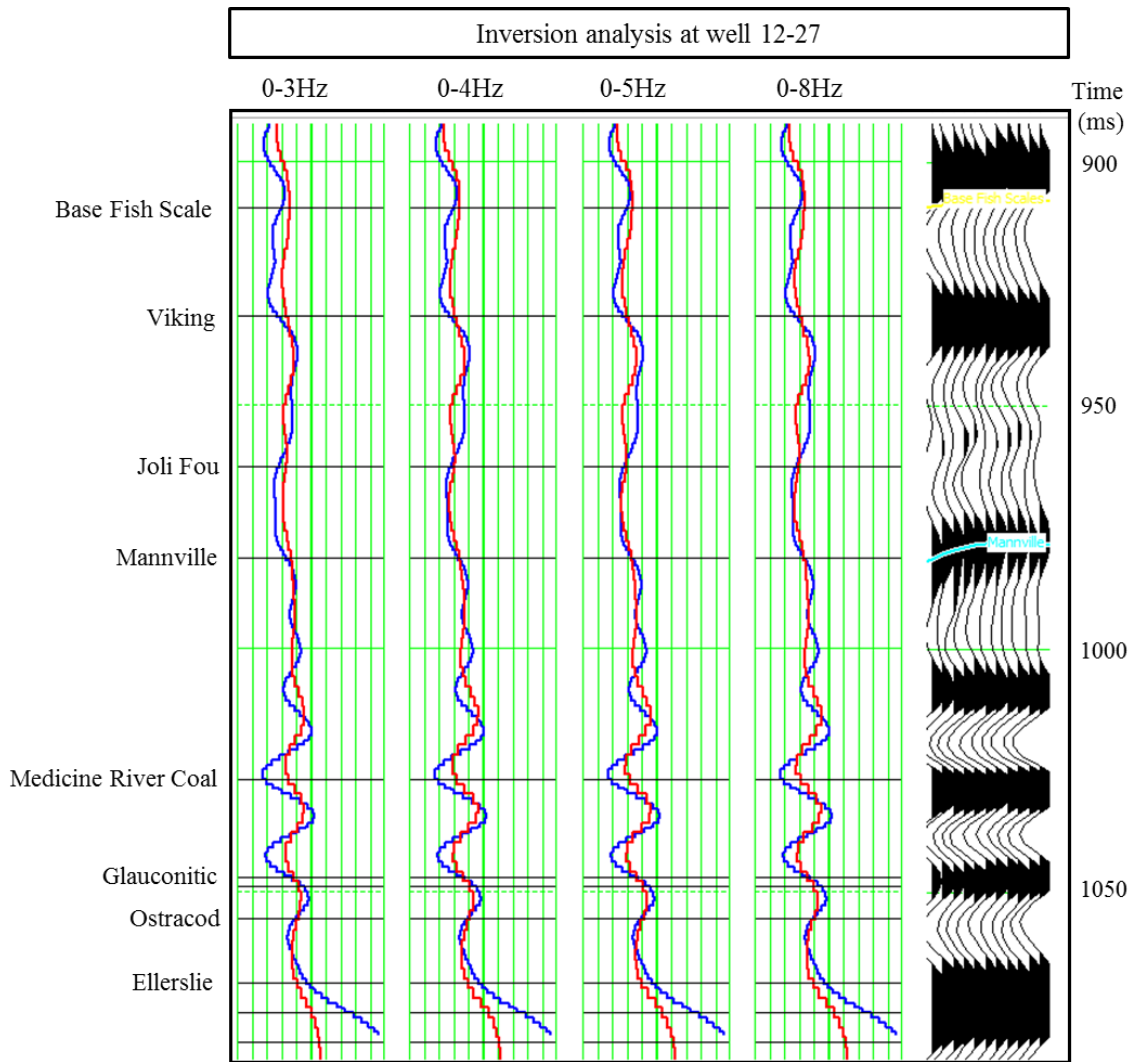


**Figure 2.24: Analysis of the post-stack inversion at Well 12-27: Impedance log (blue), inversion result (red) for each initial model.**

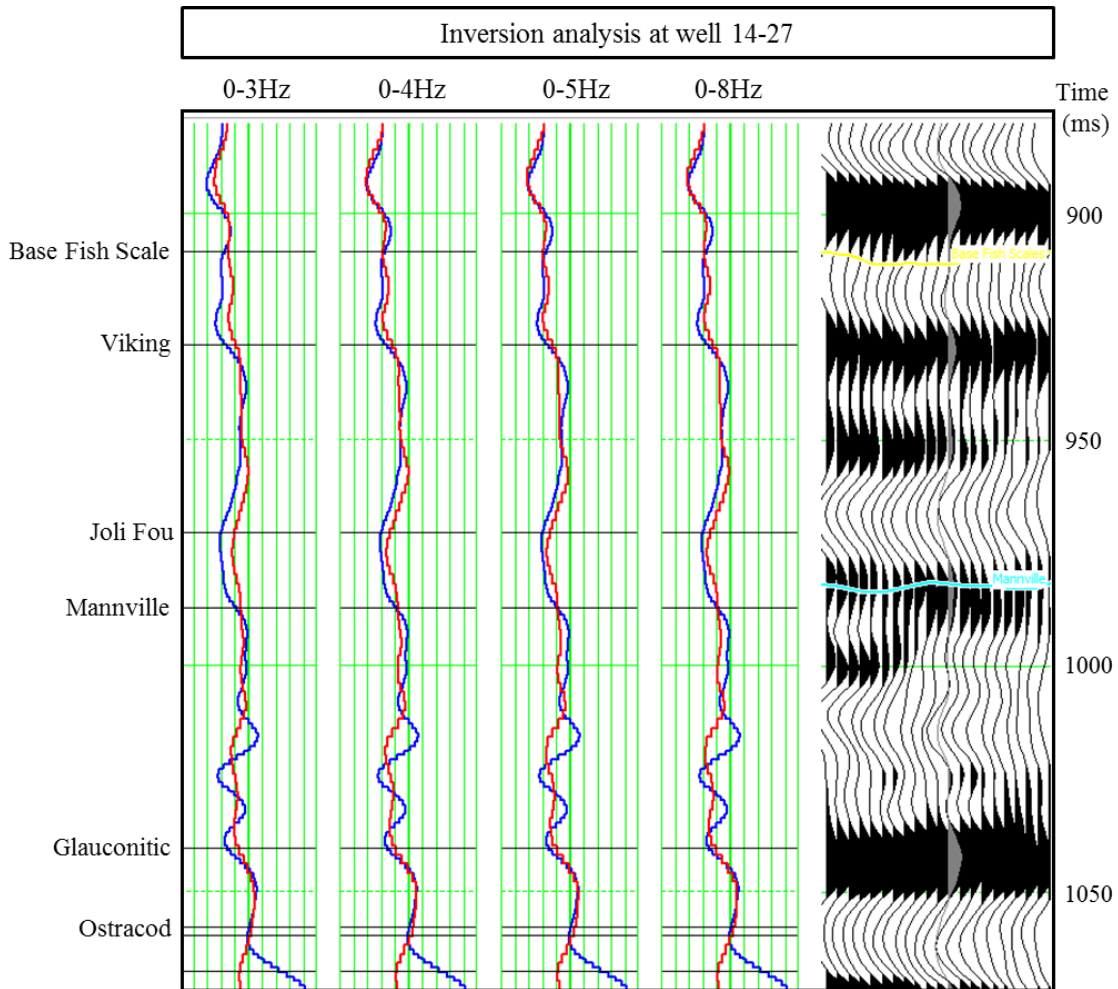


**Figure 2.25: Analysis of the post-stack inversion at Well 14-27: Impedance log (blue), inversion result (red) for each initial model.**

Figures 2.26, 2.27 and 2.28 show a cross-plot analysis between the impedance log and the inverted impedance curve for all the initial models, for each well. A small improvement in the correlation is seen when a higher limit to the low-frequency component is added, with the exception of the Well 14-27 where the correlation remains invariant at ~62% for all cases.

Wells 14-35 and 12-72 show similar behaviour, the correlation is lower for the 0-3 Hz model, which is expected since there is a gap in the low-frequency component

between the initial model and the seismic data which shows signal from about 4 Hz as demonstrated in Figure 2.18. Since the 0-8 Hz model creates more overlap between the low frequencies from the seismic and those from the model, the 0-5 Hz model was chosen as optimum for the inversion.

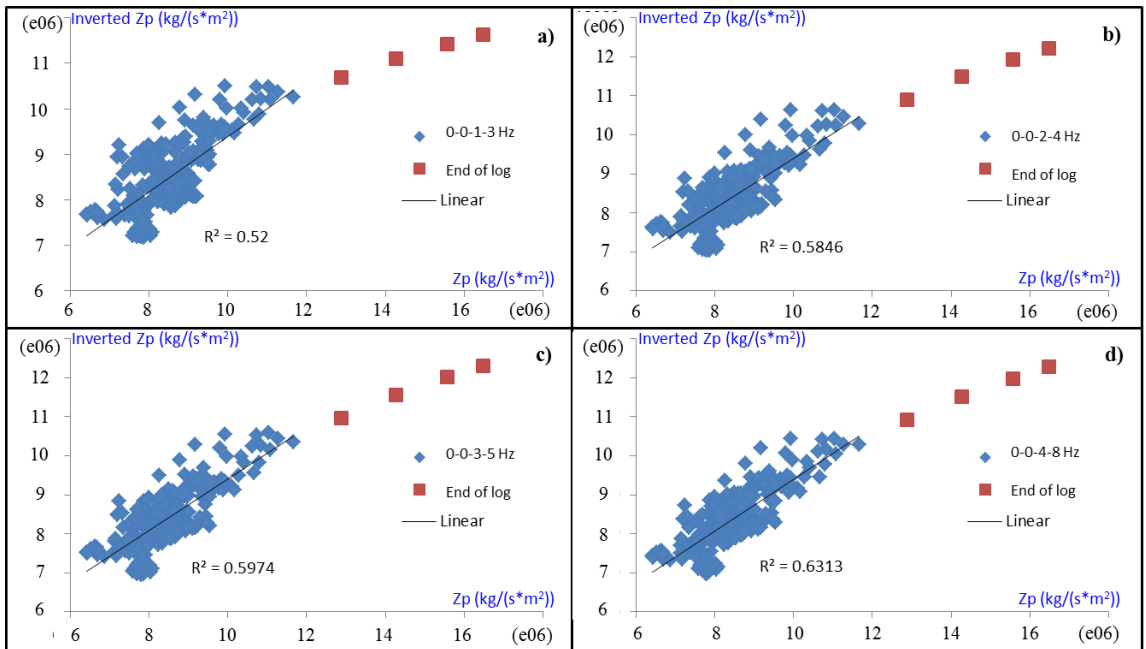


**Figure 2.26: Impedance log vs. Inverted impedance plots for Well 12-27 for each initial model: a) 0-3 Hz, b) 0-4 Hz, c) 0-5 Hz and d) 0-8 Hz. The correlation increases when a higher limit to the low-frequency component is added.**

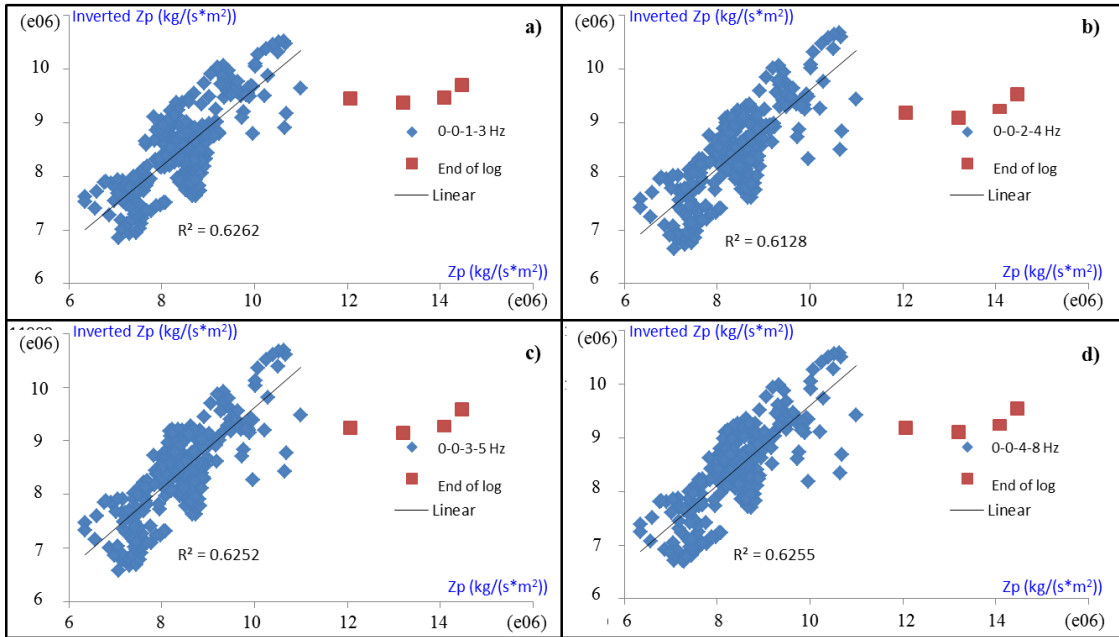


**Figure 2.27: Impedance log vs. Inverted impedance curve plots for Well 14-27 for each initial model: a) 0-3 Hz, b) 0-4 Hz, c) 0-5 Hz and d) 0-8 Hz. The correlation remains stable for all the cases.**

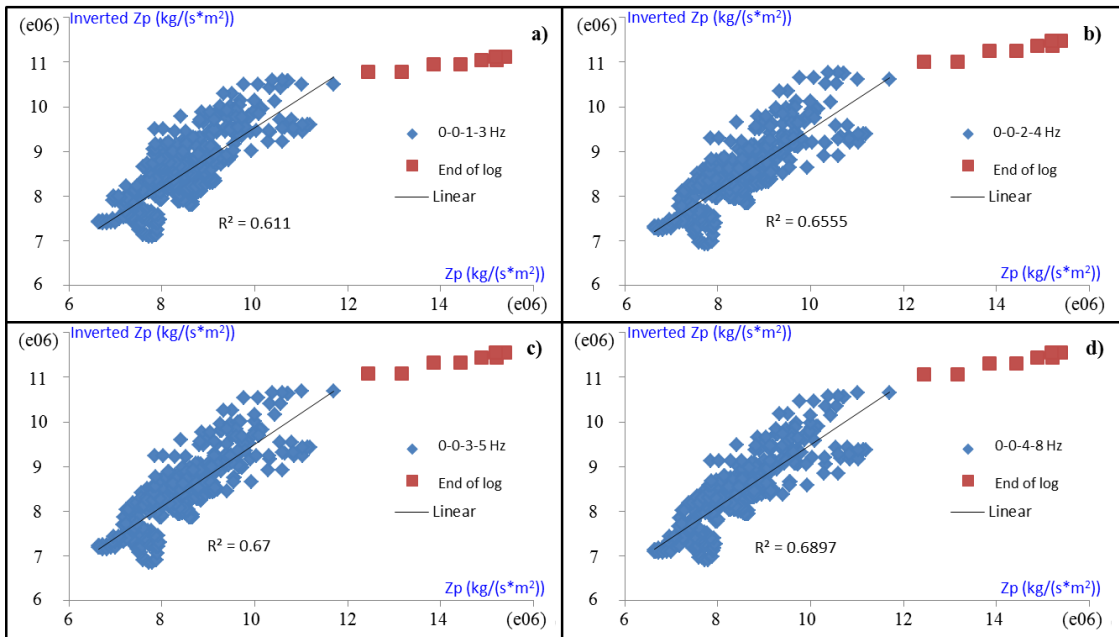


**Figure 2.28: Impedance log vs. Inverted impedance curve plots for Well 14-35 for each initial model: a) 0-3 Hz, b) 0-4 Hz, c) 0-5 Hz and d) 0-8 Hz. The correlation increases when a higher limit to the low-frequency component is added.**

### *2.3.3 Inversion Results*

Following the analysis at the well locations, model-based inversion of the seismic data was undertaken using the 0-0-3-5 Hz model and the multi-well wavelet (Figure 2.13) resulting from the seismic-well tie process.

A single value for a hard constraint of 100% was used, indicating that the initial model could be freely modified. The inversion result (Figure 2.29) shows zones of low impedance (green-yellow) within the Colorado Group (Fish Scale Zone) and Upper Mannville units (Glaucinitic and Medicine River Coal). Higher impedance values correspond to more shaly units (Figure 2.29). The P-impedance log filtered with a high cut of 60/85 Hz was inserted for comparison with the inversion result.

The members within the Mannville Group are not as evident as those in the Colorado Group probably because of resolution limitations. Most of these units have thicknesses below the seismic vertical resolution, as discussed previously. However, the inverted impedance shows the general trend and similar relative variations. The coal section was identified along the Medicine River Coal marker with impedance values closer to the log values. Around 1070 ms a low impedance anomaly is seen between wells 12-27 and 14-27 which can be related to a channel within the Ellerslie Formation which is overlain by high impedance rocks possibly related to the shale unit of the Ostracod Formation.

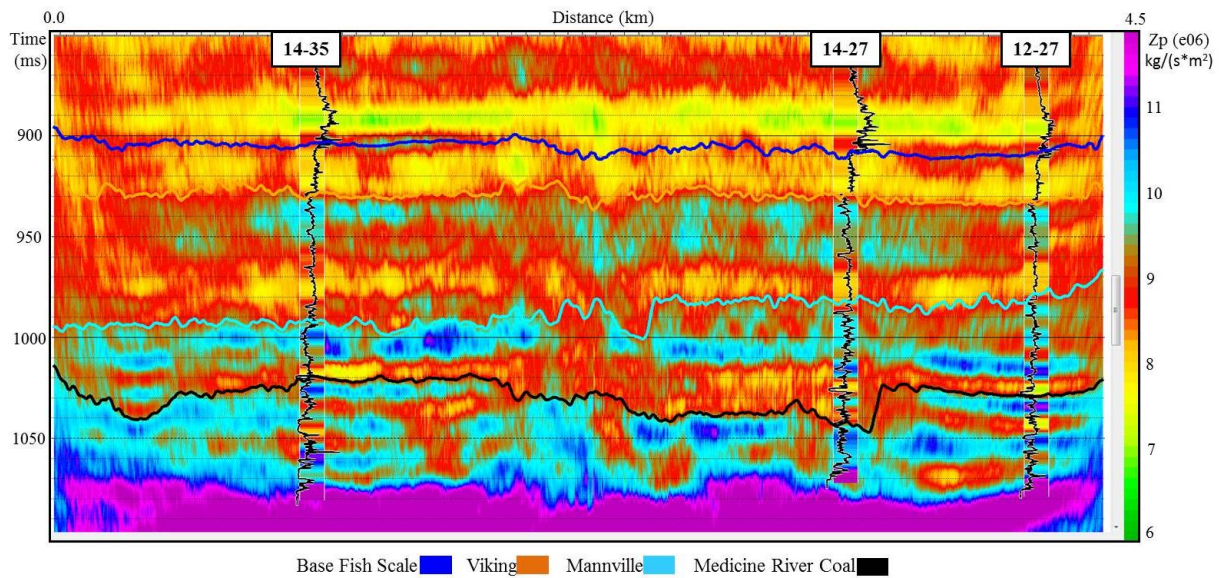


**Figure 2.29: Inversion result of Hussar 10 Hz dynamite dataset showing the GR curve in black and the impedance log with a high-cut filter 60/85 Hz in color at the well locations for comparison.**

The result shows lateral variations in the impedances that were not present in the initial model, which showed a general trend of increasing the impedance but without significant lateral variations. The changes observed in the resultant impedance reflect the character of the seismic reflection data, indicating that the inversion process was influenced by the seismic data.

In comparison, when a band-pass filter was applied to the input data to remove the low-frequency component recorded; this simulated the traditional case when the low-frequency component is missing in the seismic data. A post-stack inversion section was generated using the same parameters except using the new initial model. In this case, the seismic bandwidth was 10-15-60-85 Hz and the initial model had a frequency cut-off of 0-0-10-15 Hz. Figure 2.30 shows the inversion result; interesting differences can be seen compared to the results shown in Figure 2.29. At the well locations there is a good

impedance match, but the lateral impedance variations and intensity of some events are diminished and, in general, the inverted section resembles more the initial model response (Figure 2.19).

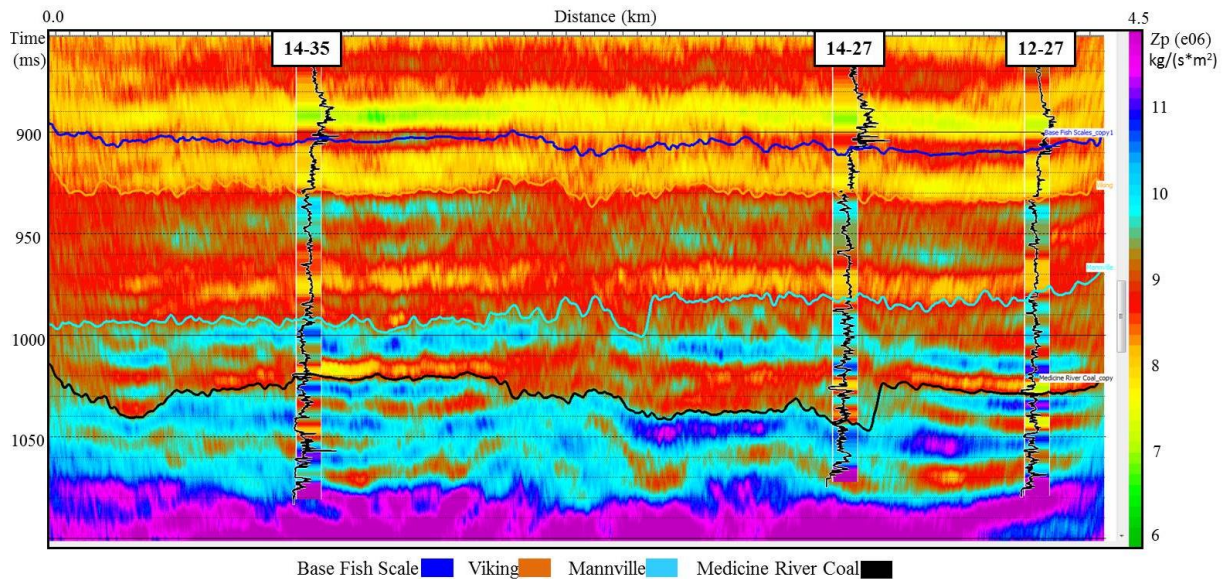


**Figure 2.30: Inversion result of Hussar 10 Hz dynamite dataset with a band-pass filter of 10-15-60-85 Hz showing the GR curve in black and the impedance log with a high-cut filter 60/85 Hz in color at the well locations for comparison. Note the differences in continuity and character of the events with respect to the results on Figure 2.29.**

## 2.4 Summary

A model-based post-stack inversion study was undertaken using the low-frequency seismic data from the Hussar experiment acquired with 3C 10 Hz geophones and a source of 2 kg of dynamite to evaluate if the inversion result improves when there is low dependence on the initial model that sometimes strongly influences the inversion result. Four initial inversion models were tested with different low-frequency cut-offs. These all had similar results but the 0-0-3-5 Hz model was chosen to invert the seismic

data since this model did not include much overlap between the low frequencies within the seismic data and those from the initial model. The initial model and the inversion were undertaken with control from Well 14-35 while wells 12-27 and 14-27 were used as blind tests.

The impedance determined from the inversion reflects the changes due to the seismic reflection data more than the influence of the initial model. Impedance changes in the target zone were not as detailed as expected, possibly due to limitation in seismic resolution; however, the inverted impedance shows the general trend and relative variations which might allow monitoring changes in the reservoir to be identified when changes in the rock properties occur due to fluid injection.

A final inversion was calculated to verify results. A band-pass filter of 10-15-60-85 Hz was applied to the seismic data to remove the low-frequency component gained during the Hussar experiment. An initial inversion model was built with a frequency cut-off of 0-0-10-15 Hz to invert this seismic data and the results at the well locations showed a good match but the lateral impedance variations and intensity of the events were subtle and resembled more the initial model character. This is observed when the low-frequency component is missing in conventional seismic data.

## CHAPTER 3: NISKU SEISMIC DATA

### 3.1 Wabamun Area CO<sub>2</sub> Sequestration Project Overview

#### 3.1.1 Introduction

The Wabamun Area CO<sub>2</sub> Sequestration Project (WASP) was a University of Calgary led multi-disciplinary project funded by the National Science and Engineering Research Council (NSERC) and Alberta Energy Research Institute (AERI) with industrial partnership that investigated the feasibility of the storage of 20 million tonnes of CO<sub>2</sub> annually over 50 years in a 5000 km<sup>2</sup> area into the deep saline aquifer Nisku Formation (Alshuhail, 2011). The study found that about half of the targeted storage capacity - or some 500 million tonnes of CO<sub>2</sub> - can be accomplished without exceeding the pressure limitations of the geologic formation into which the CO<sub>2</sub> would be injected. This is a large volume of storage, roughly equivalent to half the emissions for 30 years from all of Alberta's centrally located coal-fired power plants (WASP, 2010: [www.ucalgary.ca/wasp](http://www.ucalgary.ca/wasp)).

Results from WASP were planned to assist TransAlta Corporation and its partners in implementing Project Pioneer to capture one million tonnes of CO<sub>2</sub> annually at its Keephills 3 coal-fired power plant in the Wabamun area. On April 2012, following the conclusion of the feasibility study, the industry partners determined that the market for carbon sales and the price of emissions reductions were insufficient to allow the project to proceed (Project Pioneer, 2012: <http://www.projectpioneer.ca/>). CO<sub>2</sub> captured at the site would have been used for EOR opportunities in the Pembina Oil Field (2,600 to 2,800 m underground) or transported by pipeline to the sequestration site to be injected approximately 2 km underground into the Nisku Formation, a Devonian saline aquifer.

Despite the cancellation of Project Pioneer, the information is available as a source of reference and the affiliation between the CREWES Project with Carbon Management Canada (CMC) allows the possibility of having access to the data for further analysis. Seismic data were provided by TransAlta and Canadian Natural Resources Limited (CNRL), and Schlumberger provided the well log information used in this dissertation.

The objective of this chapter is to compare the effect of using a dataset processed with different approaches in an inversion study. These approaches are based on a previously conditioned dataset with a conventional processing flow versus applying a specialized processing flow focused on attaining coherent noise without compromising low-frequency signal. Chapter 3 describes the processes applied to the seismic data to further create a detailed geologic model of the study area. The methodology includes: geology overview, acquisition, processing, and review of WASP study with new log data, seismic interpretation and seismic inversion. Chapter 4 will use the information analyzed in this chapter to conduct a 2D seismic modelling study to simulate a CO<sub>2</sub> injection scenario in the Nisku Formation.

### *3.1.2 Geology Overview*

The sedimentary succession in the Wabamun Lake area overlays the Precambrian basement and has a maximum thickness of ~3000 m. It is characterized at its base by passive margin sediments of Cambrian to Jurassic age (evaporates, marine carbonates and shales). During the Cretaceous until present time, the upper part is formed by coarse to fine siliciclastic sediments that were deposited in the Rocky Mountain foreland basin

(Michael et al., 2008). The sedimentary succession gently dips southwest. No major faults are known in the area (Figure 3.1).

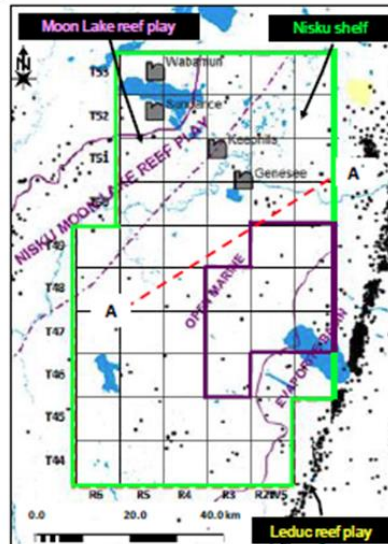
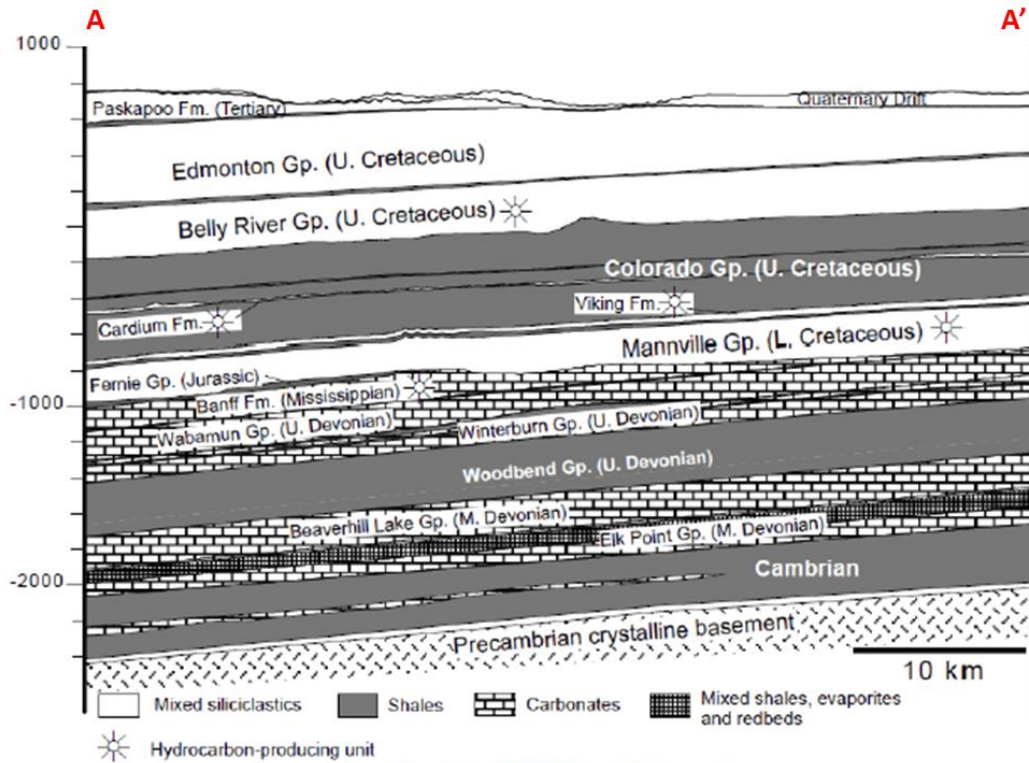


**Figure 3.1: Regional geologic cross-section across the WASP study area (green polygon) in the northeast-southwest direction. The dashed line in the (A-A') in the map indicates the location of the section (modified from Alshuhail, 2011).**

### 3.1.2.1 Geological Framework and Stratigraphic Units:

In the WASP study area, the Nisku Formation corresponds to a carbonate ramp deposited in a transgressive system tract period (Switzer et al., 1994). It can be described as carbonate member of the Winterburn Group that is conformably overlain by the Calmar Formation of the Winterburn Group and is underlain by the Ireton Formation of the Woodbend Group (Figure 3.2) (Watts, 1987; Switzer et al., 1994).

Project Pioneer identified the Winterburn Group as a potential storage complex. Underlying the Nisku formation is the Ireton formation, which is a regional shale that should form the bottom seal of the Winterburn storage complex. The interbedded shales and carbonates of the Calmar, Blueridge, and Graminia formations form the upper portion of the Winterburn Group and were expected to act as a primary seal for CO<sub>2</sub> injection into the Nisku Formation which should prevent injected CO<sub>2</sub> from migrating into the surface or shallow aquifers (Michael et al., 2008). The Exshaw Formation overlies the Wabamun Group and is a regional sealing shale able to serve as a secondary seal (Figure 3.3).

The CO<sub>2</sub> sequestration target is the Upper Devonian dolomitic Nisku Formation which has a thickness range of 40-100 m and a depth range of 1700-2200 m (Watts, 1987). In the WASP study area, the Nisku Formation can be divided into three distinct regions (Figure 3.2) (Watts, 1987; Switzer et al., 1994):

- 1) To the east, the Nisku evaporite basin is composed primarily of anhydrite lithofacies with mixture of dolomite and mudstone and is interbedded with shale.

- 2) In the middle, the Nisku shelf consists mainly of fossil-bearing open marine dolomitized carbonate lithofacies.
- 3) In the northwest, the Nisku shale basin is dominated by shale lithofacies but contains some reef build-ups. The Nisku shelf and shale basin are separated by the Nisku ramp, which is characterized by clastic carbonate lithofacies.

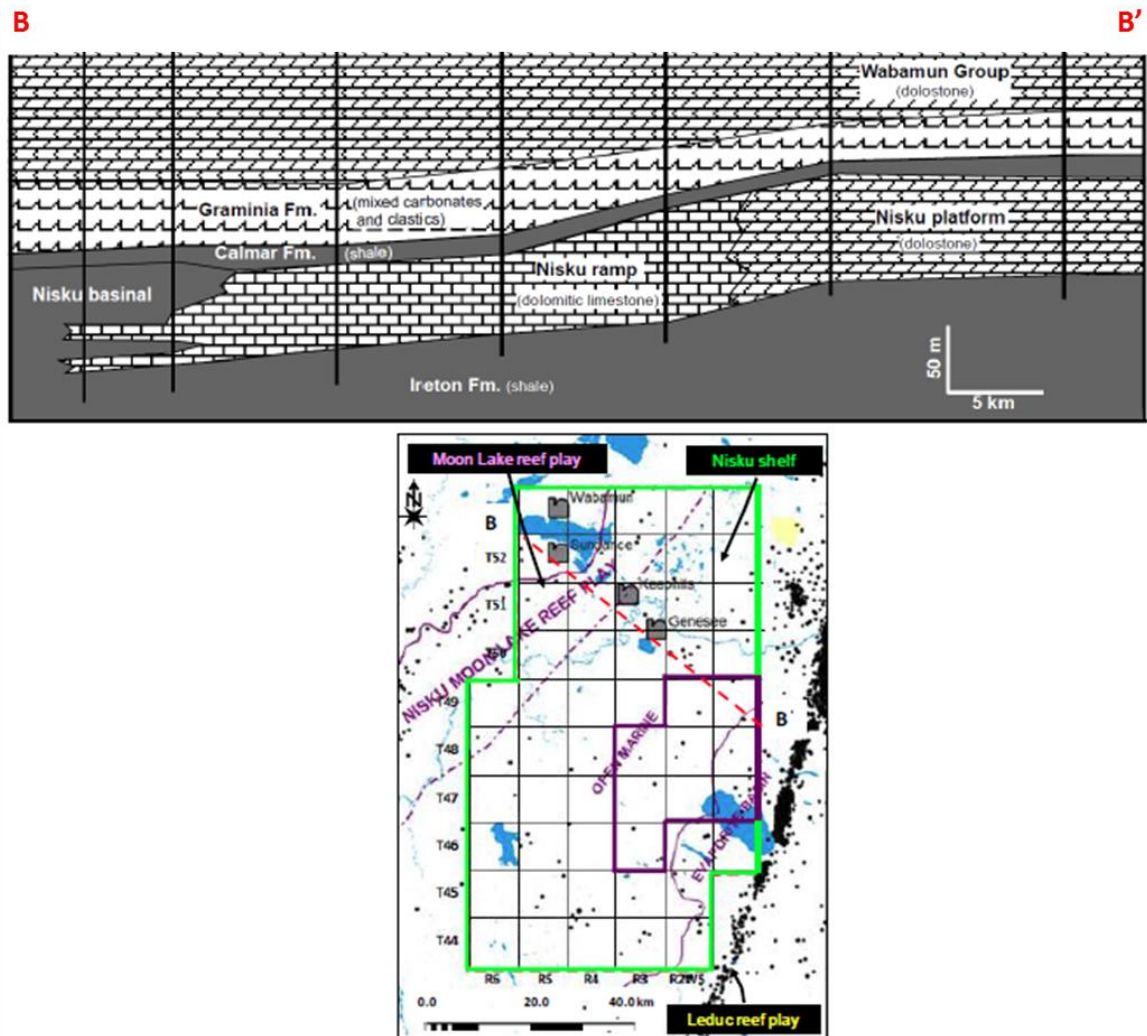


**Figure 3.2: Cross-section across the WASP study area with a northwest-southeast direction showing some of the lithofacies of the Nisku Formation. The dashed line (B-B') in the bottom map indicates the location of the section (modified from Alshuhail, 2011).**

|           |               |                       |                 |   |  |                                 |                                 |
|-----------|---------------|-----------------------|-----------------|---|--|---------------------------------|---------------------------------|
| Paleozoic | Mississippian | Tour.                 | Rundle Group    | Banff Fm.<br>Exshaw Fm.   | ~1560 m  | Siltstone<br>Shale              |                                 |
|           |               |                       | Devonian        | Framenian   | Wabamun Group  | Big Valley Fm.<br>Stettler Fm.  | ~1700 m                         |
|           | Frasnian      | Winterburn Group      |                 |   | Graminia Fm.<br>Blue Ridge Fm.<br>Calmar Fm.<br><b>Nisku Formation</b> | ~1830 m                         | Dolostone<br>Dolostone<br>Shale |
|           |               | Woodbend Group        |                 | Ireton Fm.<br>Leduc Fm.<br>Duvernay Fm.<br>Cooking Lake Fm.       | ~2140 m  | Limestone<br>Shale<br>Limestone |                                 |
|           | Givetian      | Beaverhill Lake Group |                 | Waterways Fm.<br>Slave Point Fm.<br>Fort Vermillion Fm.           | ~2340 m  | Shale<br>Limestone<br>Dolostone |                                 |
|           |               | Eif.                  | Elk Point Group | Watt Mountain Fm.<br>Muskeg Fm.<br>Keg River Fm.<br>Chinchaga Fm. | ~2505 m  | Shale<br>Limestone              |                                 |
|           | Cambrian      |                       |                 |   |  |                                 | Limestone<br>Shale<br>Shale     |
|           |               |                       |                 |   |  |                                 | Shale<br>Shale<br>Sandstone     |
|           |               | PreCambrian           |                 |   |  |                                 |                                 |

**Figure 3.3: Project Pioneer stratigraphic column in the Wabamun Lake area. The target aquifer is indicated by the red rectangle (after Project Pioneer, 2013: [http://www.transalta.com/sites/default/files/Project%20Pioneer\\_Final%20Report\\_Executive%20Summary\\_2013.pdf](http://www.transalta.com/sites/default/files/Project%20Pioneer_Final%20Report_Executive%20Summary_2013.pdf)).**

The area of interest lies along the middle and eastern regions of Nisku shelf (Figure 3.2). In addition to its favourable aquifer properties, such as porosity and permeability, this part of the Nisku Formation has no hydrocarbon potential (Michael et al., 2008).

### 3.2 2D Seismic Data: Highvale and Violet Grove

#### 3.2.1 Project Pioneer Data

The seismic data for this project was provided by CNRL and TransAlta Corporation (TransAlta) and consists of two 2D seismic lines of 17.38 km and 12.91 km,

respectively. The raw gathers and processed stacks were available for this study. Table 3.1 summarizes the main parameters of both lines. The well log information for this study was provided by Schlumberger. Figure 3.4 displays the complete set of logs from Well 8-17. This well was drilled through the target formation down to a depth of 1900 m. Figure 3.5 shows the Highvale stacked section previously processed by C&C System with the location of the Well 8-17.

**Table 3.1: 2D seismic lines main parameters**

| PARAMETERS         | HIGHVALE             | VIOLET GROVE |
|--------------------|----------------------|--------------|
| Source type        | Dynamite (1 kg/18 m) | Vibroseis    |
| Source interval    | 80 m                 | 132 m        |
| Receiver interval  | 20 m                 | 33 m         |
| Sample rate        | 2 ms                 | 2 ms         |
| Record length      | 3 sec.               | 3 sec.       |
| Number of channels | 201                  | 96           |
| Lines length       | 17.38 km             | 12.91 km     |

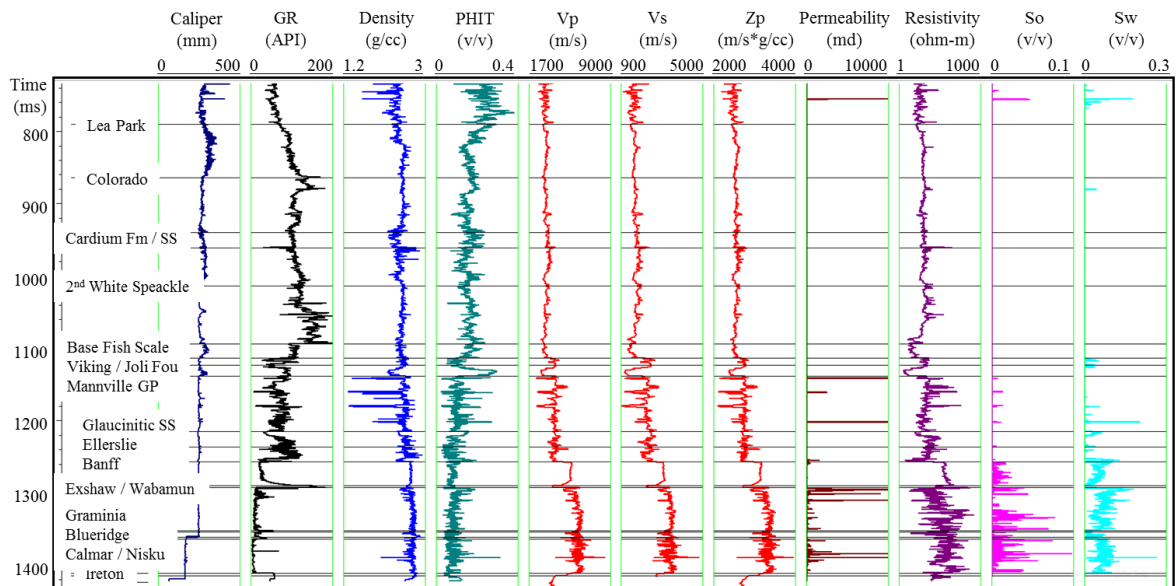


**Figure 3.4: Well 8-17 with its complete logs suite recorded through the target formation down to a depth of 1900 m.**

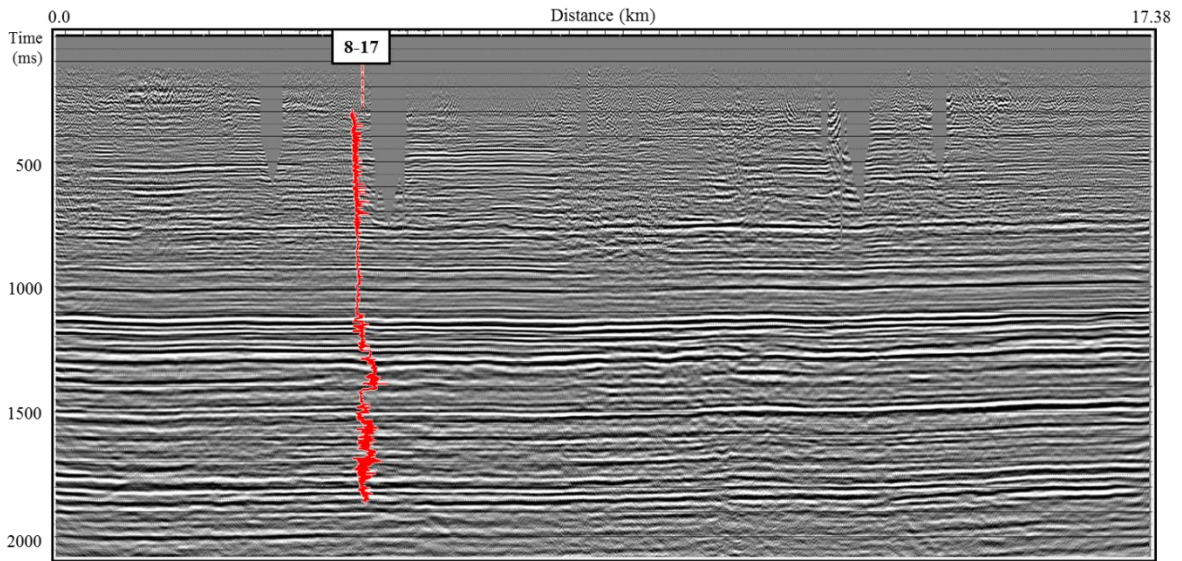
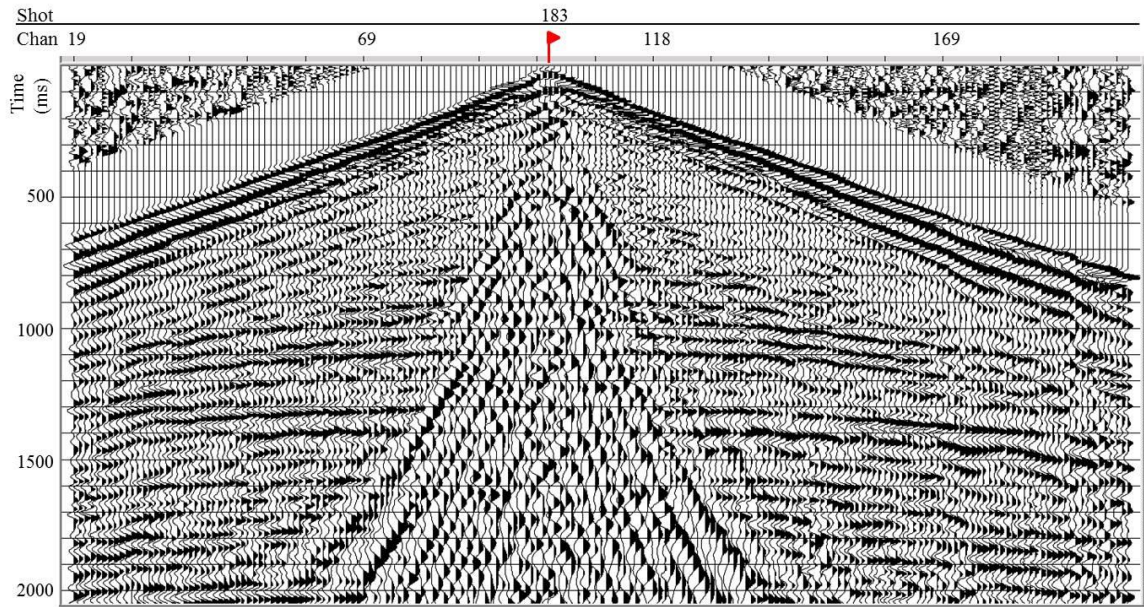


**Figure 3.5: Highvale stacked section with Well 8-17.**

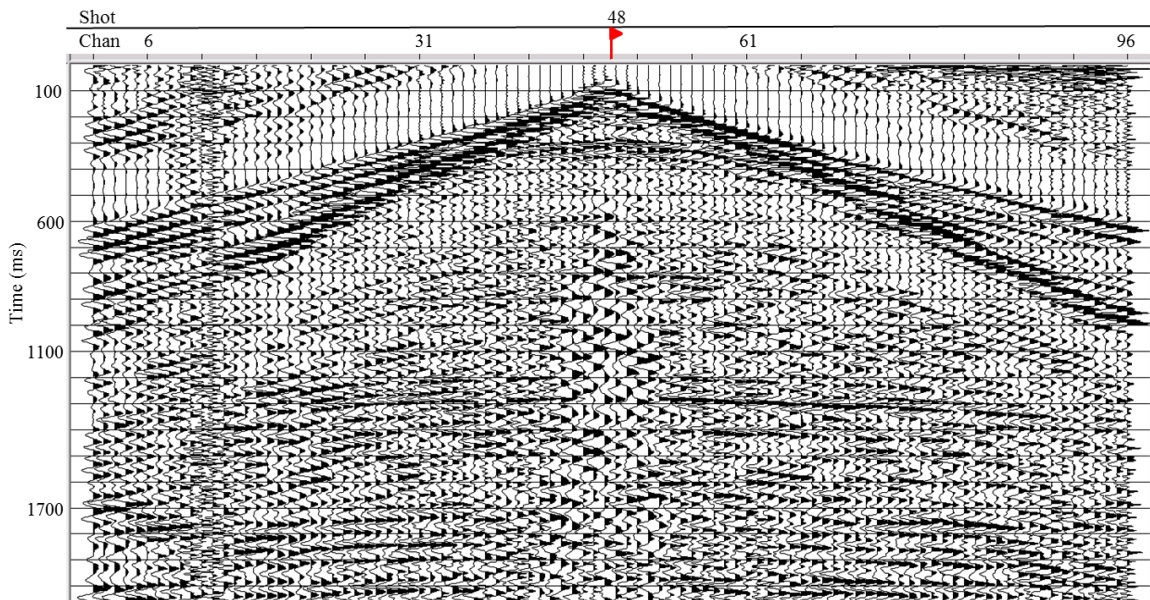
### 3.2.2 Survey Data

Two 2D seismic lines were used in this study. The first line, identified as Highvale, has an east-west trend located in the township/range 51-3W5. The line was acquired with 1 kg of dynamite with a source interval of 80 m and a receiver interval of 20 m. The total number of shots was 235 with a maximum number of 200 channels per shot. The array was split-spread with a maximum offset of 2000 m. The second line or Violet Grove has also an east-west trend located ~50 km southwest from the Highvale line. The line was acquired with vibroseis as the source with a source spacing of 132 m and receiver interval of 33 m. The total number of shots was 107 with a maximum number of 96 channels per shot. The array was split-spread with a maximum offset of 1700 m. 10 Hz Mark Products geophones (OYO-30CT) and ARAM 24 instrument were used. The recorded data has a length of 3 s with a 2 ms sample rate. Figure 3.6 (a) shows

shot 183 from Highvale line where some reflections and ground-roll noise can be observed. In Figure 3.6 (b) shot 48 from Violet Grove line is displayed.



a)



b)

**Figure 3.6: a) shot 183 from the Highvale 2D seismic line, and b) shot 48 from the Violet Grove 2D seismic line. AGC has been applied.**

### 3.2.3 2D Seismic Processing

The seismic data consists of raw gathers that were processed with the software ProMAX with the guidance of Helen Isaac and David Henley. Table 3.2 illustrates the processing flow applied to the seismic data. The processing was focused on imaging the main reflectors, including the Nisku Formation, without compromising the low frequency character present on the seismic data. Especial attention was paid to noise attenuation processes which appear to be the greatest factor in attaining low frequency signal (Isaac, 2012). The processing flow will be explained using the Highvale line as a reference.

**Table 3.2: Processing flow applied to the seismic lines Highvale and Violet Grove**

| General Processing Flow                     |
|---|
| Geometry definition                         |
| First break picking                         |
| Elevation and refraction statics correction |
| Amplitude recovery                          |
| Noise attenuation                           |
| Deconvolution                               |
| Velocity analysis and NMO Correction        |
| CDP stack and residual statics              |
| Post-stack Time Migration                   |

#### 3.2.3.1 Geometry Definition:

The first step, after loading the seismic data into ProMAX, was to correctly define the geometry into the database. ProMAX uses the database to sort the traces and further perform the processing (Isaac, pers.comm). The trace header usually has the field file identification number (FFID) and channel number. The FFID was related to the field shot station number and the channel number to the field recording station number.

### 3.2.3.2 First Break Picking:

The first break is the first recorded signal generated by the seismic source. First breaks are normally used for determining a near surface statics model (Promax user guide, 1997). ProMAX has the automatic tool “First Break Picking” which searches for the first breaks within an offset-dependent time gate. A single time gate is usually enough unless the velocity of the near-surface refractors changes significantly in far offsets so a new window would have to be defined (Isaac, pers.comm). Figure 3.7 shows the Highvale line first break time window on shot 104 and an example of shot 173 where the trough was the chosen point to pick.

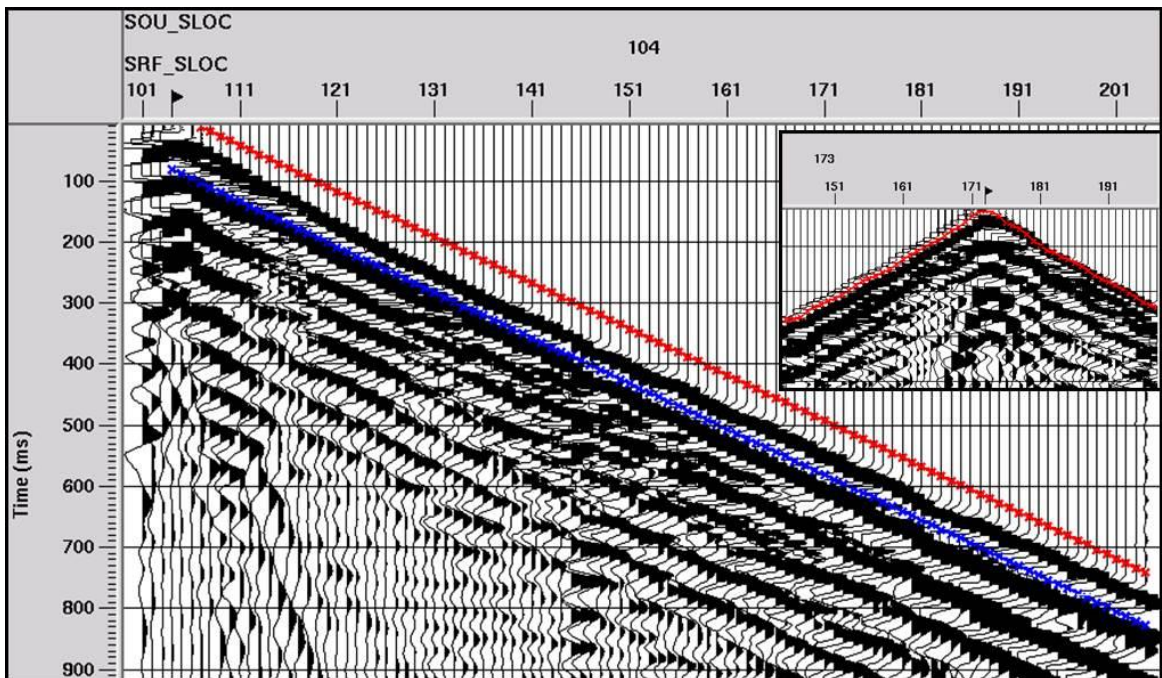


**Figure 3.7: Highvale line first break time gate on shot 104 and an example of the automated picked trough on shot 173.**

### 3.2.3.3 Elevation and Refraction Statics Correction:

Statics corrections are applied to seismic data to compensate for the effects of variations in elevation, weathering thickness and velocity, or reference to a datum (Promax user guide, 1997). Elevation statics correct the source and receiver elevations to a floating (NMO) datum (Isaac, pers.comm) by using the tool “Apply Elevation Statics”. This datum is where the velocity analysis and CDP stack are performed and is a smooth function of the elevation profile. The selected reference datum was 865 m and the replacement velocity was 2700 m/s for both lines.

“First Break Statics” compares the average first break times of source and receivers with their neighbors to compute short period statics (Promax user guide, 1997). Figure 3.8 shows the effect of applying the statics correction to Highvale line shot 104.

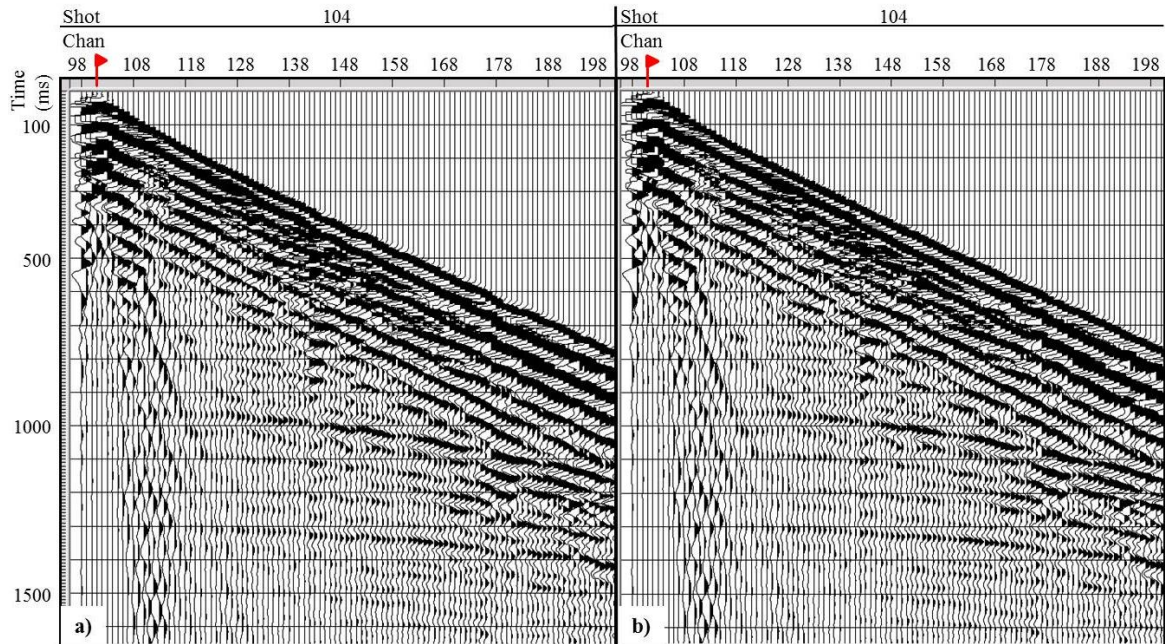


**Figure 3.8: Highvale line shot 104 a) before and b) after statics correction**

### 3.2.3.4 Amplitude Recovery:

In this step the objective is compensate for the natural loss of signal due to geometric spreading and transmission losses (Isaac, pers.comm). The gain correction is performed by applying an amplitude adjustment in the form of time raised to a power correction:

$$g(t) = t^{POWER} \quad (3.1)$$

where POWER is the time-power constant and was set as 2 . The correction was applied using the ProMAX process “True Amplitude Recovery” (Figure 3.9).

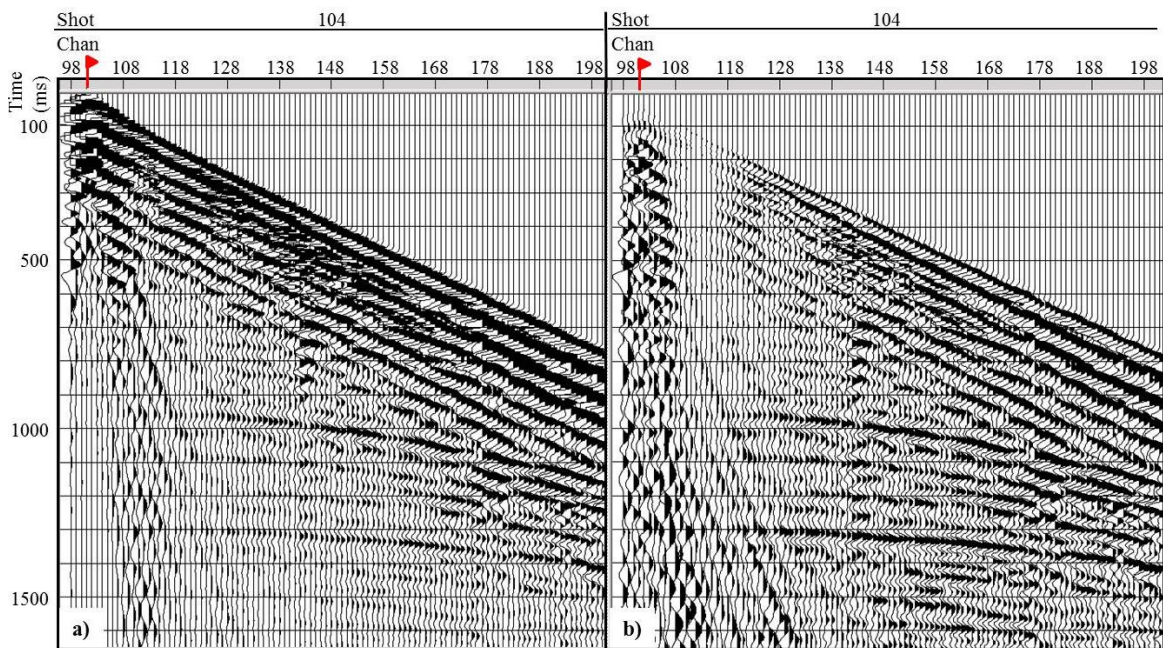


**Figure 3.9: Highvale line shot 104 a) before and b) after amplitude recovery compensation.**

### 3.2.3.5 Noise Attenuation:

Noise present in the seismic data varies depending on the condition of the survey and can be shot generated (surface waves), externally generated (powerline interference)

or receiver generated (bad coupling, noise burst). The shot gathers shown in Figure 3.6 have strong noise that obscures the reflections and is characterized by low frequency and low group velocity. Two noise attenuation techniques were applied separately in this project: Surface Wave Noise Attenuation and Radial Trace Filter. Using a conventional approach the former method attempts to attenuate surface-wave noise given the surface velocity and the frequency cut-off by forming low-frequency arrays. It transforms the data from the time-space domain to the frequency-space domain, where frequency components higher than the cut-off frequency remain unchanged (Promax user guide, 1997). A more recent approach separates coherent noise or ground roll from reflections on seismic trace gathers (Claerbout, 1983) by applying the process known as “Radial Trace Filter”. This technique was developed by David Henley (2011). The technique attempts to isolate the coherent noise from the reflection signal based on the separation in apparent velocity, source position and frequency content in the R-T domain (Henley, 2011). Coherent noise is characterized by linear trajectories that can be attenuated on the basis of its apparent velocity in the X-T domain; while in the R-T domain, source generated linear noises are mapped into compact group of radial traces with significantly lower frequency content (Henley, 2011). The events aligned with these parameters will be subtracted in the X-T domain (Henley, 2003). R-T filter is applied iteratively based on two approaches: first applying a general fan filter to attenuate multiple source-generated noises; and second, by applying a dip filter with a narrow radial trace fan to attenuates residual constant velocity noises (Henley, 2011).

In the case of applying surface wave noise attenuation, four successive filters were applied to the Highvale line data to attenuates the noise (100, 400, 500 and 600 m/s)

with a frequency cut-off of 15 Hz. In the case of applying the radial trace filter one fan filter (-3000 m/s to 3000 m/s) and eight successive dip filters (+/-2400, +/-1500, +/-600 and +/-300 m/s) were applied to remove the ground roll. All the filters were designed with the same low frequency cut-off (5-9 Hz). After running the radial filter a band pass Ormsby filter of 3-6-55-70 Hz was applied for better imaging. Figure 3.10 shows the comparison between the surface wave noise attenuation and the radial filter outputs. An evident reduction of the coherent noise and enhancement of the reflections is appreciated with respect to the data on Figure 3.9. Radial filter succeeds in attenuating first arrivals and allows a better separation between noise and reflections while keeping the low frequency signal unaltered.

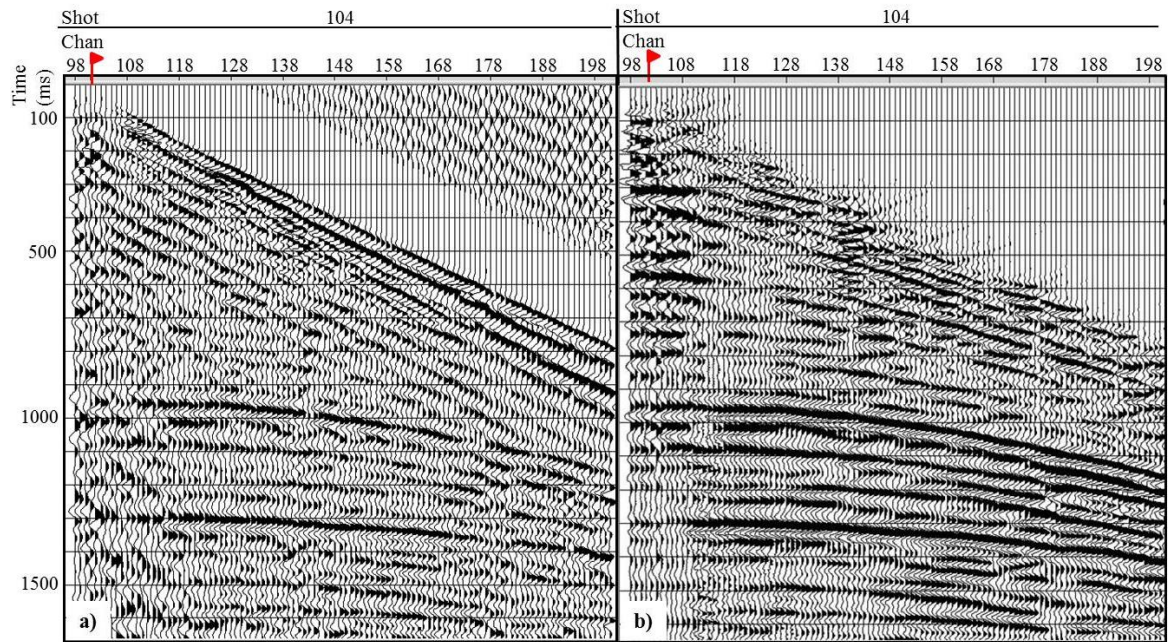


**Figure 3.10: Shot 104 of the Highvale line a) after surface wave attenuation and b) after radial trace filtering.**

### 3.2.3.6 Deconvolution:

Deconvolution is the process that aims to remove the seismic wavelet from the seismic trace and, therefore, improves the temporal resolution (Yilmaz, 2001). It can attenuate multiples and balance the spectrum (Isaac, pers.comm). There are several deconvolution methods (spiking, predictive, etc.) which assume, among other things, that the wavelet is invariant in time where the effects of attenuation and frequency and amplitude variation are not taken into account (Margrave et al., 2002). This stationary assumption of the seismic wavelet motivates the development of an extension of seismic deconvolution to the non-stationary case capable of removing the effects of attenuation in the earth and the source signature (Henley and Margrave, 2008). Margrave et al (2002) developed the Gabor deconvolution which attempts to estimate the time and frequency variant Q function, or attenuation function, for each seismic trace. This function is calculated via the Gabor Transform and then it is included in the deconvolution operator to remove the effects of Q from the seismic trace simultaneously with inverting the source waveform (Henley and Margrave, 2008). Figure 3.11 shows the result of applying Gabor Deconvolution and a bandpass filter of 5-6-55-70 Hz to attenuate boosted high frequency noise on shot 104.

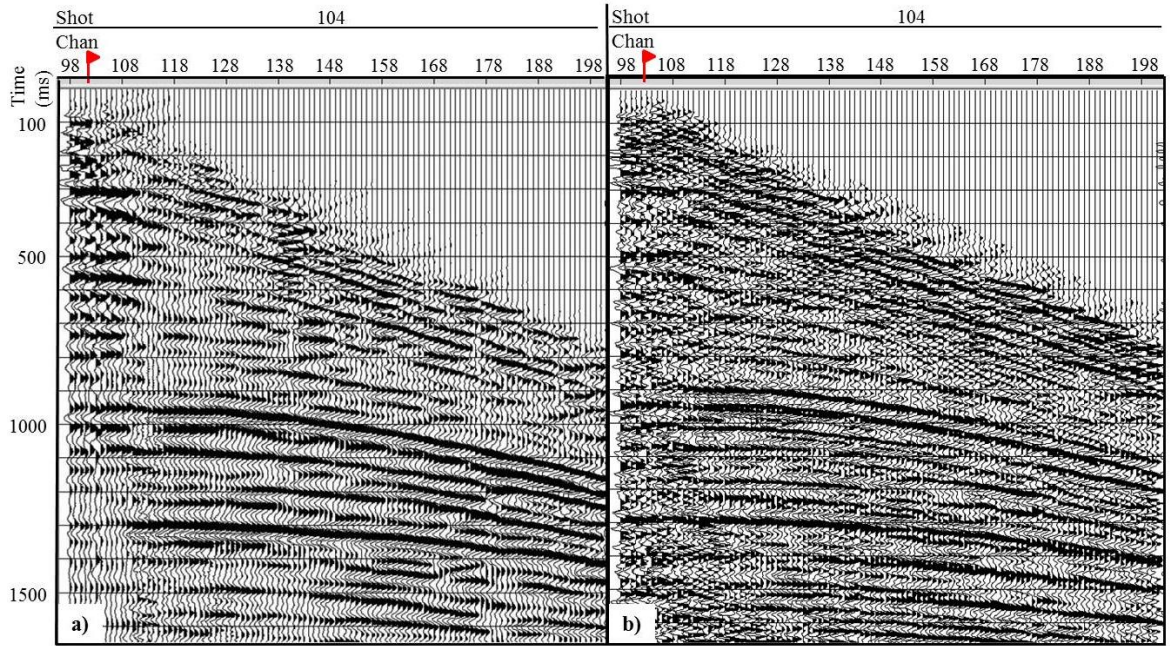


**Figure 3.11: Shot 104 of the Highvale line a) before and b) after applying Gabor Deconvolution and a bandpass filter of 3-6-55-70 Hz.**

### 3.2.3.7 Velocity Analysis and NMO Correction:

The next step in the processing flow is to perform velocity analysis to enable application of normal move out (NMO) correction on CDP gathers (Yilmaz, 2001). Based on the assumption that reflection travel times with offset follow hyperbolic trajectories, the NMO correction is the process to remove the move out effect on travel times by making all traces zero-offset. Reflection travel times are described by the following hyperbolic relationship:

$$t^2 = t_0^2 + \frac{x^2}{V_{RMS}^2} \quad (3.2)$$

where  $t$  is the recorded time at offset  $x$ ,  $t_0$  is time at zero offset and  $V_{RMS}$  is the root mean squared velocity. The NMO correction is given by the difference between  $t - t_0$  and it can be reduced to:

$$\Delta t_{RMS} = t - t_0 = \sqrt{t_0^2 + \frac{x^2}{V_{RMS}^2}} - t_0 \sim \frac{x^2}{2V_{RMS}^2 t_0} \quad (3.3)$$

This approximation is valid for  $x \ll V_{RMS}t_0$ . The RMS velocity is obtained from the velocity analysis which is performed on selected CDP gathers or array of gathers (super gather) by measuring the signal coherency along hyperbolic trajectories ruled by velocity (semblance panel). ProMAX uses the process “Velocity Analysis” to interactively pick the velocity field using the semblance panel and velocity stacks that best corrects CDP gathers. In the Figure 3.12, the semblance panel is shown on the left where the red color indicates maximum semblance; in the next panel is the super gather (group of 7 CDP gathers every 50 CDPs from CDP 205 to CDP 1959 on the Highvale line) as a function of time and offset and it is followed by its stacked section. The final panel includes the stacked traces created after applying move out with the different velocity functions. The final picked velocity is shown with a white line on the semblance panel and with a red line on the velocity functions stack panel. The result from this process can be seen on a 2D velocity model on Figure 3.13 and reflects the geological scenario where generally flat layers are expected.

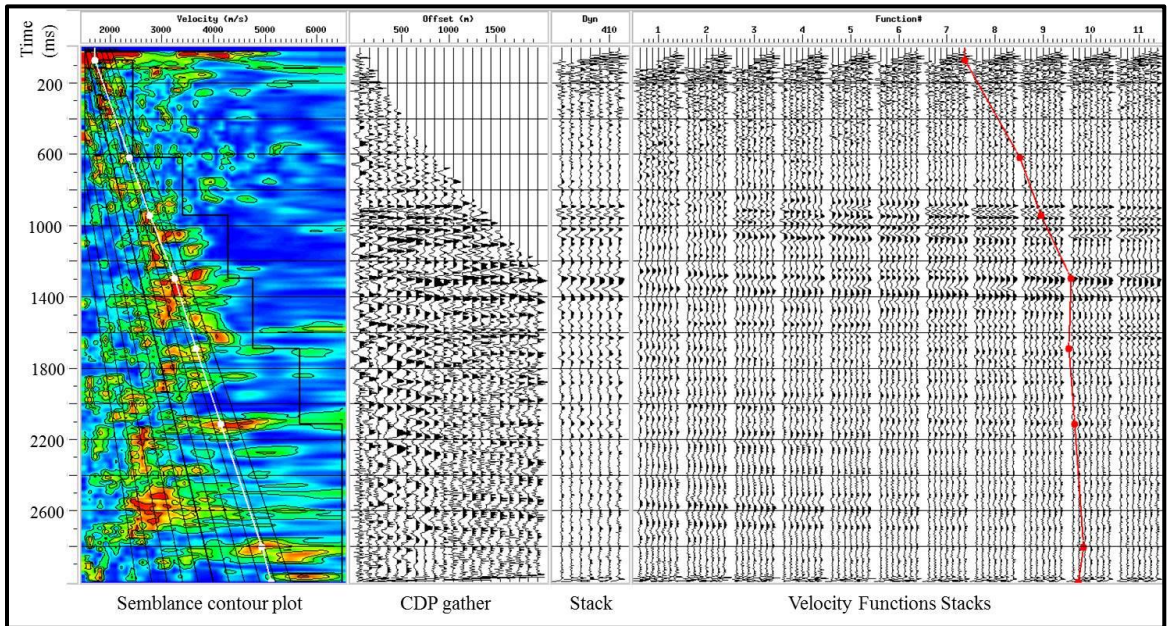


**Figure 3.12: From left to right: semblance panel, CDP gather and velocity functions stack panels from the velocity analysis on the Highvale line. The final velocity function is shown with a white line on the semblance panel and a red line on the stack panel.**

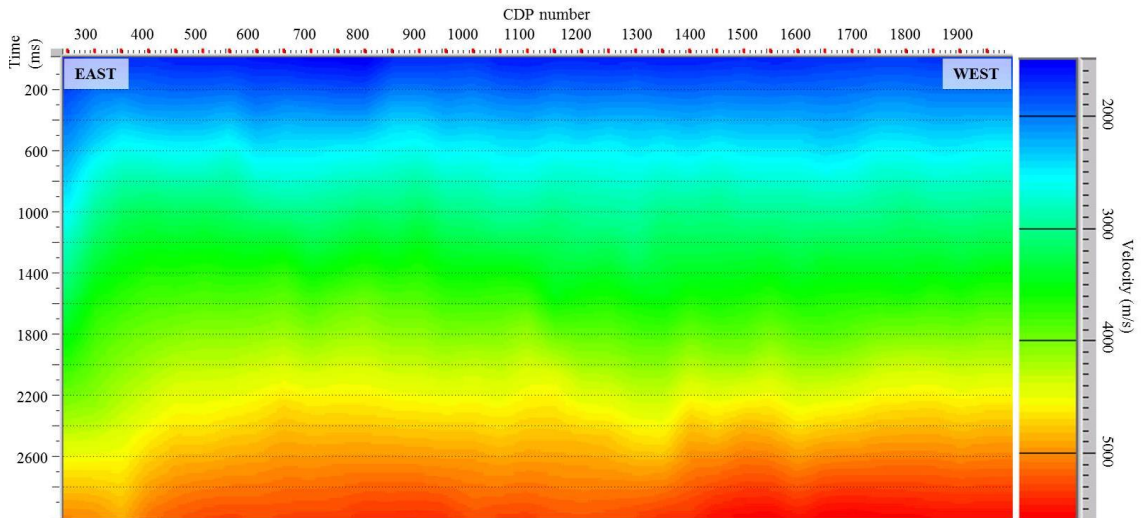


**Figure 3.13: Velocity model obtained from the velocity analysis**

### 3.2.3.8 CDP Stack and Residual Statics:

As mentioned before, the purpose undertaken the velocity analysis was to get a velocity field to apply the NMO correction. This process intends to align the events on CDP gathers using the RMS velocity. All traces are then stacked to create a seismic section.

Residual statics attempt to align a target event in MNO corrected CDP gathers by applying static shifts (Isaac, pers.comm). “2D/3D Maximum Power Autoestatics” is the ProMAX tool for applying this surface-consistent process based on the cross-correlation of a pilot trace, formed from summing several traces in a target window along the autoestatic horizon, with other traces with the same source and receiver and the difference in time defines the shift to apply the correction. Figure 3.14 shows the section after applying NMO correction, residual statics and a time variant band pass filter. Strong reflections are easily identified in the middle of the section. As discussed in the geology overview (3.1.2) and showed in Figure 3.13 the geology of the area presents flat layers with no major structures. After applying the NMO correction, a depression can be observed in the middle of the section possibly related with a shallow channel caused by an old meander of the North Saskatchewan River. No velocity or statics anomalies were observed during the processing of this dataset. This depression is not present in the previous processing performed by C&C.

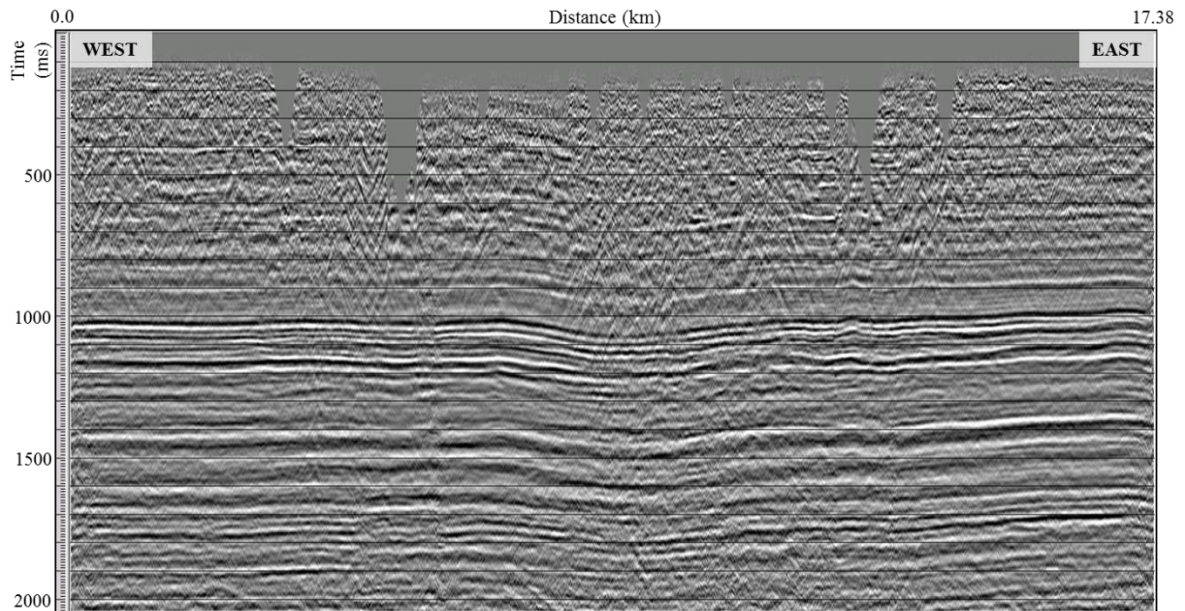


**Figure 3.14: Highvale CDP stacked section. Clear reflections are easily identified across the section.**

### 3.2.3.9 Post-stack Time Migration:

Post-stack time migration attempts to move the reflections to their correct subsurface location. Several post-stack migration techniques have arisen depending on geological complexity and the characteristics of the seismic data. In this case Implicit Finite Difference Time Migration was the chosen technique which performs a post-stack time migration using a Finite Difference algorithm capable of imaging steep dips (Promax user guide, 1997). The Highvale migrated sections using the two processing flows are shown in Figure 3.15 and Figure 3.16, 100% of the interval velocity field was used. Figure 3.15 shows the result of applying conventional processes (surface wave attenuation and spiking deconvolution), while Figure 3.16 shows the result of applying more specialized processes (radial filter and gabor deconvolution). Since the geology character is flat no major changes are seen in comparison with the section in Figure 3.14.

An improvement in continuity and resolution is evident. It is important to mention that after migration an F-X Decon was applied to produce an output section with less random noise than the input data. F-X Decon applies a Fourier transform to each trace of stacked data. It applies a complex Wiener Levinson prediction filter in distance for each frequency in a specified range, and then inverse transforms each resulting frequency trace back to the time domain (Promax user guide, 1997). In this case, 50 traces were used in the horizontal prediction window and the frequency range was set to 5-80 Hz.

Both results are very similar but, as shown in the pre-stack data in Figure 3.10, the radial filter was successful in attenuating noise while keeping more low frequency signal. The events are more continuous in Figure 3.16.

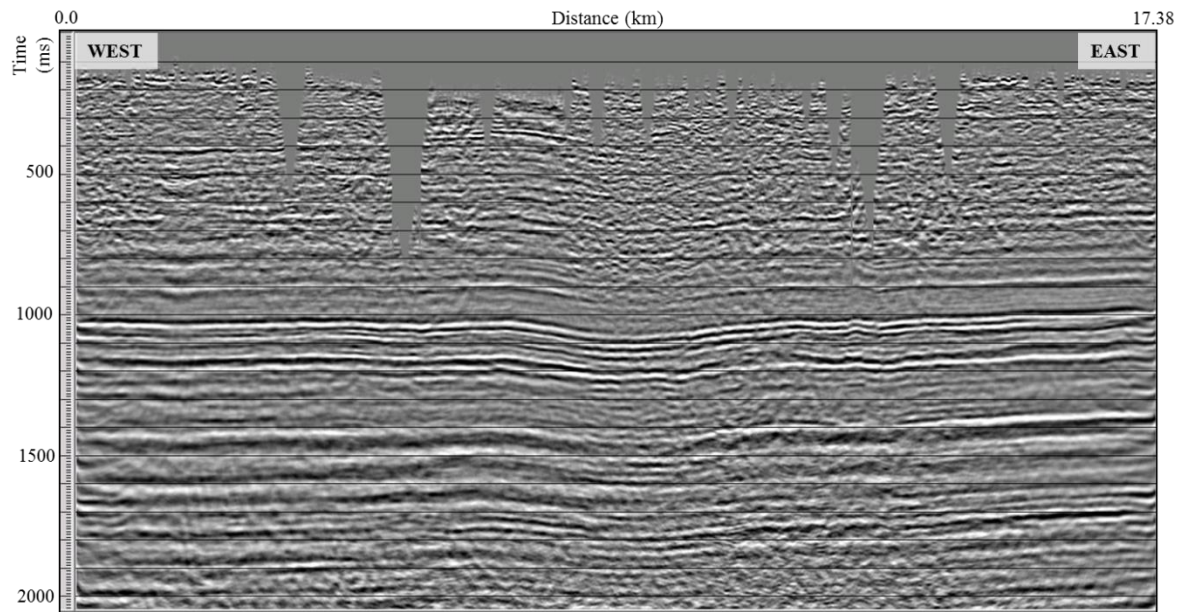


**Figure 3.15: Highvale stack section after applying conventional processes and Implicit Finite Difference Time Migration and F-X Deconvolution. No major changes are observed in terms on the position of the reflectors due to the flat character of the events.**

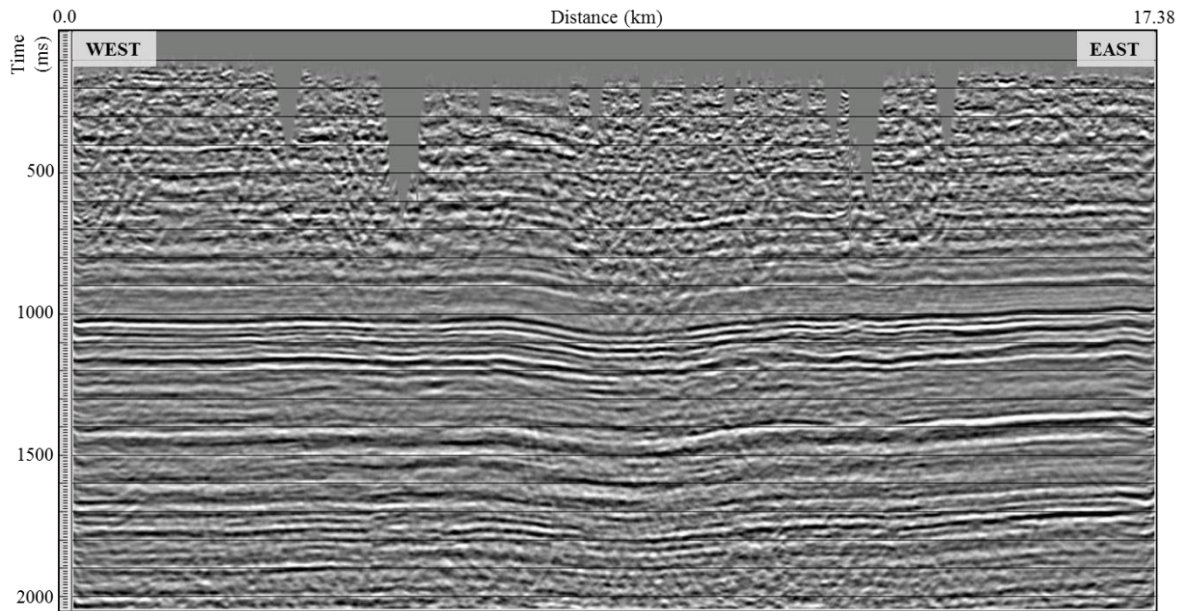


**Figure 3.16: Highvale stack section after applying special processes (Radial Filter and Gabor Deconvolution) and Implicit Finite Difference Time Migration and F-X Deconvolution.**

Figure 3.17 shows the final processing result on the Violet Grove line after applying a conventional processing flow. Similar quality to the Highvale line is observed.

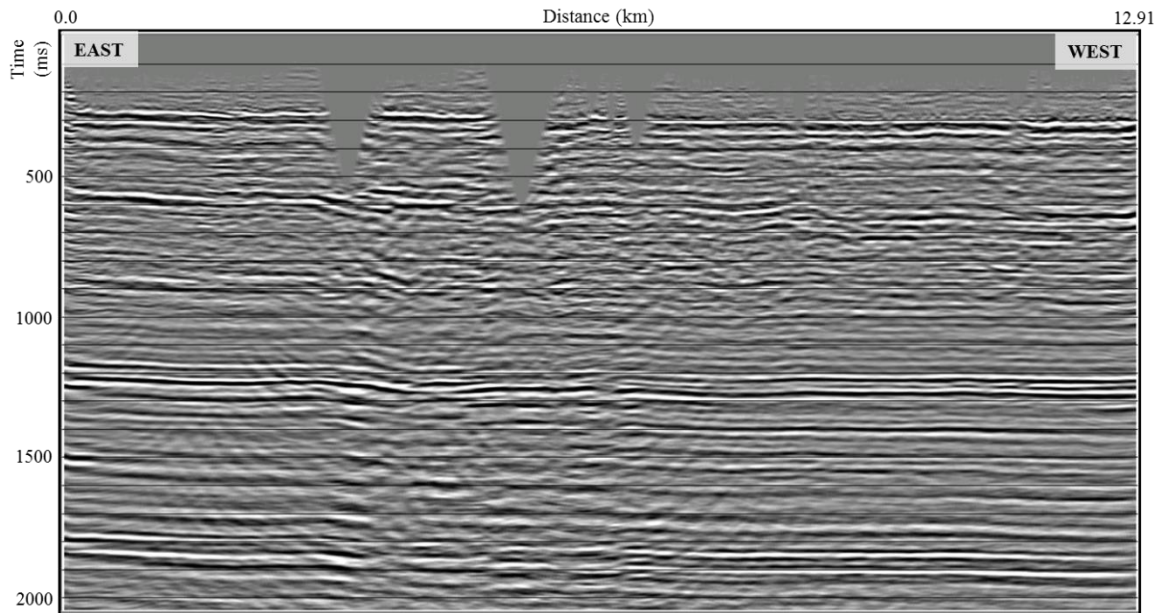


**Figure 3.17: Violet Grove stack section after applying conventional processes and Implicit Finite Difference Time Migration and F-X Deconvolution.**

### 3.3 Highvale Seismic Inversion

#### 3.3.1 Introduction:

The purpose of this section is to evaluate the seismic response of the Nisku Formation by studying its amplitude variation in terms of impedance changes with the surrounding formations. As we discussed in Chapter 1, inversion is the method to estimate the impedance component of the seismic trace and this is highly dependent on the inversion initial model. An inversion comparison has done with the seismic data processed by the company C&C Systems Limited (C&C) as well as the data processed in this dissertation. This section includes the well-seismic tie process, cross plot analysis and the detailed inversion study performed on both datasets. Highvale line was used for this purpose since there is a well that matches the line (Well 8-17) which was conditioned and studied by Schlumberger for the Project Pioneer.

Figure 3.18 shows a comparison of three different processing results around the well location a) previous processing (C&C); b) current processing with the specialized sequence (radial filter and gabor deconvolution); and c) current processing with a conventional sequence (surface wave attenuation and spiking deconvolution). The frequency content, resolution and continuity vary between the C&C result and the other two results.

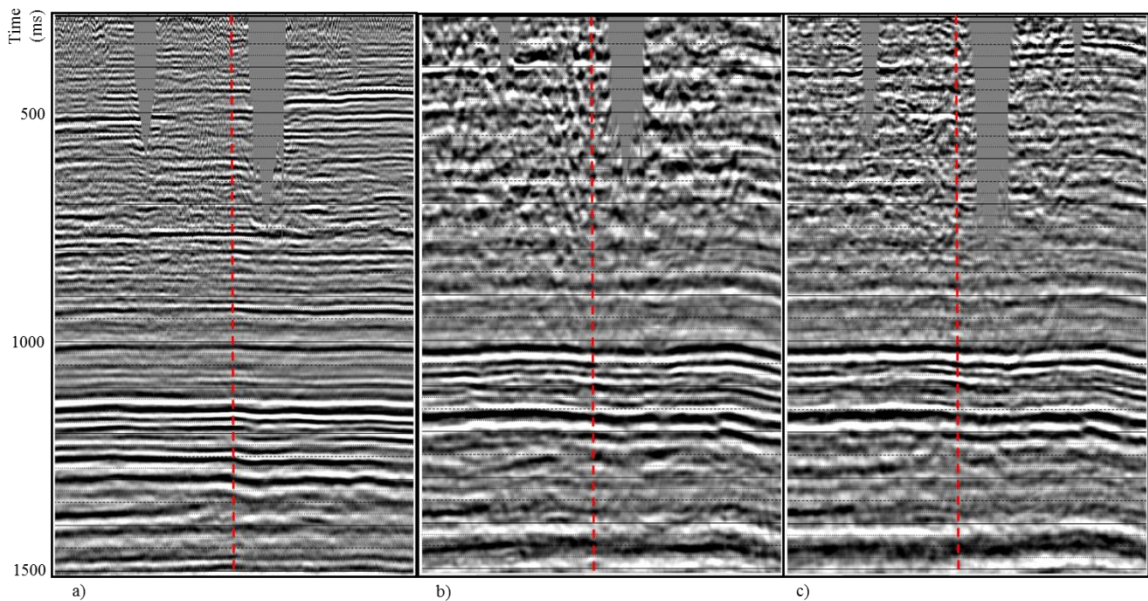


**Figure 3.18: Comparison of processing results: a) previous processing b) current specialized sequence and c) current conventional sequence. Note the difference in frequency content, resolution and continuity of the events depending on the processing applied. The red dotted line shows the location of the Well 8-17.**

The importance of retaining the low frequency component in the seismic data was discussed in Chapter 2. In this case, current processing was focused on keeping this low frequency signal while attaining the noise present in the data (Figure 3.10). In Figure 3.19 the amplitude spectra for each dataset are displayed and were calculated in a window of 700 ms (800 ms to 1500 ms) along the entire section. As can be observed, the low

frequency content includes ~5-9 Hz in cases b) and c), while in case a) the frequency content includes only ~10-14 Hz.

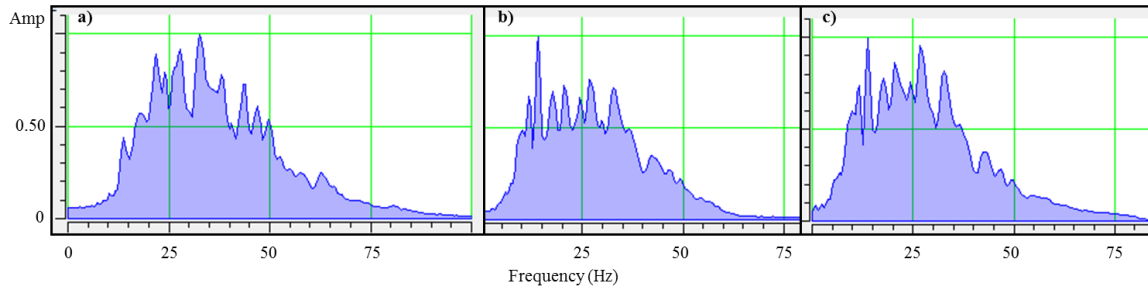


**Figure 3.19: Frequency spectra of the datasets shown in figure 3.17 in a 700 ms window around the target formation. Note the low frequencies include 5-9 Hz in cases b) and c), while in case a) the frequency content includes 10-14 Hz.**

### 3.3.2 Well Log Analysis

The well log information for this study was provided by Schlumberger as discussed at the beginning of this chapter (Figure 3.4). Schlumberger undertook a detailed study with this well including core analysis to analyze the capability of the Nisku Formation to store CO<sub>2</sub> as well as testing the Calmar Formation as a seal to avoid potential leakage of the injected gas. Figure 3.20 shows an image of the core samples from the Nisku and Calmar formations (Carbon Management Canada, 2013: <http://www.cmc-nce.ca/events/gallery/>).



**Figure 3.20: Nisku core sample and Calmar core plug recovered from Well 8-17 during the development of Project Pioneer. Diameter = 1 inch (modified from Carbon Management Canada, 2013: <http://www.cmc-nce.ca/events/gallery/>).**

Table 3.3 summarizes the main properties of the Nisku Formation from analyzing Well 8-17 as well as three others in the Wabamun area (Alshuhail, 2011).

**Table 3.3: Physical properties of the Nisku Formation in the Wabamun Area. The values with an asterisk (\*) were obtained from the Well 8-17.**

|  |  |
|--|--|
| Target Aquifer / Formation               | Nisku                                    |
| Primary Lithology                        | Dolostone                                |
| Reservoir Bearing Fluid                  | Water (brine)                            |
| Other Reservoir Fluid                    | Gas (CH <sub>4</sub> , H <sub>2</sub> S) |
| Reservoir Depth                          | 1793* m                                  |
| Reservoir Thickness                      | 103* m                                   |
| Reservoir Pressure                       | 15 MPa                                   |
| Reservoir Temperature                    | 50.3 C°                                  |
| CO <sub>2</sub> Phase at the Reservoir   | Supercritical                            |
| Gas-Water Ratio                          | 4 (insignificant)                        |
| Average Effective Porosity               | 7.4* %                                   |
| Average Permeability                     | 315* mD                                  |
| Density of Supercritical CO <sub>2</sub> | 653 kg/m <sup>3</sup>                    |

From Table 3.3 it can be observed that the average effective porosity value of the Nisku Formation is 7.4% and the average permeability is 315 mD. In comparison, the average effective porosity of the Calmar Formation is 1.8% and the average permeability is 0.83 mD (Alshuhail, 2011). Importantly the differences in these properties are key for reducing the risk of potential leakage.

From the cross plot analysis performed on Well 8-17 it should be possible to differentiate the Nisku Formation from the overlain formations. Since the Calmar Formation has a thickness of 6 m in this area, it is expected that resolving this formation from Graminia and Blueridge formations will be a challenge. Following the same

analysis completed at Hussar (Section 2.1.3), the vertical resolution for this dataset is approximated 50 m. Figure 3.21 shows a cross plot between P-impedance ( $Z_P$ ) and porosity ( $\phi$ ) with Gamma Ray (GR) in the colour key. The cross plot was done between tops Banff and Ireton (1256 ms to 1411 ms). Note how cleaner lithologies (GR < 10) separates from more shaly lithologies with high values of P-impedance ( $Z_P > \sim 16 \times 10^6$  kg/(s\*m<sup>2</sup>)). The two yellow bars above the Nisku Formation correspond to the Calmar and Graminia formations. In terms of performing an inversion study it would be challenging to resolve these formations.

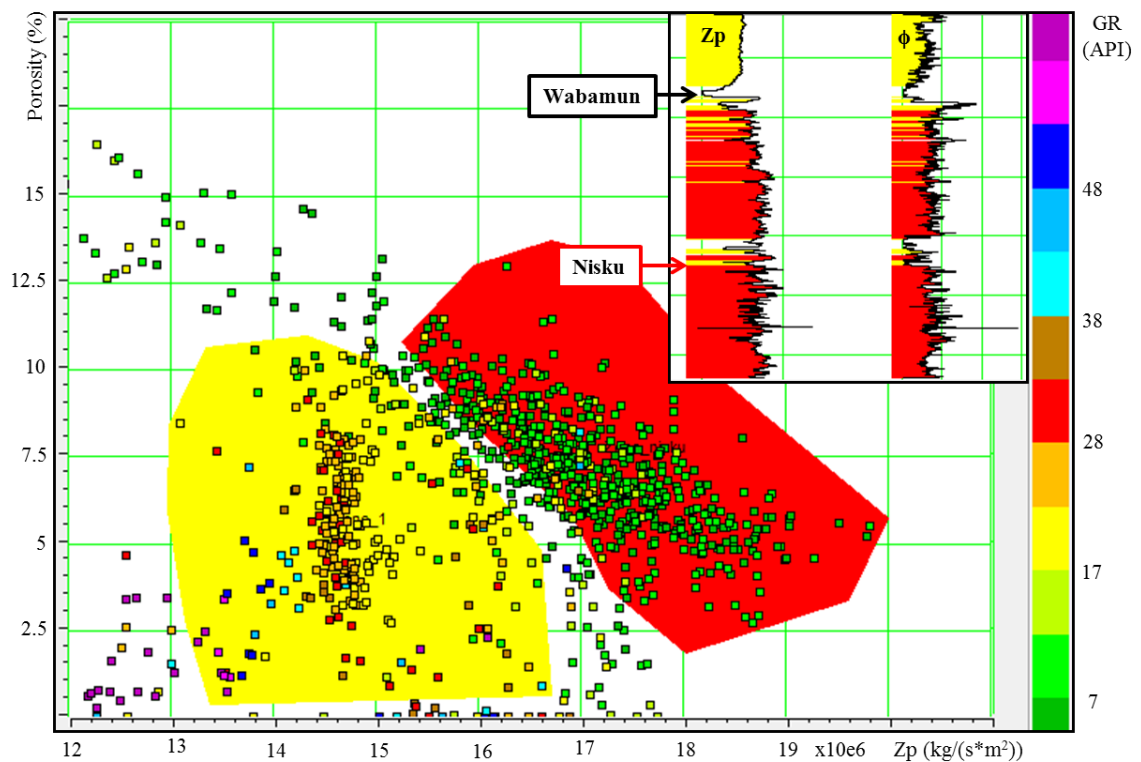


**Figure 3.21: Cross plot between  $Z_P$  and porosity and GR in the colour key. Note how Cleaner lithologies (GR < 10) separates from more shaly lithologies with high values of P-impedance ( $Z_P > \sim 16 \times 10^6$  kg/(s\*m<sup>2</sup>)). The two yellow bars above the Nisku Formation correspond to Calmar and Graminia formations.**

In all the three cases (a, b and c) the seismic-well tie process was performed following the procedure in Chapter 2 (2.1.5). The bottom part of the P-wave log from another well drilled deeper (10-5) was used to help the seismic-well tie process. The wavelet was extracted from the Well 8-17 in a window from 800 ms to 1500 ms (Figure 3.22). The final correlation coefficient in case a) was 0.738 (Figure 3.23).

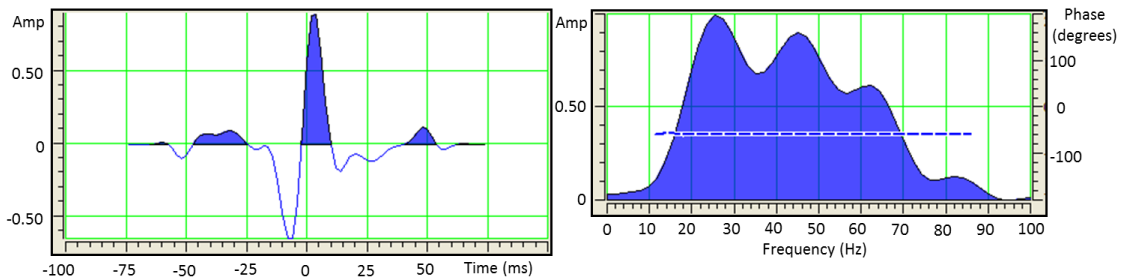


**Figure 3.22: Wavelet extracted from Well 8-17 in case a) with its amplitude spectrum. The dotted line indicates the average phase of the wavelet ( $-56^\circ$ ).**

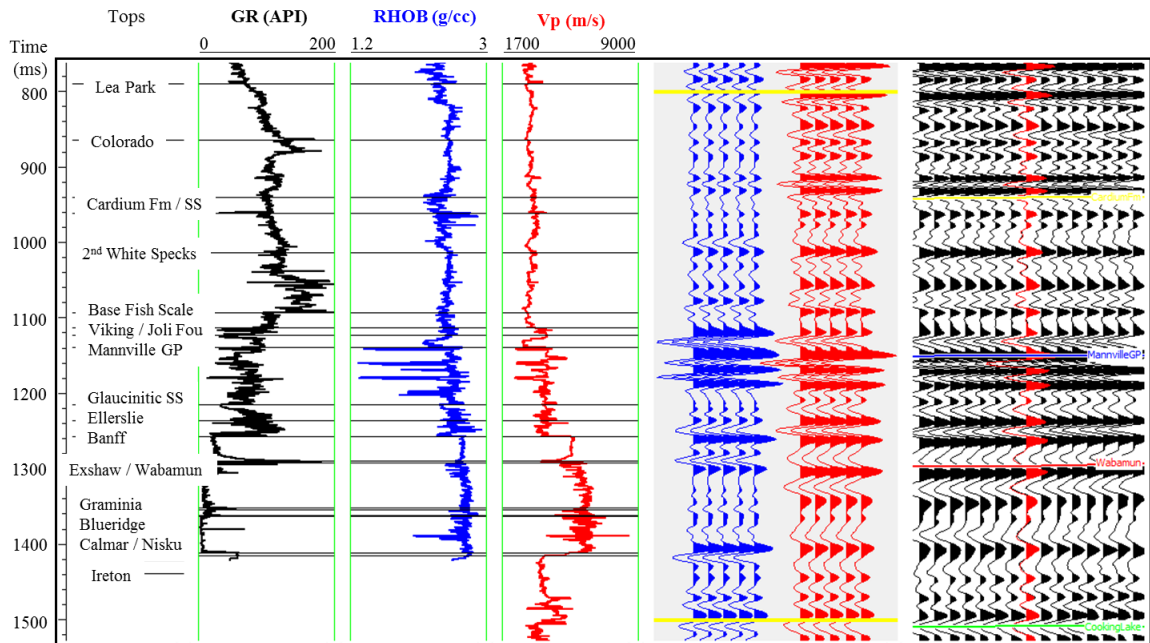


**Figure 3.23: Final tie of Well 8-17 with the C&C dataset (case a). Blue traces represent the synthetic seismogram; red traces represent the extracted trace from the seismic data at the well location, and black traces shows the ten traces around the well location. Yellow bars show the correlation window. Correlation = 74%.**

Figures 3.23, 3.24, 3.25 and 3.26 show the wavelet and seismic-well tie process for cases b) and c) respectively. The correlation coefficient in case b) was 0.623, while in case c) was 0.473.

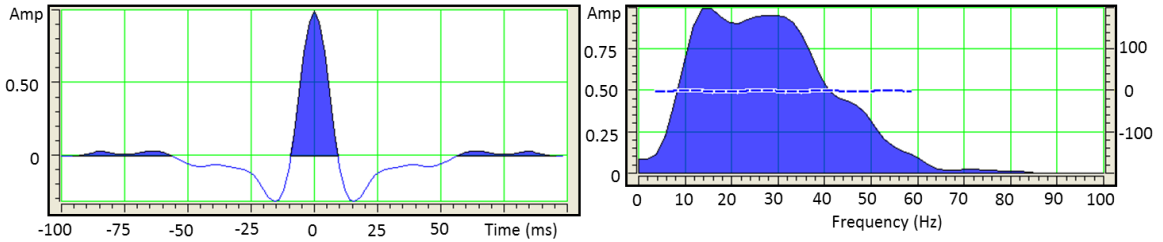


**Figure 3.24: Wavelet extracted from Well 8-17 in case b) with its amplitude spectrum. The dotted line indicates the average phase of the wavelet ( $-7^\circ$ ).**

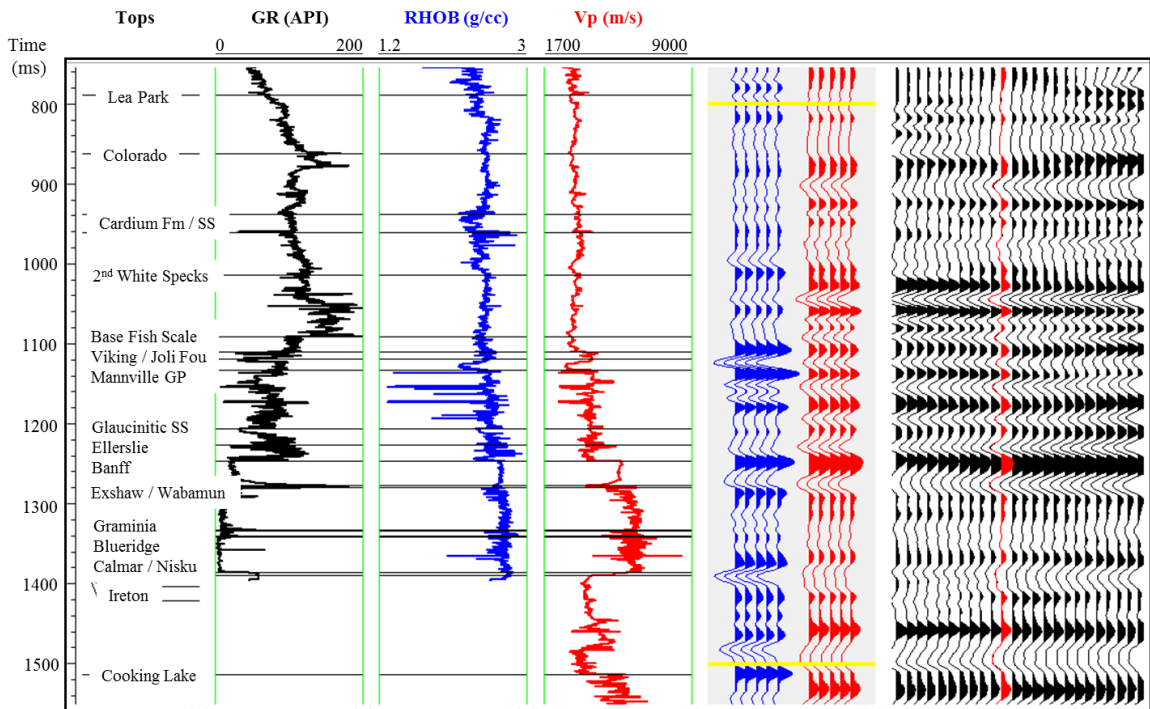


**Figure 3.25: Final tie of Well 8-17 with the case b) dataset. Blue traces represent the synthetic seismogram; red traces represent the extracted trace from the seismic data at the well location, and black traces shows the ten traces around the well location. Yellow bars show the correlation window. Correlation = 62%.**

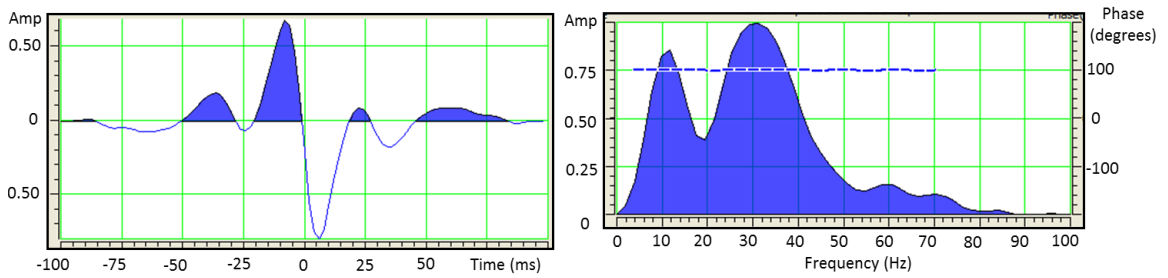


**Figure 3.26: Wavelet extracted from Well 8-17 in case c) with its amplitude spectrum. The dotted line indicates the average phase of the wavelet ( $102^\circ$ ).**

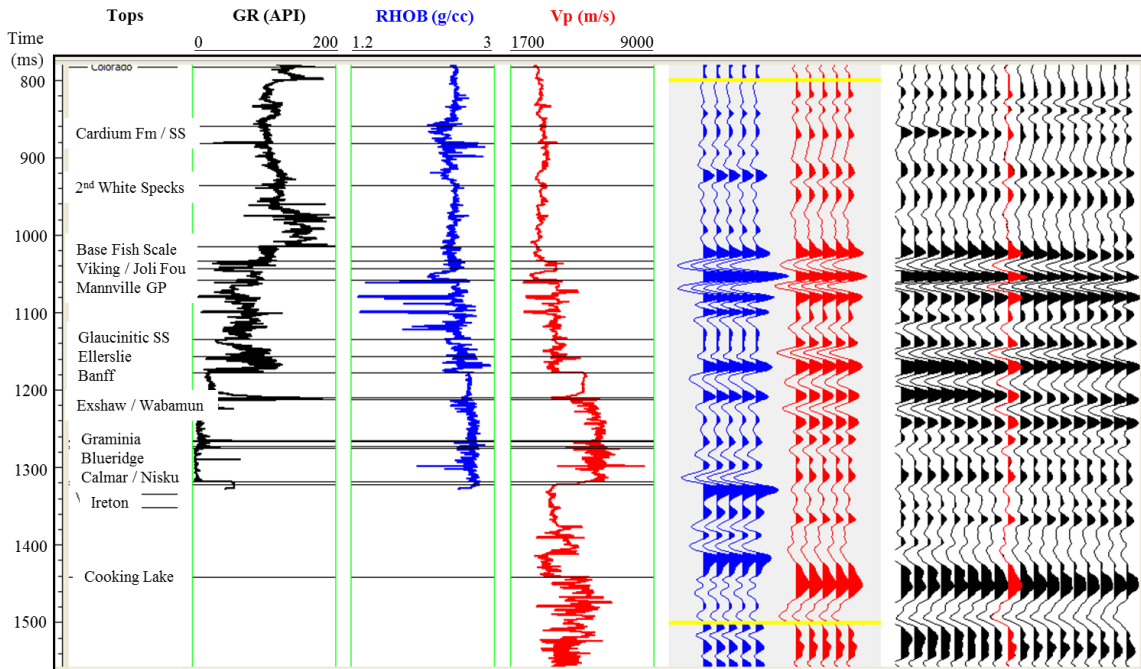


**Figure 3.27: Final tie of Well 8-17 with the case c) dataset. Blue traces represent the synthetic seismogram; red traces represent the extracted trace from the seismic data at the well location, and black traces shows the ten traces around the well location. Yellow bars show the correlation window. Correlation = 47%.**

The seismic-well tie process in case (c) showed a phase shift value different from the previous cases and a low correlation coefficient possibly created by the low frequency noise observed in the amplitude spectrum of the wavelet (Figure 3.26). Referencing back to Section 3.2.3.5 this dataset was processed using a conventional approach in attenuating surface wave noise which is not strong in differentiating signal from noise in the low frequency range. Based on this analysis, it was decided not to perform an inversion study with this dataset.

### *3.3.3 Initial Model for Inversion*

Following the same workflow described in section 2.2.1, the initial background model was created by blocking an impedance log from a well. The P-impedance ( $Z_P$ ) initial model was generated using a P-impedance log calculated with the sonic and density logs from Well 8-17. In case a), a low-pass filter with a high frequency ramp of 8-13 Hz was applied to build the model (Figure 3.28); while in case b), the high frequency ramp was 6-10 Hz (Figure 3.29). P-impedances in the model range from 3.8 to almost 19 kg/(s\*m<sup>2</sup>). The 2D impedance model was generated by interpolating the impedance at the well location using the Second White Speckled Shale horizon as a guide in both cases. As mentioned previously, the dataset from case (c) was not used in the inversion study due to uncertainties in its seismic-well correlation.

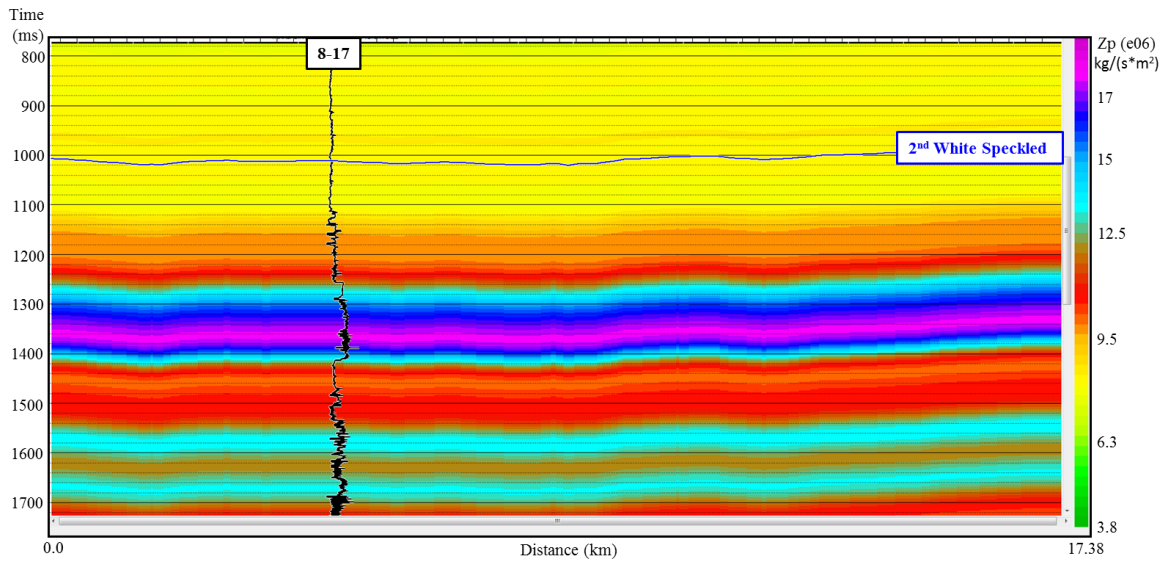


**Figure 3.28: Initial low frequency P-impedance model (0-0-8-13 Hz) using Well 8-17 and the Second White Speckled Shale horizon. The inserted black curve is the  $V_p$  log.**

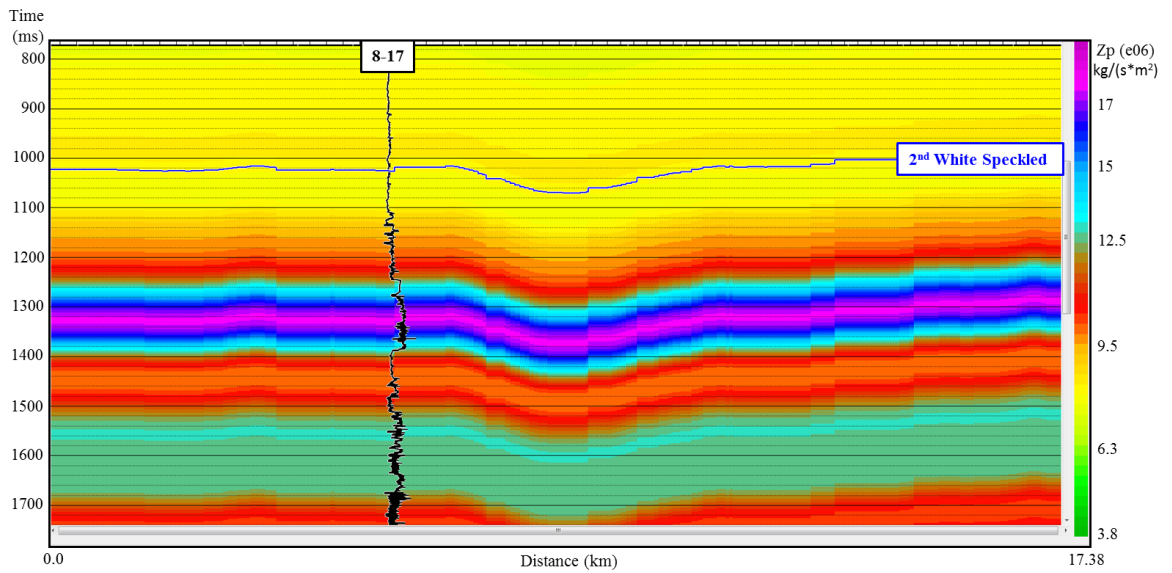


**Figure 3.29: Initial low frequency P-impedance model (0-0-6-10 Hz) using Well 8-17 and the Second White Speckled Shale horizon. The inserted black curve is the  $V_p$  log.**

### 3.3.4 Inversion Analysis

A post-stack inversion analysis was performed initially at the location of Well 8-17 focused on a window from 800 to 1500 ms, to evaluate the efficacy of the inversion by comparing the impedance at the well with the impedance derived from the seismic data. The impedance was inverted from a single trace at the well location and was then convolved with a wavelet to produce a synthetic trace that was compared with the actual seismic trace at that location. The correlation between the synthetic trace (red) and the seismic trace (black) is very good in both cases ((a) and (b)) with high correlations coefficients (over 0.99 for case (a) and over 0.96 for case (b)), (Figure 3.30 and Figure 3.31 respectively). The estimated RMS error between them is 0.09 and 0.26. As mentioned previously, the inversion result is band-limited and fails to reproduce the higher frequency details in the impedance observed in the well logs. To make a fair comparison, well logs were filtered using a high-cut of 60/100 Hz. Within the inverted window the inversion estimates are very close to the actual impedance values; however, in the Wabamun Group the inverted impedance shows the general trend and relative variations indicating higher impedance consistent with its lithology. The RMS error between the target log and the predicted log curves is  $1.4 \times 10^6 \text{ kg/(s} \cdot \text{m}^2)$ , or 5 %.

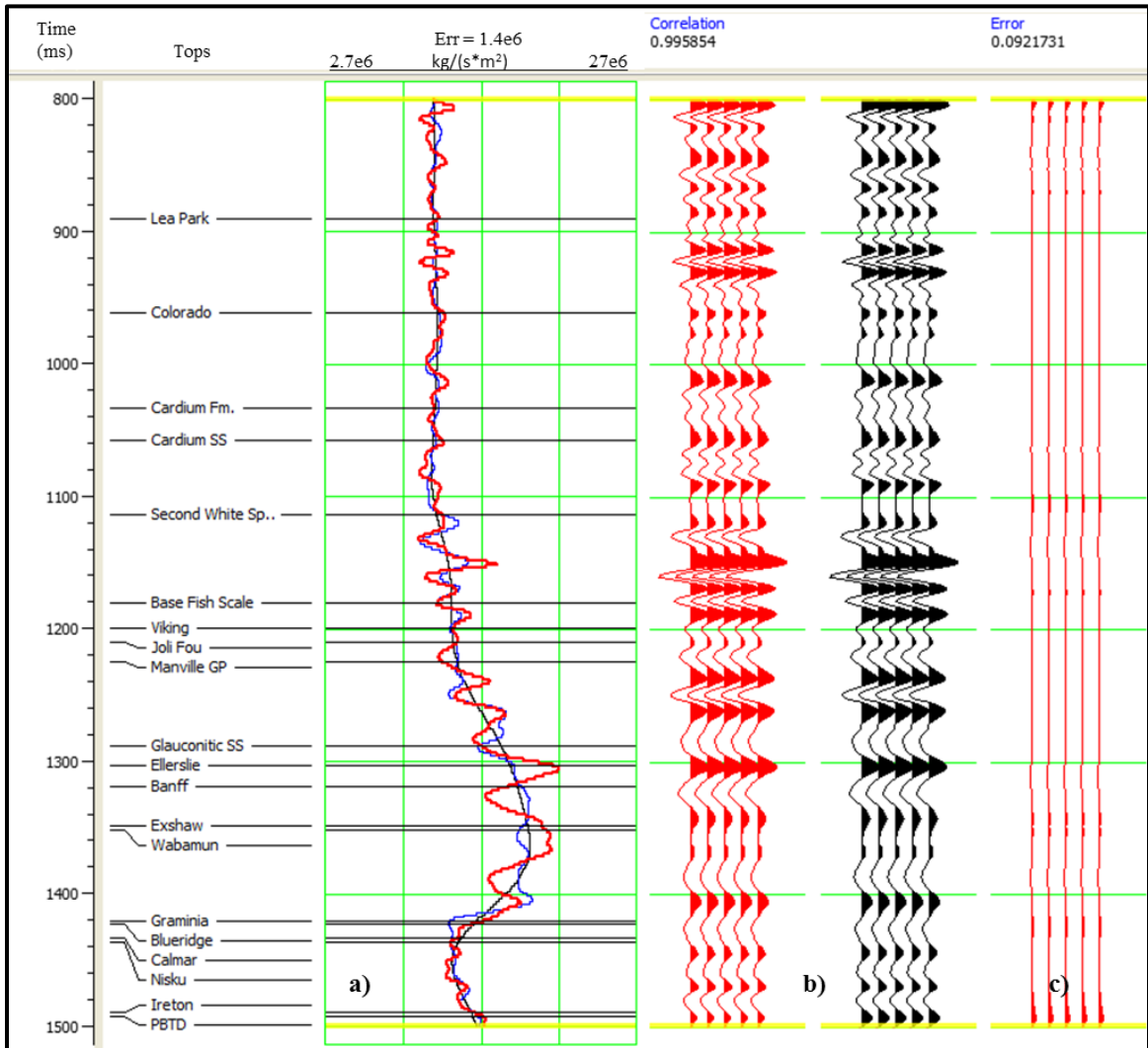


**Figure 3.30: Analysis of the post-stack inversion at Well 8-17 with the initial model cut-off of 0-0-8-13 Hz: a) filtered impedance log (blue), initial model (black), inversion result (red); b) synthetic trace from inversion (red) and extracted trace from the seismic (black), and c) RMS error between synthetic trace and seismic trace.**

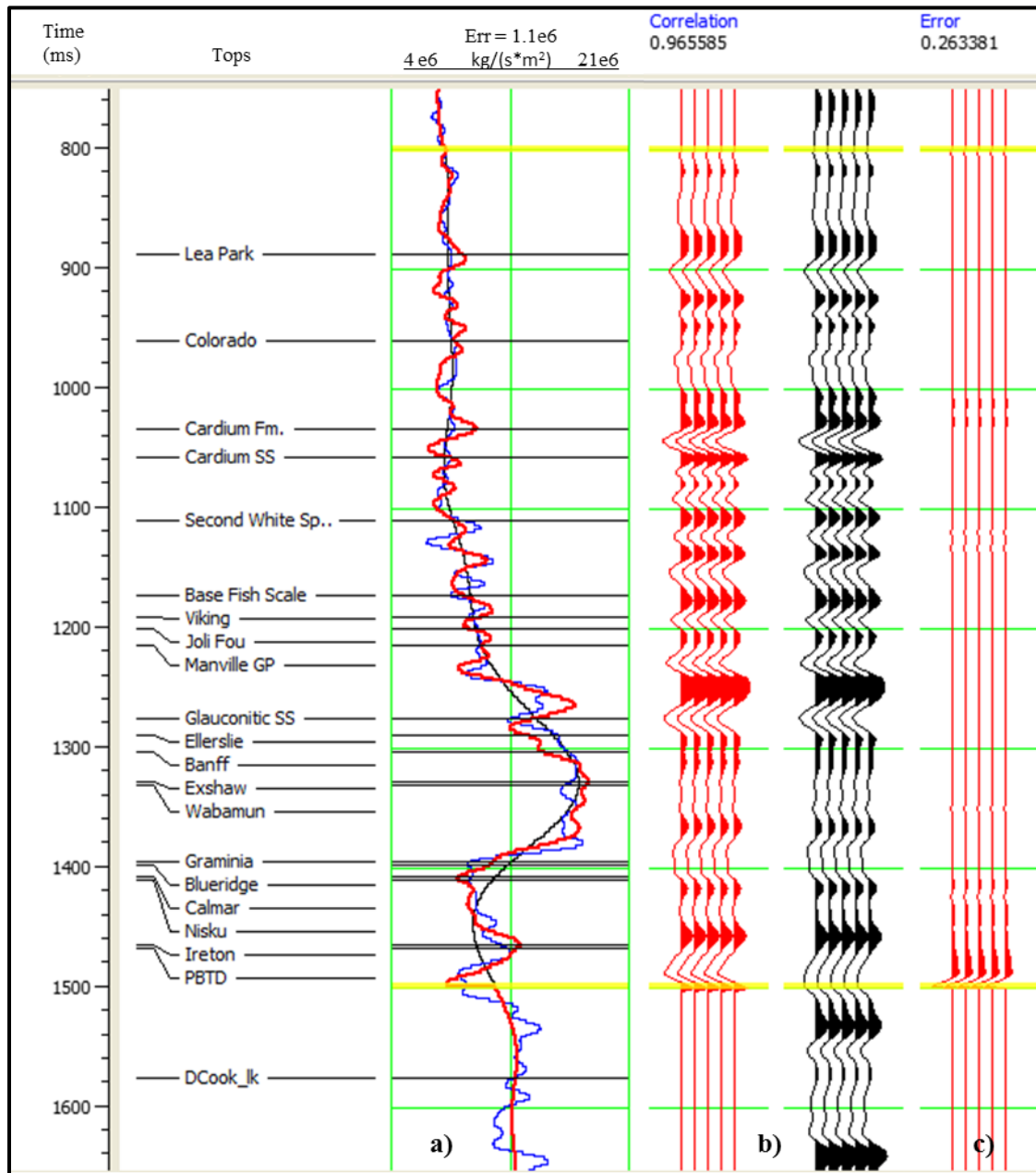


**Figure 3.31: Analysis of the post-stack inversion at Well 8-17 with the initial model cut-off of 0-0-6-10 Hz: a) filtered impedance log (blue), initial model (black), inversion result (red); b) synthetic trace from inversion (red) and extracted trace from the seismic (black), and c) RMS error between synthetic trace and seismic trace.**

### 3.3.5 Inversion Results

Following the analysis at the well location, the model-based inversion of the seismic data was undertaken for both cases. The inversion results of the dataset processed by C&C (case a) (Figure 3.32) and the newly processed dataset (case b) (Figure 3.33) show that the inverted impedance is very close to the actual impedance values. In both cases, in the Winterburn Group the Graminia, Blueridge and Calmar formations were not individually resolved as expected because their thicknesses are below the seismic vertical resolution; in which case, the amplitudes of the recorded seismic data are affected by interference effects from surrounding layer boundaries. The inverted impedance of these units merges with that from Wabamun Group with a higher impedance layer in comparison with the underlying Nisku Formation. The Nisku Formation shows impedance values lower than expected ( $9 \times 10^6 - 19 \times 10^6 \text{ kg/(s} \cdot \text{m}^2)$ ) according to the impedance log analysis ( $> 15 \times 10^6 \text{ kg/(s} \cdot \text{m}^2)$ , Figure 3.21); this could be associated with the higher porosity and permeability of this formation in comparison to the overlying formations plus the fluids present in the Nisku formation (water and gas) which affect the impedance response. Underlying the Nisku Formation, the Woodbend Group shows intermediate ( $\sim 11 \times 10^6 \text{ kg/(s} \cdot \text{m}^2)$ ) and lower ( $\sim 8 \times 10^6 \text{ kg/(s} \cdot \text{m}^2)$ ) impedance values corresponding to the lithologies of these different units, (limestones and shales). The P-impedance log filtered with a high cut of 60/100 Hz was inserted for comparison with the inversion result. Although similar results are seen in both cases, in general case a) shows more continuous layers without much lateral variation. Meanwhile, case b), shows thicker layers with some lateral variations possibly due to the effect of the initial model that has

lower frequency content than that used in case a). Also, the case b) result shows higher resolution within the Colorado Group, below Second White Speckled Shale.

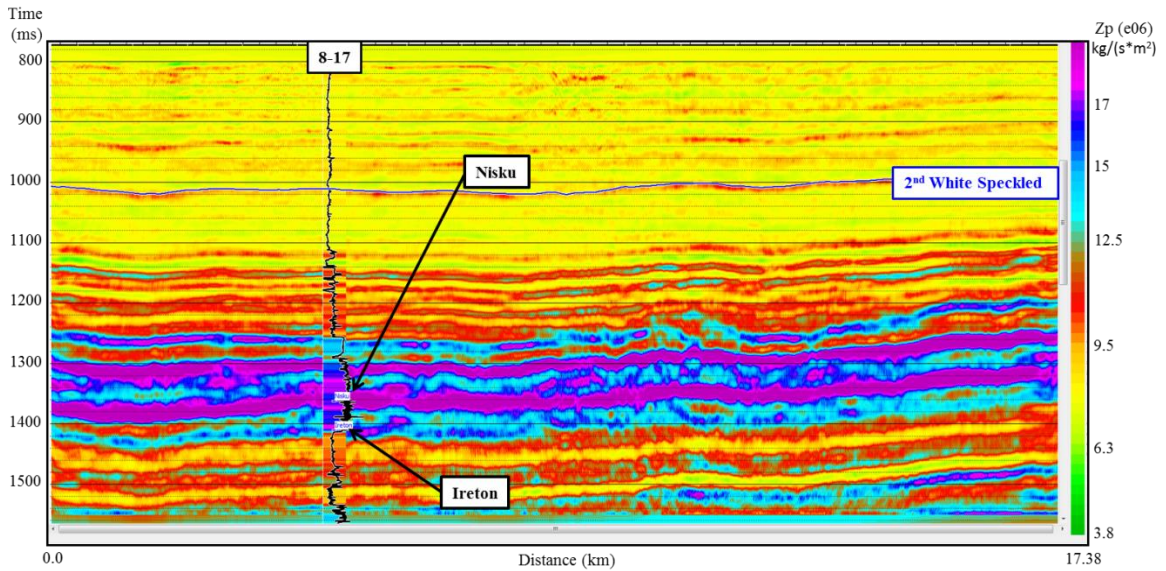


**Figure 3.32: Inversion result of the Highvale seismic data based on previous processing (case a) showing the gamma ray curve in black and the impedance log with a high-cut filter 60/100 Hz in color at the well location for comparison.**

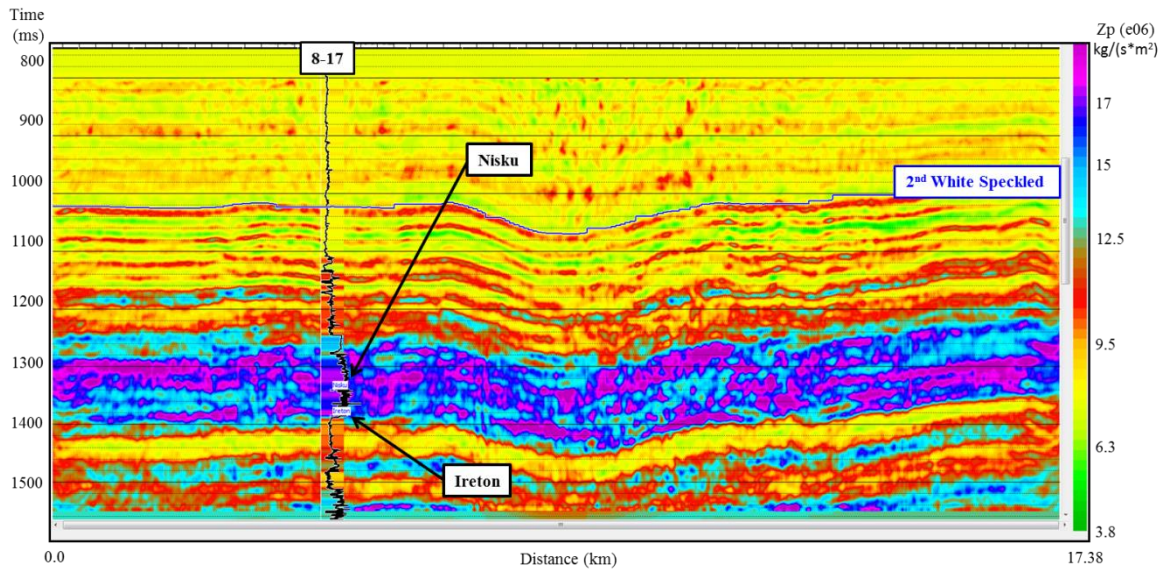


**Figure 3.33: Inversion result of the Highvale seismic data based on new processing (case b) showing the gamma ray curve in black and the impedance log with a high-cut filter 60/100 Hz in color at the well location for comparison.**

Figure 3.34 and Figure 3.35 show with more detail the inversion results within the Wabamun and Winterburn Groups. In both cases, the inversion result at the well location is excellent and with high correlation as indicated in the inversion analysis (Section 3.3.4). Despite the depression observed in case b), no major differences are seen in terms of vertical position of the units at the well location and in the relative variation of the inverted impedance values.

Another important difference is that in case b), the initial model presented several high frequency features related to the horizon used to interpolate the model (Figure 3.29). These features are not observed in the inversion result. Even though the horizon comes from interpreting the seismic data, the inverted impedance is related more to impedance changes at the layer boundaries and the fact that these spikes are not present in the result indicates that the seismic data is dominating the inversion process.

Case a) result presents a cleaner section possibly due to higher apparent resolution evident in the final stack. Case b) result shows more low frequency content from the seismic instead of adding it from the wells in the initial model. This result also proves the importance of taking particular care in the noise attenuation processes during processing to avoid removing low frequency signal which is vital in inversion studies.

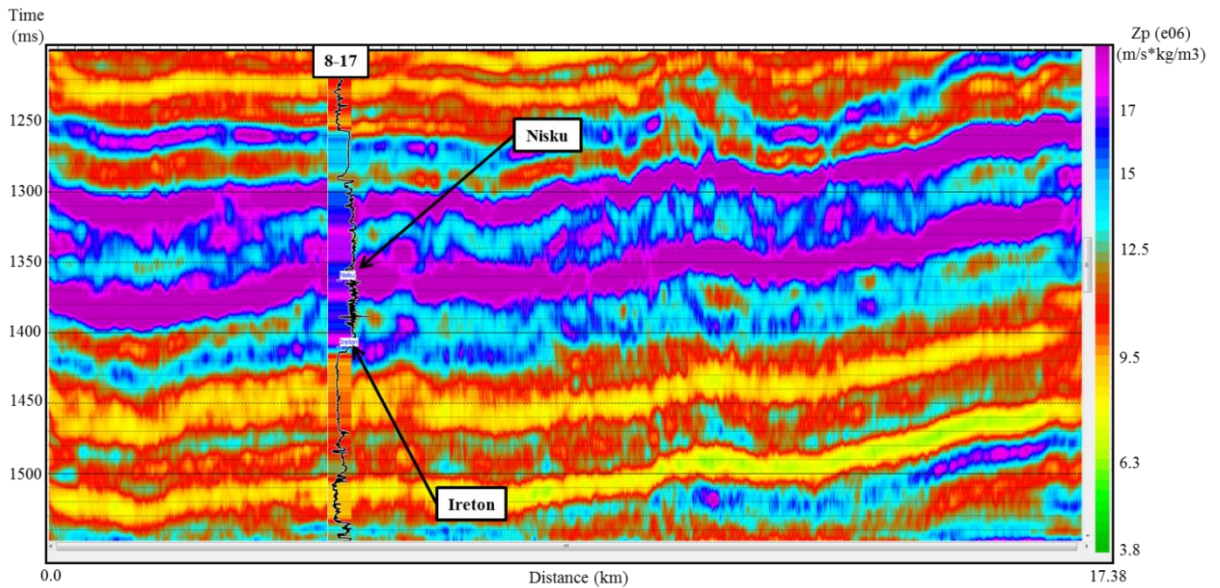


**Figure 3.34: Inversion result of Highvale line previous processing (case a) on Wabamun and Winterburn Groups with the gamma ray curve in black and the impedance log with a high-cut filter 60/100 Hz inserted in colour at the well location for comparison.**

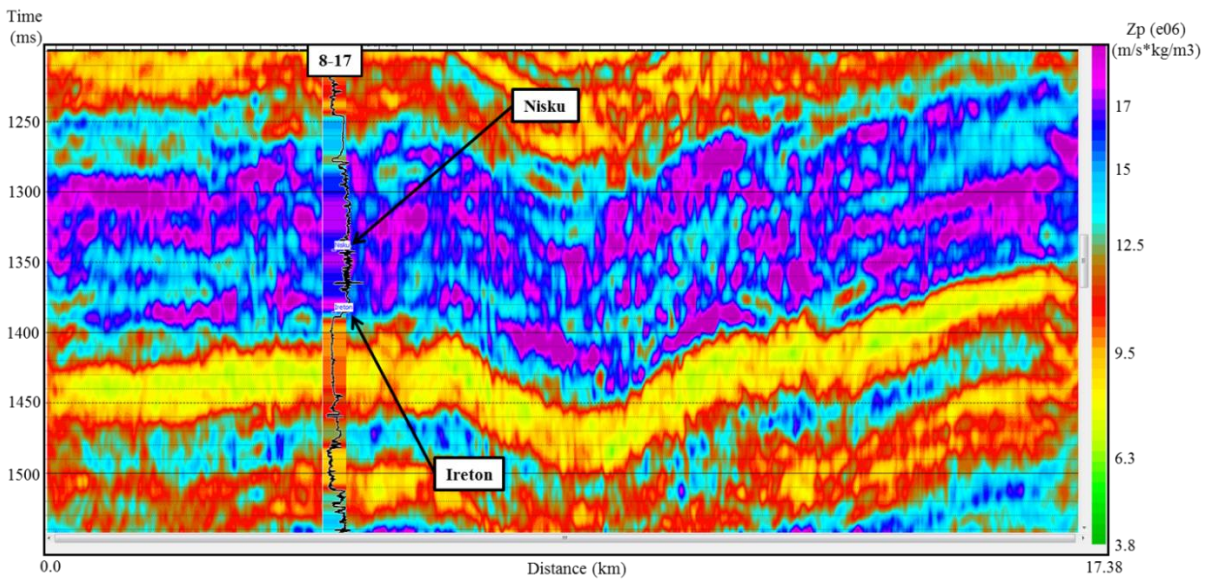


**Figure 3.35: Inversion result of Highvale line current processing (case b) on Wabamun and Winterburn Groups with the gamma ray curve in black and the impedance log with a high-cut filter 60/100 Hz inserted in colour at the well location for comparison.**

### **3.4 Discussion**

The objective of this chapter was to evaluate inversion of different datasets for studying the Nisku Formation. For this purpose seismic and well data from Project Pioneer was used to perform a model-based inversion. The seismic data was provided by TransAlta Corporation and CNRL and consisted in two seismic lines with the processed stacks and raw gathers. The well was provided by Schlumberger and contained a complete set of logs measured down to the Nisku Formation. The well is located on one of seismic lines (Highvale) and was the one used in the inversion study.

The raw gathers were fully processed using two sequences, a conventional one and a specialized one; the conventional sequence used surface wave noise attenuation and spiking deconvolution processes, while the specialized sequence used radial filter and gabor deconvolution. As expected, the specialized processing flow resulted in better attenuation of low frequency noise while keeping the low frequency signal. In comparison with the previous processed stack, current result showed higher low frequency content around the target zone (from ~5-9 Hz) than the previous processing (from ~8-13 Hz), but showed a structural depression in the middle part of the section possibly related with a shallow channel caused by an old meander of the North Saskatchewan River. However, no velocity or statics anomalies were observed during the processing of this dataset.

A model-based inversion was performed in both datasets (previous processing (a) and new processing (b)). In both cases, the inverted impedance showed good results at the well location and presented similar general trend and lateral variations. The inverted impedance in case b) showed a broadband result possibly related with the presence of

more low frequency content in the seismic data. In case a) the result yielded a cleaner section possibly due to more powerful filters applied to the final stack and the units look more continuous without much lateral variation. Both results showed the Nisku Formation with lower values of impedance ( $9 \times 10^6 - 19 \times 10^6 \text{ kg}/(\text{s} \cdot \text{m}^2)$ ) than those expected from the cross plot analysis ( $> 15 \times 10^6 \text{ kg}/(\text{s} \cdot \text{m}^2)$ ); this could be associated with the higher porosity and permeability of this formation in comparison with the overlying formations plus the fluids present in the Nisku Formation (water and gas) which affect the impedance response.

## **CHAPTER 4: 2D SEISMIC MODELLING**

### **4.1 Introduction**

The objective of this chapter is to numerically monitor a CO<sub>2</sub> plume after it has been injected into a saline aquifer, Nisku Formation. The monitoring program is based on measuring the amplitude changes before and after injection using time-lapse seismic data. In this opportunity, an inversion study was performed to further investigate these amplitude changes in terms of their impedance contrast. The first step was to create a 2D geological model that represents the geology of the Wabamun Lake area. Then, a CO<sub>2</sub> plume was designed according to a final volume of 1 million tonnes after 1 year of injection. The plume was then included in the geological model as an anomalous body within the target unit representing the post-injection scenario. Subsequently, both geologic models were used in a 2D seismic simulation to reproduce the seismic response before and after CO<sub>2</sub> injection. Finally, the amplitude change was estimated with a time-lapse analysis and an inversion study to investigate the capabilities of this technique in detecting the CO<sub>2</sub> plume in the Nisku aquifer.

The CO<sub>2</sub> injection simulation was inspired in Project Pioneer dataset characteristics discussed in Chapter 3.

### **4.2 2D Geological Modelling**

The 2D geological model consisted of a 17.38 km long cross-section, created using Norsar-2D software. The structure of the section was based on the parameters of the Highvale line, processed in Chapter 3 (Section 3.2). The geological model was designed combining geological background and well log information from Well 8-17.

To reproduce the stratigraphy and layering of the model, gamma ray, velocity and density logs were used. The geological background given in Section 3.1.2 was used as a reference to understand the regional geology. The sedimentary succession presents gently dipping in the southwest direction of the Wabamun lake area (Figure 3.1) and no major faults are known in the area (Michael et al., 2008). Based on the seismic character from data presented in Chapter 3, a flat layer design was chosen to reproduce the local geologic model. The units utilized in defining the blocks were selected based on the key formation tops identified in the logs as well as the seismic data. Fourteen layers were defined based on the average values of the target logs for each of them (Figure 3.4). Table 4.1 summarizes the velocities and density values for each block.

**Table 4.1: Geological model parameters. The target formation is indicated in red**

| Block | Depth (Km)   | Vp (m/s)    | Vs (m/s)    | $\rho$ (g/cc) | Formation          |
|-------|--------------|-------------|-------------|---------------|--------------------|
| 1     | 0.0          | 1900        | 1590        | 2.3           | Shallow surface    |
| 2     | 0.1          | 1920        | 1600        | 2.3           | Shallow - Lea Park |
| 3     | 0.773        | 3000        | 1610        | 2.35          | Lea Park           |
| 4     | 1.27         | 3300        | 1620        | 2.5           | Viking             |
| 5     | 1.533        | 3700        | 2000        | 2.68          | Banff              |
| 6     | 1.605        | 5410        | 3029        | 2.61          | Exshaw             |
| 7     | 1.613        | 3795        | 2195        | 2.74          | Wabamun            |
| 8     | 1.764        | 6000        | 3300        | 2.67          | Graminia           |
| 9     | 1.769        | 5889        | 3328        | 2.78          | Blueridge          |
| 10    | 1.787        | 5890        | 3350        | 2.77          | Calmar             |
| 11    | <b>1.793</b> | <b>5500</b> | <b>3150</b> | <b>2.8</b>    | <b>Nisku</b>       |
| 12    | 1.897        | 6200        | 3300        | 2.77          | Ireton             |
| 13    | 2.0          | 5000        | 2660        | 2.8           | Duvernay/Leduc     |
| 14    | 2.14         | 4000        | 2100        | 2.77          | Basal Cooking Lake |

The option “Model Builder” from Norsar-2D software was used to create the geological model. This option allows defining the geometry of the model by setting the boundaries in terms of distance and depth (X and Y coordinates). In this rectangular section, a series of interfaces were created to represent the geological structure of the study area. The depth of each interface is also defined in terms of its coordinates. Once these interfaces were created, the space between each of them represents a block. These blocks are then filled with the properties  $V_P$ ,  $V_S$  and density obtained from the well log values summarized in Table 4.1. Figure 4.1 shows the baseline geological model. The model size is 17.38 km long and 2.5 km deep. The Nisku Formation is the 11<sup>th</sup> block found at a depth of 1.793 km.

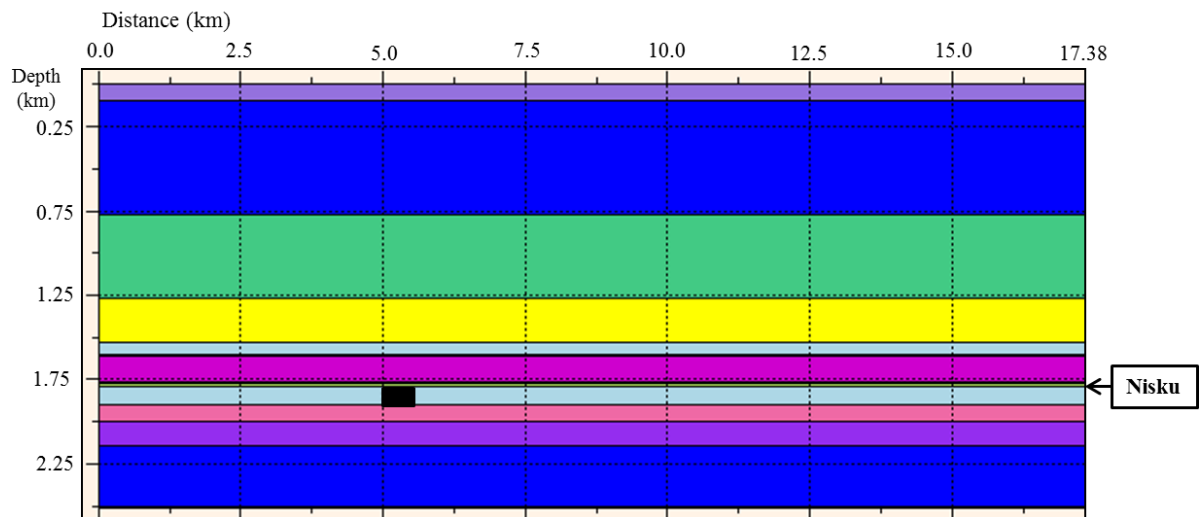


**Figure 4.1: 2D geological model. The location of the injection zone in the Nisku Formation is indicated by the black rectangle.**

### 4.3 CO<sub>2</sub> Plume Simulation

Frailey (2009) explained the methods for estimating the volume of CO<sub>2</sub> trapped in geological formations. The static approach requires rock and fluid properties while the

dynamic approach requires information about active injection, injection volumes and reservoir pressure. The static technique was applied in this project, specifically the volumetric method which is summarized in Figure 4.2. A cylinder or disk was selected to estimate the CO<sub>2</sub> volume and corresponding radius of extension (Vera, 2012).

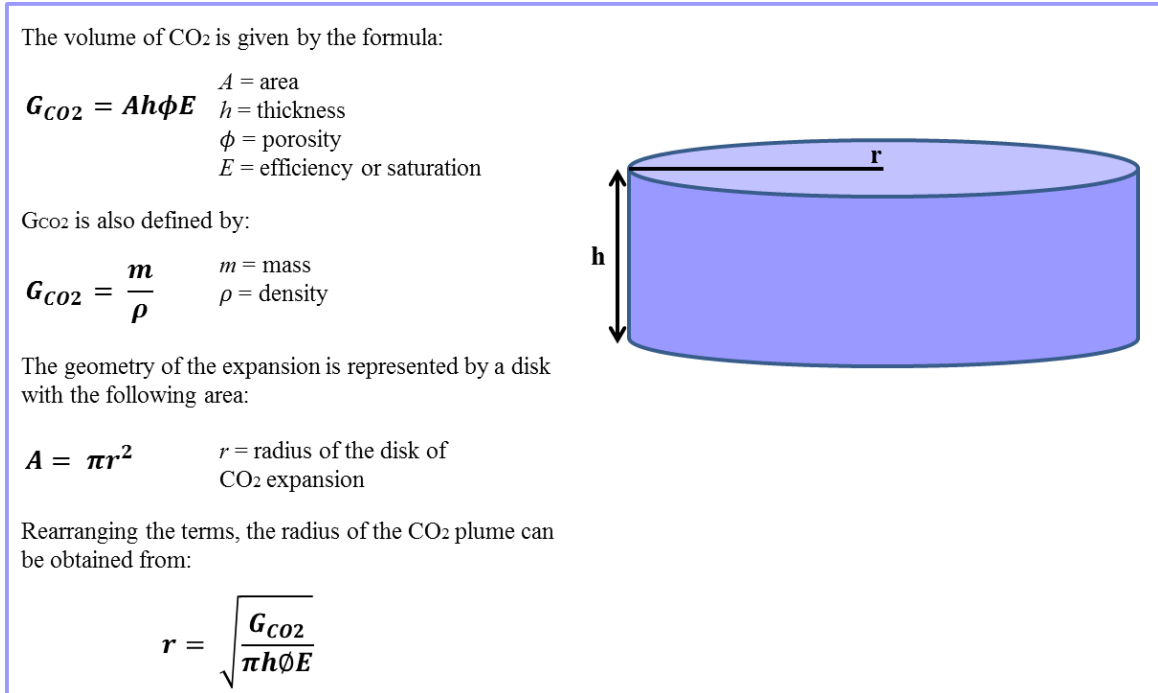


**Figure 4.2: CO<sub>2</sub> plume designed.**

The amount of CO<sub>2</sub> simulated in this experiment was 1 million tonnes after one year of injection. Based on the data presented at Chapter 3, the Nisku Formation has a thickness  $h = 103.85$  m, porosity  $\phi = 7.3\%$  and density  $\rho = 653$  kg/m<sup>3</sup>. The efficiency, considered as the CO<sub>2</sub> saturation, was estimated for 100% saturation ( $E = 1$ ) in the available pore space. Using the equations in Figure 4.2 the radius of the disk was calculated to have a value of 253.57 m.

It is important to notice that even when a 3D model was used to estimate the plume size the final geological model is in 2D, therefore the presented cylinder was translated into a rectangle with a longitude equal to the diameter of the cylinder ( $d = 507.14$  m).

The monitor geological model represents the post-injection scenario. For this case, the rectangular  $\text{CO}_2$  plume was inserted in the same geological model of the baseline case. Two new interfaces had to be defined to introduce this plume (Figure 4.3). The layer corresponding to the Nisku Formation was divided in three parts where two of these intervals have the same properties as the baseline model (representing 0% of  $\text{CO}_2$  saturation). The third interval represents the injection zone, with velocities and density change values obtained from the Gassmann fluid substitution (Gassmann, 1951) analysis done by Ashuhail (2011), summarized in Table 4.2.

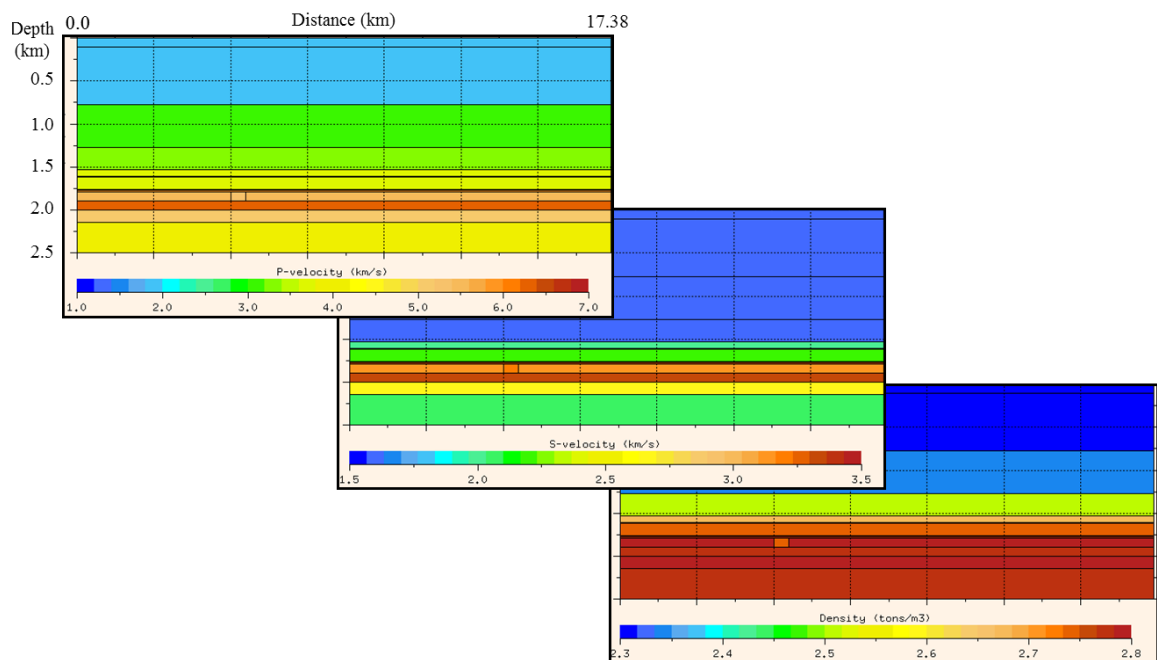


**Figure 4.3: Monitor 2D geological model ( $V_P$ ,  $V_S$  and  $\rho$ ). The rectangular  $\text{CO}_2$  plume is inserted in the Nisku Formation.**

**Table 4.2: Velocities and density values of the CO<sub>2</sub> plume. The percentages change was obtained from the Gassmann fluid substitution analysis performed by Alsu hail (2011).**

| Properties           | Percentage change (%) | Initial values | New values |
|----------------------|-----------------------|----------------|------------|
| V <sub>P</sub> (m/s) | -4.5                  | 5500           | 5252.5     |
| V <sub>S</sub> (m/s) | 0.635                 | 3150           | 3170       |
| ρ (g/cc)             | -1.26                 | 2.8            | 2.76       |

#### 4.4 2D Seismic Modelling

The 2D geological models generated previously were input into the 2D seismic modelling algorithm. The goal was to generate the seismic data that would allow performing the time-lapse analysis for monitoring the CO<sub>2</sub> plume. The seismic survey was designed using the same acquisition parameters of the Highvale line discussed in section 3.2.1 and these are shown in Figure 4.4. The line length is 17.38 km, shots spacing is 80 m, receiver spacing is 20 m. The total number of channels is 200 and the array is split-spread with an offset maximum of 2000 m. NORSAR-2D “Common Shot Ray Tracer” algorithm was used to obtain the reflectivity events which were later convolved with a zero-phase Ricker wavelet of 30 Hz to create the synthetic seismograms for each case. Figure 4.5 shows an example of a shot gather from the baseline case where the reflections represent the 17 interfaces.

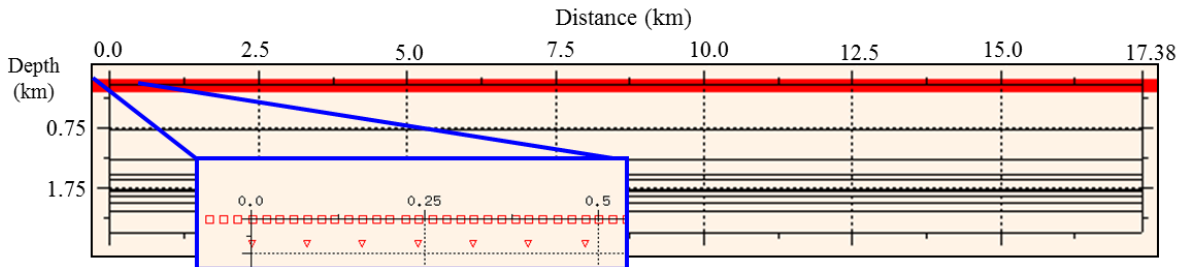


**Figure 4.4: 2D seismic modelling survey design. The line is 17.38 km long with 80 m shots spacing and 20 m receivers spacing.**

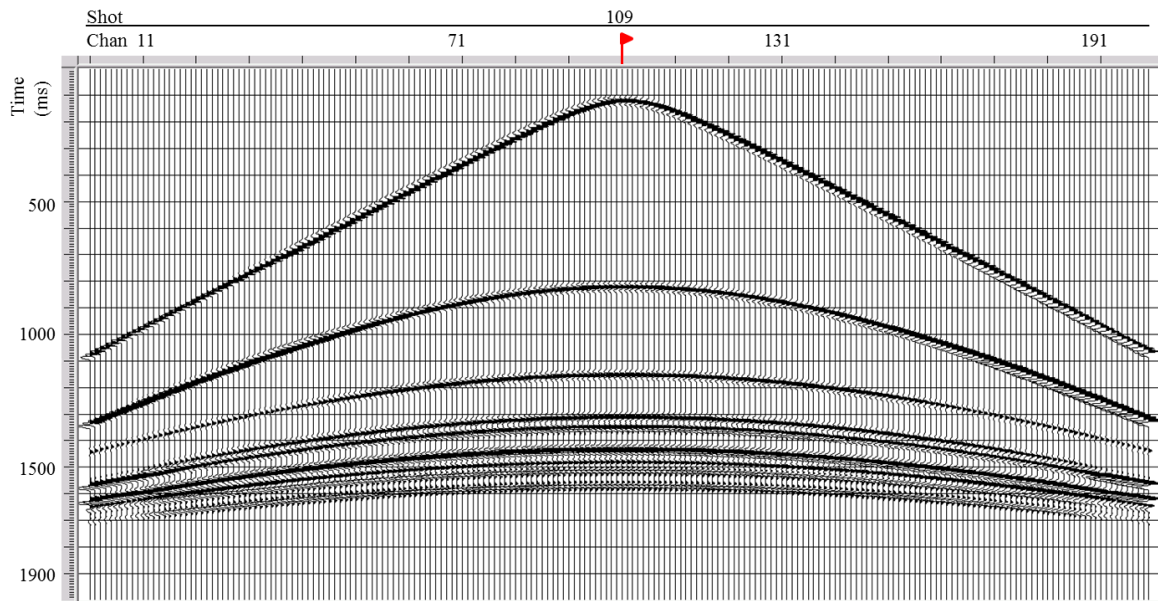


**Figure 4.5: Shot gather 109 from baseline 2D modelling. 200 channels per shot.**

The data processing in this case is much simpler than the processing flow explained in Section 3.2.2. Since no noise or statics effect are present in these models the steps to stack the shot gathers consist of, after assigning the geometry, applying the NMO correction and creating the CDP stacked section. The NMO correction needs a RMS P-wave velocity function (Figure 4.6) which was obtained from converting, through Dix's equation (Dix, 1955), the interval velocity field defined in the geological models (Tables 4.1 and 4.2).

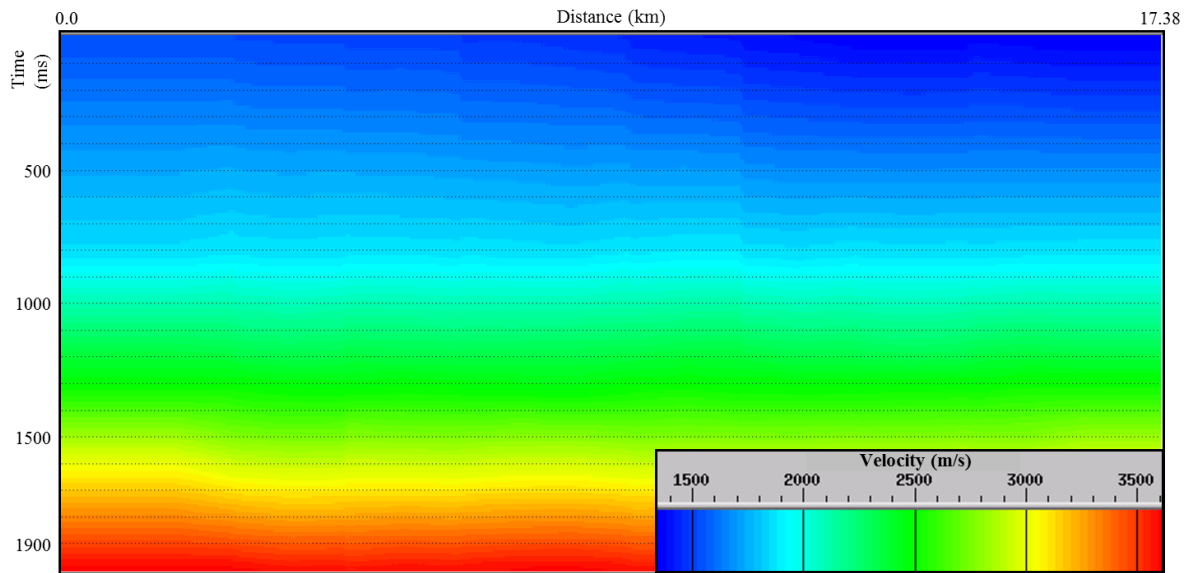


**Figure 4.6: RMS P-wave velocity field converted from the interval velocity field defined in the 2D baseline geological model.**

Figure 4.7 shows the result of the NMO correction and the stacking processes where a) it is the CDP stack section of the baseline case (0% CO<sub>2</sub> saturation), while b) it is the CDP stack section of the monitor case (100% CO<sub>2</sub> saturation). In the monitor section the injection zone in the target formation is evident. A time shift in the base of the plume and amplitude distortion below it is clearly observable.

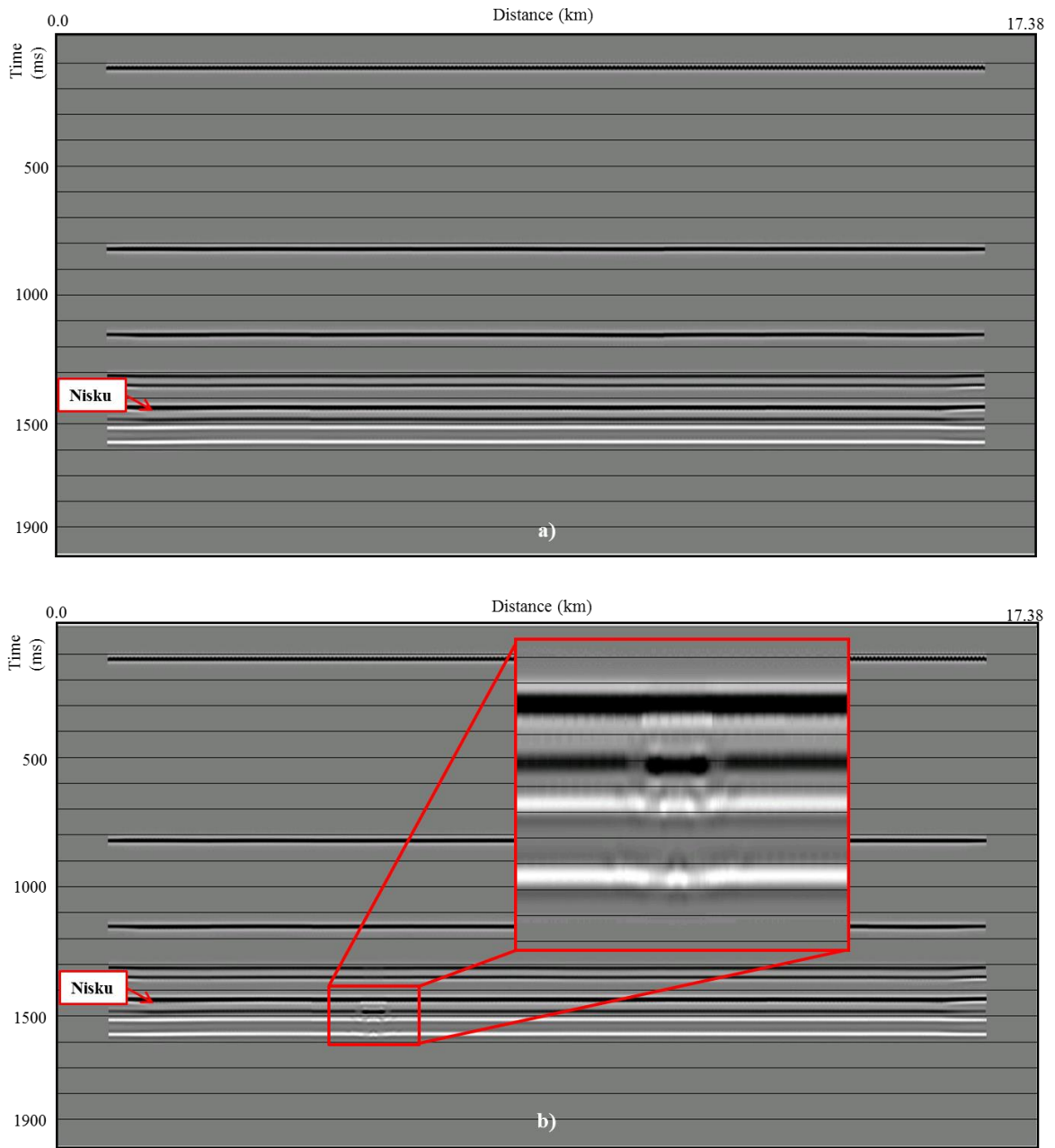


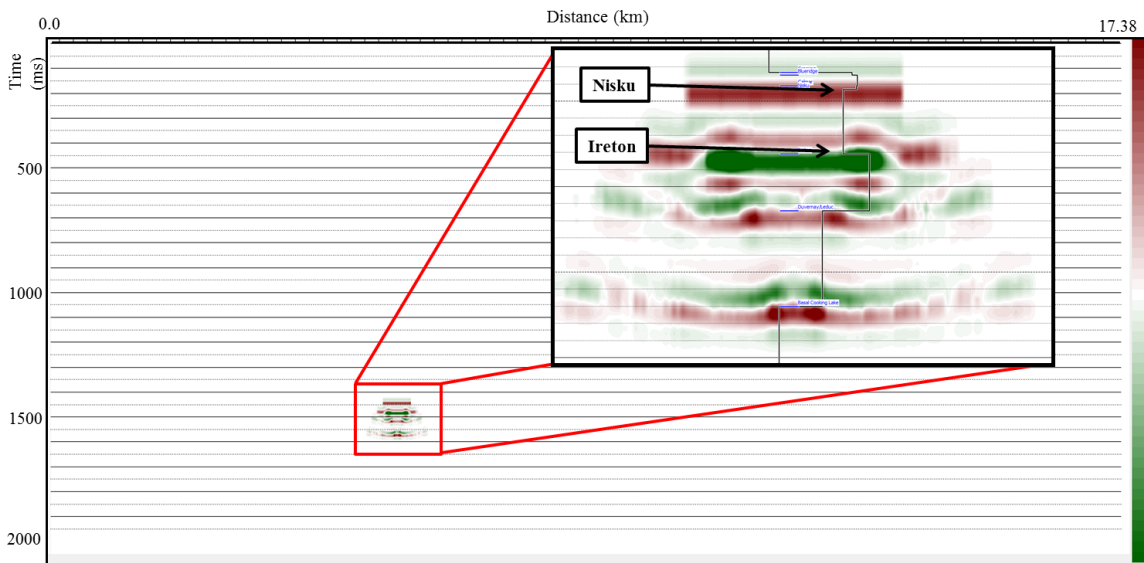
**Figure 4.7: a) Baseline CDP stack section, b) Monitor CDP stacked section. Injection zone is indicated in red square.**

## 4.5 2D Seismic Monitoring Results

The effects of injecting CO<sub>2</sub> into a saline aquifer were discussed in section 1.1.2.2. Once the 2D seismic modelling was completed, the next step was to analyze the changes in physical properties, such as reflectivity, time shift and velocity in the monitor data.

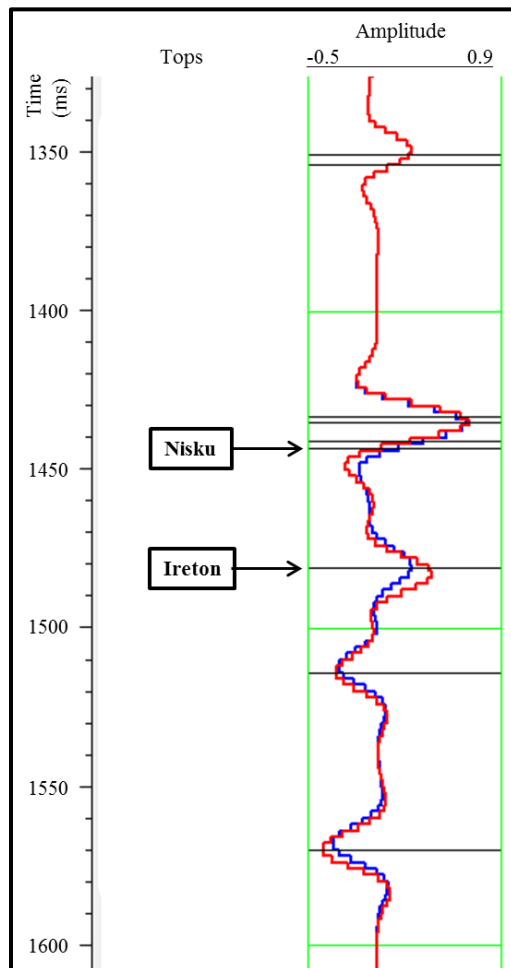
### 4.5.1 Seismic Amplitudes Direct Comparison:

Figure 4.8 shows the effect in the injection zone determined from subtracting the monitor CDP stacked section data from the baseline section data. This difference represents 100% CO<sub>2</sub> saturation in the injection zone. The traces outside the injection area were cancelled and only the injected region and reflectors below it are affected. This response is made up of the difference in amplitude and travel time expected from the changes that fluid substitution produces in the seismic data.



**Figure 4.8: Difference between baseline CDP stack and monitor stack. The red square highlights 100% CO<sub>2</sub> injection zone.**

In order to quantify these changes, traces at CDP location 726 were extracted from both the baseline and monitor sections. Figure 4.9 shows the comparison of these traces. The reflection from the base of the Nisku Formation shows a time shift of 1.81 ms, and the RMS amplitude changed over a window from 1442 ms to 1482 ms by about 30% after injecting CO<sub>2</sub>.



**Figure 4.9: Comparison of baseline (blue) and monitor (red) traces at CDP location 726.**

The edges and top of the CO<sub>2</sub> plume is clearly identified in Figure 4.8. However, the bottom of the plume is hard to isolate from the reflectors underneath due to velocity

pushdown in the monitor survey. The edges of the plume are located between CDPs 702 and 752. Each CDP is separated by 10 m meaning that the width of the plume has a value of 500 m, accurately predicted from the geological model and the difference section.

#### 4.5.2 Impedance Comparison after Seismic Inversion:

Following the same approach of the two previous study cases, a model-based inversion was performed on each CDP stacked section (baseline and monitor) to evaluate the impedance sensitivity in detecting the CO<sub>2</sub> plume.

Since in this case synthetic data is been used, the first step was to create synthetic well logs ( $V_P$  and  $\rho$ ) to help constrain the impedance initial model. The  $V_P$  and density values (Table 4.1) used to build the 2D geological model were used to create these well logs. Figure 4.10 shows the broadband wavelet from the seismic for the well tie process of the synthetic well logs with the baseline section (Figure 4.11). The final correlation coefficient was 0.93.

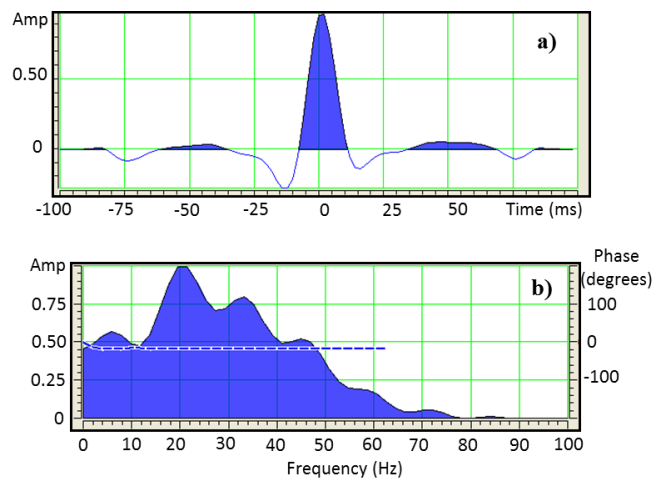


**Figure 4.10: a) Wavelet extracted from synthetic well with the baseline CDP stacked section. b) Amplitude spectrum. The dotted line indicates the average phase of the wavelet (-14°).**

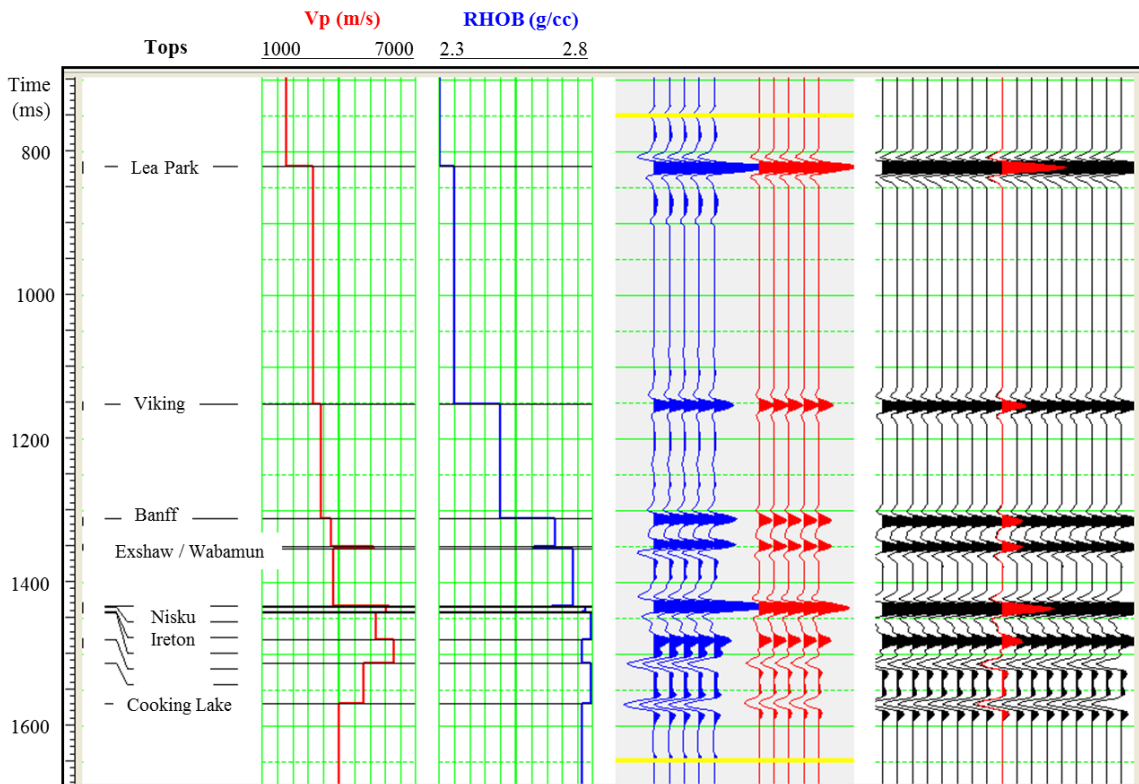


**Figure 4.11: Tie process of synthetic  $V_P$  and density logs with the baseline CDP stacked section. Blue traces represent the synthetic seismogram; red traces represent the extracted trace from the seismic data at the well location, and black traces shows the ten traces around the well location. Yellow bars show the correlation window. Correlation = 93%.**

The P-impedance ( $Z_P$ ) initial model was generated using a  $Z_P$  log calculated with the sonic and density logs from the synthetic well. Since synthetic data is used in this analysis, no low-pass filter was applied in this case. The initial model was generated using the exact impedance values of the synthetic  $Z_P$  log. P-impedances in the model range from  $4 \times 10^6$  to almost  $16.5 \times 10^6$  kg/(s\*m<sup>2</sup>). Figure 4.12 shows an example of the inversion analysis performed with the initial model and the baseline CDP stacked section in a window from 750 ms to 1650 ms. The correlation between the synthetic (red) and the seismic trace (black) has a high correlation coefficient (0.99). The estimated RMS error

between synthetic trace and the seismic trace is 0.053. The RMS error between the target log and the predicted log curves is  $3.49 \times 10^5 \text{ kg}/(\text{s} \cdot \text{m}^2)$ , or 2 %.

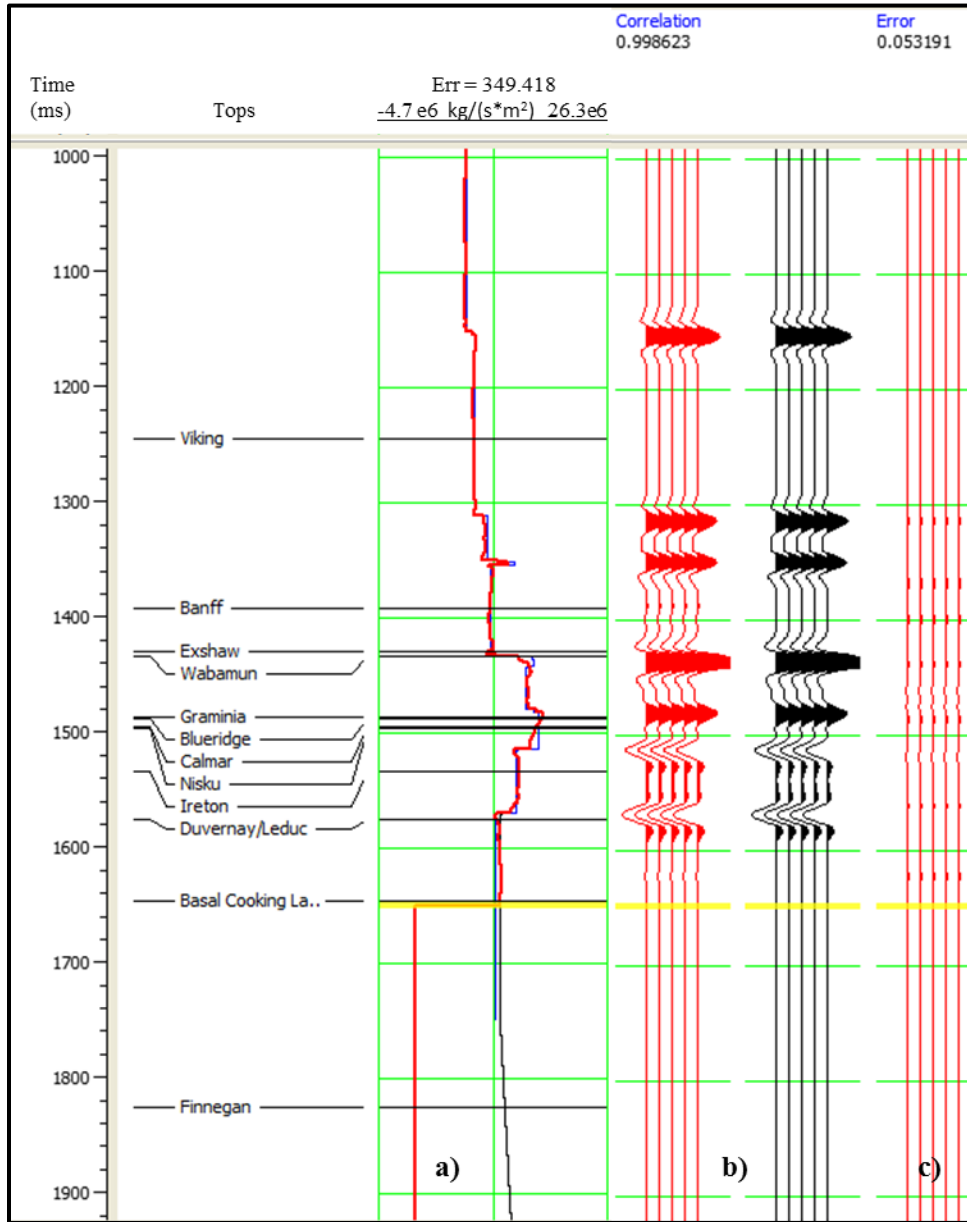


**Figure 4.12: Analysis of the post-stack inversion at synthetic well location: a) filtered impedance log (blue), initial model (black), inversion result (red); b) synthetic trace from inversion (red) and extracted trace from the seismic (black), and c) RMS error between synthetic trace and seismic trace.**

Following the analysis at the well location, the model-based inversion was undertaken for the baseline and monitor datasets. Figure 4.13 shows the inversion results of (a) the baseline CDP stacked section and (b) the inversion results of the monitor CDP stacked section. The inverted impedance shows the exact impedance values of the initial model except in the monitor case where a distortion is evident in the injection zone and the impedance values of the plume have decreased.

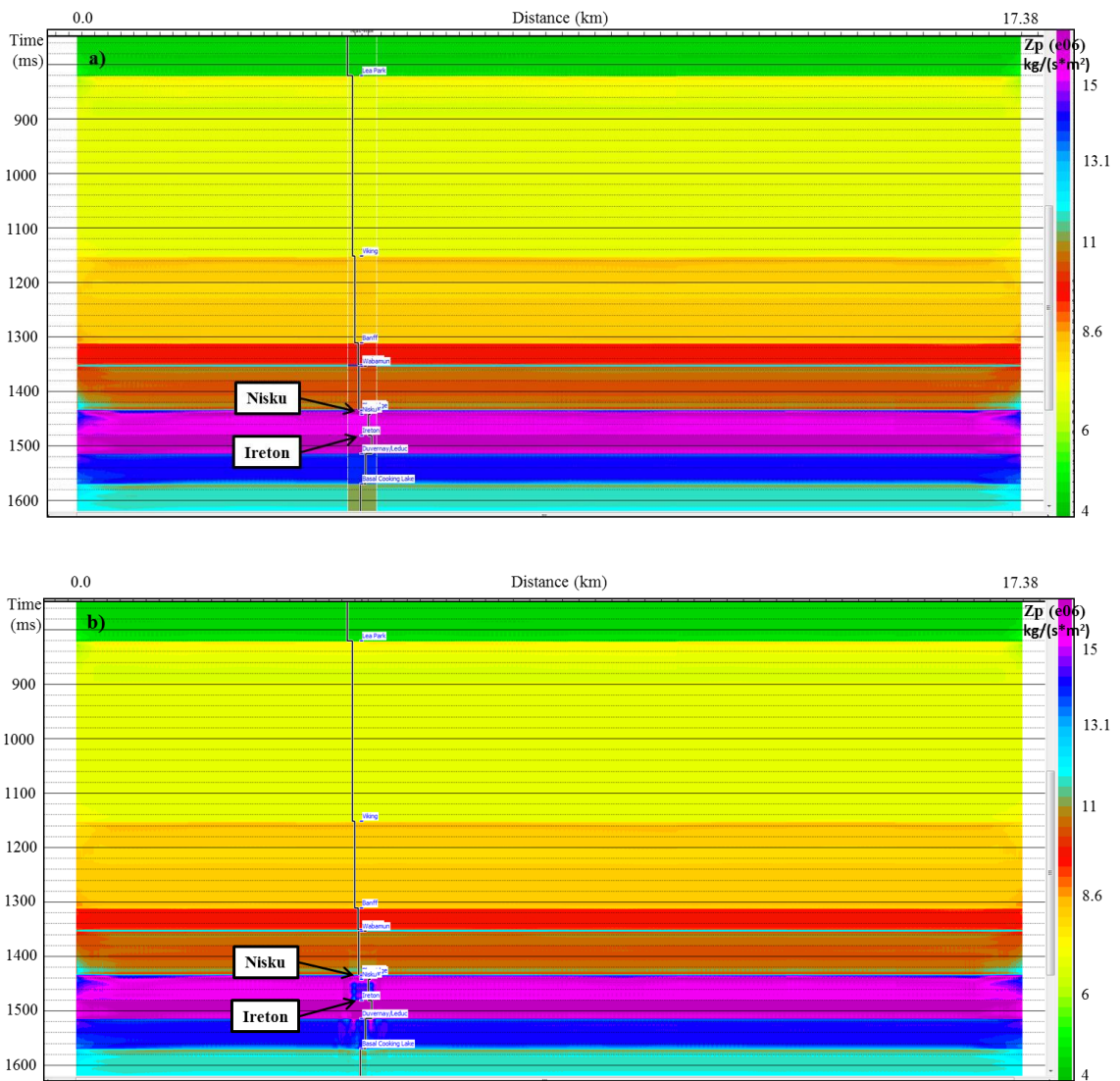


**Figure 4.13: a) Baseline inversion, b) Monitor inversion. Distortion in the impedance values in the injection region and reflectors underneath is evident.**

Numerical impedance changes in traces at CDP location 726 were extracted from the inverted baseline and monitor sections. Figure 4.14 shows the comparison of these traces. A decreased in the impedance values of ~7% is observed after injecting CO<sub>2</sub> in the Nisku Formation. This percentage enhances the detectability of the plume since combining the effect of V<sub>P</sub> and ρ, is effective and is in agreement with the expected values from the fluid substitution analysis (Table 4.2).

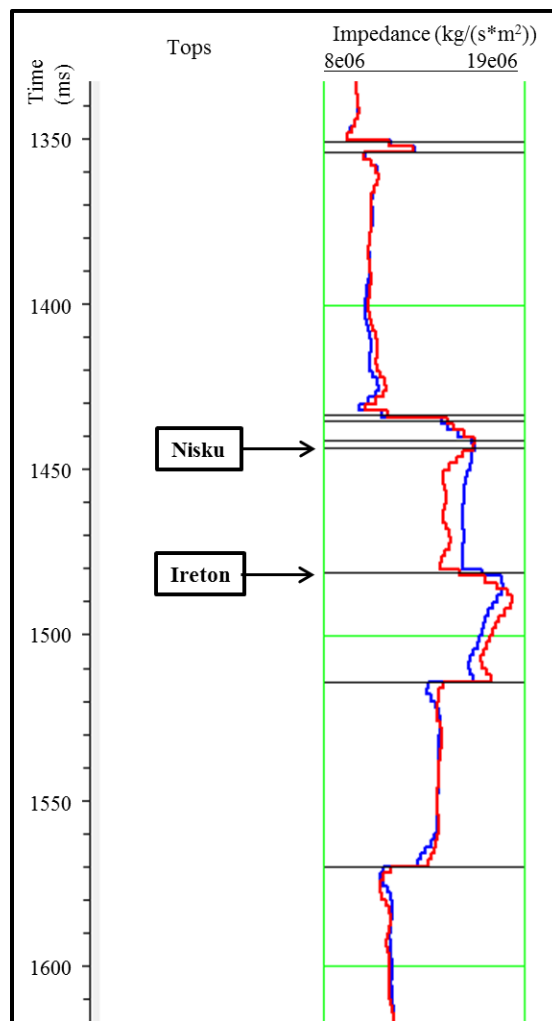


**Figure 4.14: Comparison of baseline (blue) and monitor (red) inverted traces at CDP location 726.**

Similar to the differenced stacked sections, Figure 4.15 shows the effect within the injection zone determined from subtracting the monitor impedance section from the baseline impedance section. This difference represents the 100% CO<sub>2</sub> saturation zone. The traces outside the injection area were cancelled and only the injected region and reflectors below it are affected. The reflectors below the CO<sub>2</sub> plume are not as distorted as was seen in Figure 4.8. It is possible that the impedance changes in that region are not that significant so they were not resolved after the subtraction process. However, some artifacts are still present at the edges of the plume.

It is important to notice that these results identify the shape of the CO<sub>2</sub> plume even more clearly than just by directly comparing the differences in the seismic amplitudes. The top, base and sides of the plume are easily identifiable. The edges of the plume are again located between CDPs 702 and 752. Therefore, the width of the plume is accurately predicted from the inverted section difference (500 m).

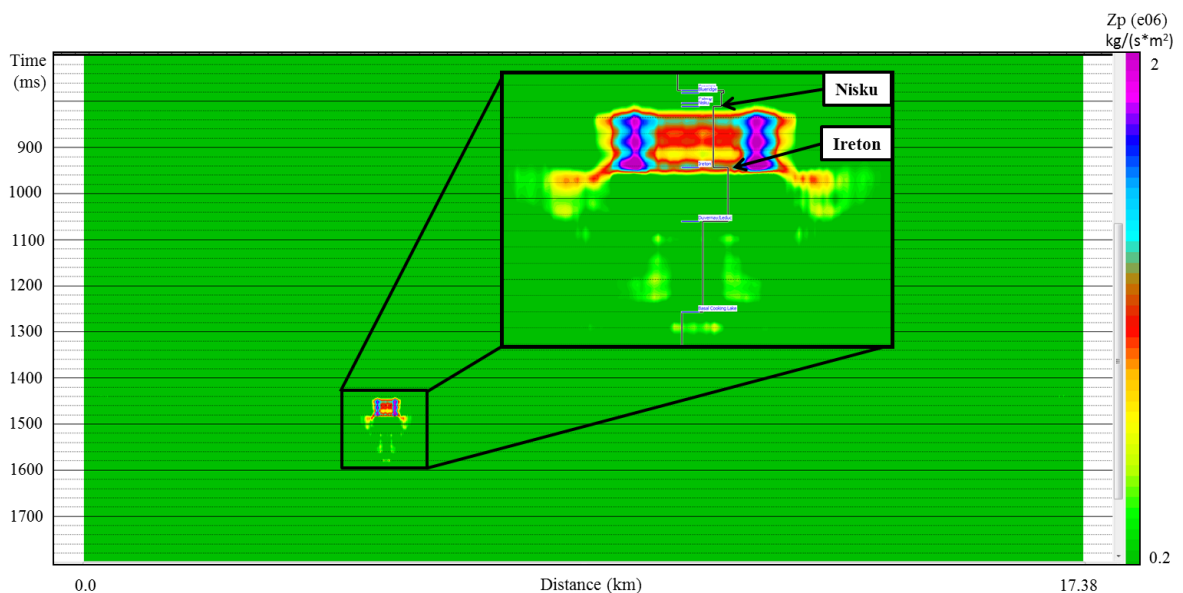


**Figure 4.15: Difference between baseline inversion and monitor inversion. The black square highlights 100% CO<sub>2</sub> injection zone.**

A final test was undertaken to test the sensitivity of the inversion method by inverting the impedance difference rather than differencing the inversion of the monitor and baseline data. The difference of the CDP stacked sections (Figure 4.8) was taken into a model-based inversion analysis using as an initial model the impedance difference log. Therefore in this case just the effect of the CO<sub>2</sub> plume will contribute in the inversion study. Figure 4.16 shows the inversion analysis performed at the synthetic well location (CDP 726) in a window from 1400 ms to 1600 ms. The initial model was generated using the exact impedance values of the difference  $Z_p$  log. P-impedance differences in the model range from 0 to almost  $30 \times 10^4$  kg/(s\*m<sup>2</sup>). The correlation between the synthetic (red) and the seismic trace (black) has a high correlation coefficient (0.98). The estimated RMS error between synthetic trace and the seismic trace is 0.22. The RMS error between the target log and the predicted log curves is  $2.55 \times 10^3$  kg/(s\*m<sup>2</sup>), or 8.5 %.

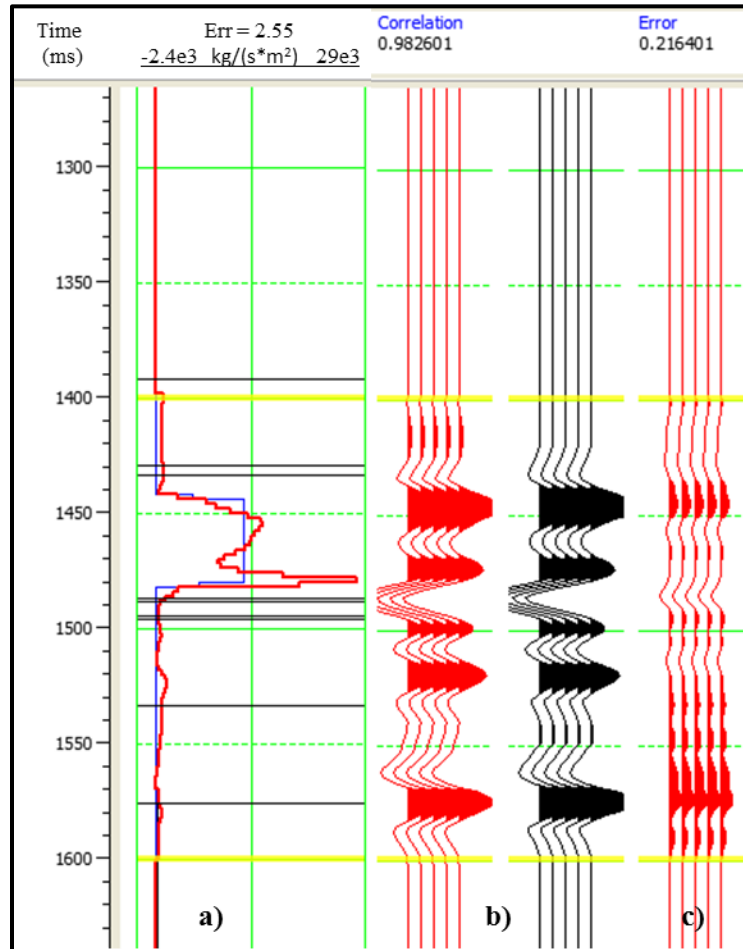


**Figure 4.16: Analysis of the post-stack inversion of the CDP stack section difference at synthetic well location: a) filtered impedance log (blue), initial model (black), inversion result (red); b) synthetic trace from inversion (red) and extracted trace from the seismic (black), and c) RMS error between synthetic trace and seismic trace.**

In Figure 4.17 the result of the difference inversion is displayed in comparison with the difference of the independent inversions showed in Figure 4.13. Both look very similar but with different residual impedance values. These values are strongly related with the initial model that was used to run the inversion. Since Hampson-Russell inversion algorithm was developed to deal with full bandwidth seismic data, it is interesting to see that it performed quite well in the inversion of the difference.

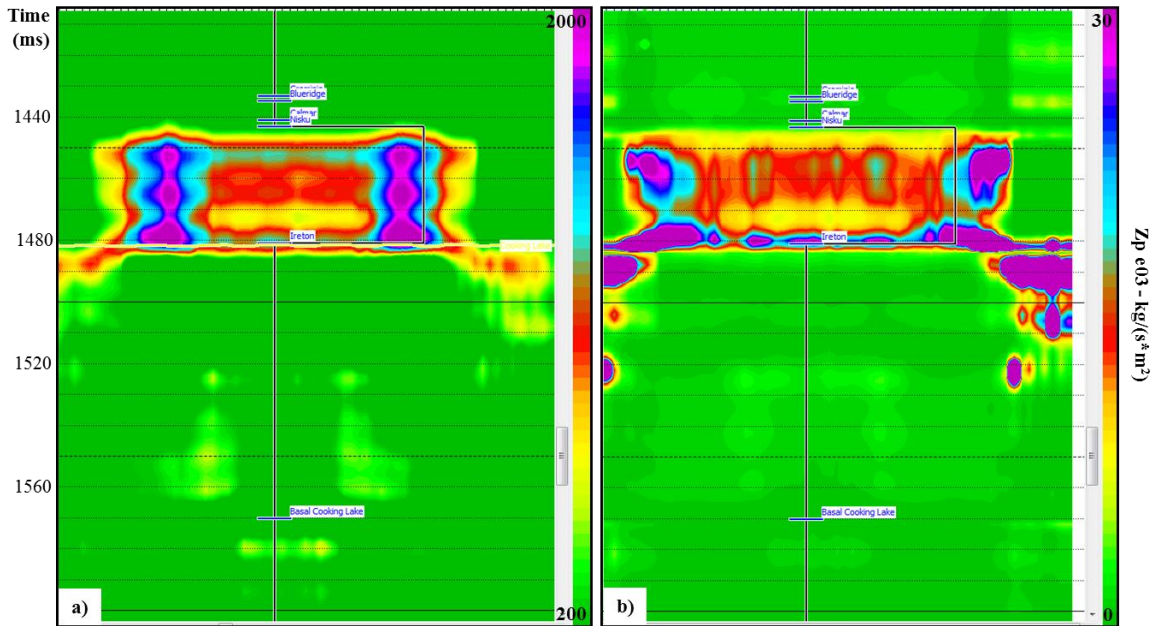


**Figure 4.17: a) Difference of impedance sections in Figure 4.13, and b) inversion of the difference on Figure 4.8.**

#### 4.6 Discussion

The 2D seismic modelling undertaken in this study allowed us to simulate a CO<sub>2</sub> injection scenario within the Nisku saline aquifer. The geological model was based on the seismic analysis discussed in Chapter 3 and well log information. The post-injection seismic section shows a time delay of 1.8 ms of the basal reservoir reflector and amplitude change of ~30% with respect to the baseline case. The shape of the plume is more evident after calculating the difference between the sections where the top and width of the body are clearly distinguishable, while the bottom of the plume is hard to identify due to time delay in deeper reflectors. The 500 m length of the plume was accurately predicted according to the geological model.

To further investigate the seismic changes caused by injection of CO<sub>2</sub> a model-based inversion study was performed to determine these changes in terms of impedance contrast. A decrease in the impedance values of ~7% is observed in the post-injection scenario. As expected, the impedance change is stronger due to the combination of V<sub>P</sub> and  $\rho$ . In this case, the shape of the plume is even more evident since the base is less affected by the underlying reflectors. It is possible that the impedance changes of the reflectors underneath the plume are not significant and got cancelled after the subtraction process.

The test of inverting the residual CDP stacked section gave interesting results even though the inversion algorithm is designed to use full bandwidth seismic data.

## CHAPTER 5: CONCLUSIONS

### 5.1 Conclusions

The main goal of this thesis was to evaluate the influence of using broadband seismic data in inversion studies. Three study cases were used to accomplish this goal and they were all analyzed under the Hampson-Russell model-based inversion approach. The following conclusions have arisen based on the results of this research study:

- Low-frequency component in seismic data adds valuable information to inversion studies. The inversion initial model has a strong influence in inversion results and this effect can be alleviated if broadband seismic data is used for this techniques. The Hussar Experiment showed the advantage of preserving the low-frequency component from acquisition through to processing. The Highvale line, from Project Pioneer, proved the importance of taking special care of noise attenuation processes which appear to be the most critical in attenuating low-frequency signal. Radial filter was applied in both datasets and demonstrated to be useful in suppressing coherent noise while retaining low-frequency signal.
- The seismic data processing performed on the Highvale line showed differences in the reflection structure in comparison with the previous processed data. This difference is attributed to the thickening of the weathering layer suggesting that it is quite likely that the river meandered through the region depositing a significant amount of unconsolidated material. This effect could have resulted in a large time delay going through the material resulting in higher statics corrections. However, no velocity or statics anomalies were observed during the processing of this dataset.

- Impedance changes are easily identifiable if the contrast with surrounding layers is considerable; as in the Hussar study case where the Glauconitic Sandstone can be isolated from more shaly units. In the Project Pioneer case, the Nisku Formation has similar impedance values than the overlain units from the Winterburn Group (Graminia, Blueridge and Calmar). However, the Nisku Formation shows impedance values lower than expected according to the log analysis; possibly associated with the higher porosity and permeability of this formation in comparison with the surrounding formations. Also, the fluids present in the Nisku formation (water and gas) could have affected the impedance response.
- In both the Hussar Experiment and Project Pioneer cases, lateral variations in the inversion results are associated to the presence of low-frequency signal in the seismic data suggesting that the seismic reflections are controlling the impedance response. This feature is not observed when the low-frequency component is added from the inversion initial model.
- In the CO<sub>2</sub> injection simulation case, the post-injection seismic section shows a time delay of 1.8 ms of the basal reservoir reflector and amplitude change of ~30% with respect to the baseline case. Also, a decreased in the impedance values of ~7% is observed in the post-injection scenario. As expected, the impedance change is stronger due to the combination of  $V_P$  and  $\rho$ . The impedance changes of the reflectors underneath the plume are not significant and got cancelled after subtracting the monitor stacked section from the baseline stacked section making

easier the identification of the CO<sub>2</sub> plume. The shape of the plume was accurately estimated having a width of 500 m.

## 5.2 Recommendations

This thesis focused on the impact of broadband seismic data in inversion studies specifically using post-stack data and the Hampson-Russell model-based inversion approach. The following recommendations have been made to further investigate this topic:

- Use other post-stack inversion techniques and compare their results. Most of them appear to have less influence from the initial model but fail to reproduce detailed impedance changes.
- Include 3D seismic data and more well log information to have more control in the expected impedance behaviour.
- Extend the analysis to the elastic pre-stack domain which would provide much more information about fluid changes in the reservoir. The attributes  $V_p/V_s$  and  $\lambda\rho-\mu\rho$  appear to be more sensitive to fluid changes than the acoustic impedance.
- Independently of the approach to be applied, consider the option of reprocessing the seismic data to recover the low-frequency signal if no new acquisition is contemplated to be performed.
- Perform this analysis on real time-lapse data to reduce the uncertainties related with using ideal scenarios in seismic modelling experiments.

Acoustic impedance proved to be an excellent technique to interpret seismic data beyond the limitations of directly evaluates the seismic amplitudes. When the impedance contrast is considerable, this method presents low risk in assessing target zones. It is well known that careful considerations must be taken in the initial model as well as the wavelet. Errors in these parameters will be present in the final inversion result. Having more control in the inversion parameters warranty a success in the results especially when the reservoirs are challenged by limitations, such as: vertical resolution, low impedance contrast with surrounding formations, and poor data quality. Including the low-frequency component in the seismic data decreased uncertainties added from the initial model.

## REFERENCES

- Adam, L., Otheim, T., van Wijk, K., Batzle, M., McLing, T., and Podgorney, R., 2011, CO<sub>2</sub> sequestration in basalt: Carbonate mineralization and fluid substitution: 81<sup>st</sup> Ann. Internat. Mtg., Soc Expl. Geophys. Expanded Abstract, 2108-2113.
- Allan, J. A. and Rutherford, R. L., 1934, Geology of Central Alberta: Alberta Geological Survey, Report 30. Retrieved July 22<sup>nd</sup>, 2013: [http://www.ags.gov.ab.ca/publications/abstracts/REP\\_30.html](http://www.ags.gov.ab.ca/publications/abstracts/REP_30.html)
- Alshuhail, A., 2011, CO<sub>2</sub> Sequestration Site Characterization and Time-lapse Monitoring Using Reflection Seismic Methods: PhD. Thesis, Univ. of Calgary.
- Bachu, S., 2001, Screening and Ranking of Hydrocarbon Reservoirs for CO<sub>2</sub> Storage in the Alberta Basin, Canada: National Conference on Carbon Sequestration. US Department of Energy – National Energy Technology Laboratory.
- Bachu, S., Brulotte, M., Grobe, M., & Stewart, S. (2000). Suitability of the Alberta subsurface for carbon-dioxide sequestration in geologic media. Alberta Geological Survey, Earth Sciences Report. Edmonton: Alberta Energy and Utilities Board.
- Carbon Management Canada., 2013. Retrieved September 22, 2013: <http://www.cmc-nce.ca/events/gallery/>

- Chadwick A., R. Arts., O. Eiken, P. Williamson., and G. Williams., 2006, Geophysical Monitoring of the CO<sub>2</sub> Plume at Sleipner, North Sea: Advances in the Geological Storage of Carbon Dioxide, 303-314.
- Clarebout, J., 1983, Ground Roll and Radial Traces: Stanford Exploration Project Report, SEP-35, 43-53.
- Cooke, D. A. and Schneider, W.A., 1983, Generalized linear inversion of reflection seismic data: Geophysics, Vol. 48, p. 665-676.
- Core Lab Petroleum Services., 2013, Stratigraphic Correlation Chart. Retrieved August 9<sup>th</sup>, 2013: <http://www.landman.ca/pdf/CORELAB.pdf>
- Dix, H. C., 1955, Seismic velocities from surface measurements: Geophysics, **20**, 68-86.
- Dutta, T., Mavko, G., and Mukerji, T., 2009, Compaction trends for shale and clean sandstone in shallow sediments, Gulf of Mexico: The Leading Edge, **28**, No. 5, 590-596.
- Frailey, S., 2009, Methods for Estimating CO<sub>2</sub> Storage in Saline Aquifers: Energy, Elsevier Science Ltd, Oxford, **1**, 2769-2776.
- Gassmann, F., 1951, Uber die elastizitat poroser medien. Verteljahrss-chrift der Naturforschenden Gesellschaf , **23**, 1-23.
- Hampson-Russell., 2009, Hampson-Russell Assistant. Hampson-Russell Software Documentation. Hampson-Russell Software, A CGGVERTIAS Company.

- Henley D. C. and Gary F. Margrave., 2008, Gabor deconvolution: surface-consistent and iterative: Back to Exploration, Canadian Society of Exploration Geophysics (CSEG). Expanded abstract, 307-310.
- Henley, D. C., 2003, Coherent noise attenuation in the radial trace domain: Geophysics, **68**, No. 4, 1408-1416.
- Henley, D. C., 2011, Now you see it, now you don't: radial trace filtering tutorial: CREWES Research Report, **23**.
- Isaac, J. H. and Margrave, G. F., 2011, Hurrah for Hussar! Comparisons of stacked data: CREWES Research Report, **23**, No. 55.
- Isaac, J. H., Margrave, G. F., Deviat, M., and Nagarajappa, P., 2012, Processing an analysis of Hussar data low frequency content: CREWES Research Report, **24**.
- Kallweit, R.S. and L.C. Wood., 1982, The limits of resolution of zero-phase wavelets: Geophysics, **47**, 1035-1046.
- Lindseth, R. O., 1979, Synthetic sonic logs – a process for stratigraphic interpretation: Geophysics, Vol. 44, No. 1, p. 3-26.
- Lloyd, H. J. E., 2013, An Investigation of the Role of Low Frequencies in Seismic Impedance Inversion: M.Sc. Thesis, University of Calgary.

- Margrave, G. F., Lamoureux, M. P., Grossman, J. P., and Iliescu, V., 2002, Gabor deconvolution of seismic data for source waveform and Q correction: 72<sup>nd</sup> Ann. Internat. Mtg: Soc. of Expl. Geophys. Expanded Abstract, 2190-2193.
- Margrave, G. F., Mewhort, L., Phillips, T., Hall, M., Bertram, M. B., Lawton, D. C., Innanen, K. A. H., Hall, K. W. and Bertram, K. L., 2012, The Hussar low frequency experiment: CSEG Recorder, **37**, No. 07, 25-39.
- Michael, K., Bachu, S., Buschkuehle, B., Haug, K., & Talman, S., 2008, Comprehensive Characterization of a Potential Site for CO<sub>2</sub> Geological Storage in Central Alberta, Canada: American Association of Petroleum Geologists Manuscript, **40**.
- Moradi, S., and Lawton, D. C., 2013, Theoretical detectability of CO<sub>2</sub> at a CCS project in Alberta: 83<sup>rd</sup> Ann. Internat. Mtg., Soc Expl. Geophys. Expanded Abstract, 3475-3479.
- Mossop, G. D., Shetsen, I (comp.), 1994, Geological Atlas of the Western Canada Sedimentary Basin. Retrieved August 14<sup>th</sup>, 2013: [http://www.ags.gov.ab.ca/publications/wcsb\\_atlas/atlas.html](http://www.ags.gov.ab.ca/publications/wcsb_atlas/atlas.html)
- Natural Resources Canada., 2013, Atlas of Canada - Alberta. Retrieved August 30, 2013, from Natural Resources Canada: <http://atlas.nrcan.gc.ca/site/english/maps/reference/provinceterritories/alberta>
- Oldenburg, D. W., Scheuer, T., and Levy, S., 1983, Recovery of the acoustic impedance from reflection seismograms: Geophysics, Vol. 48, No. 10.

Poulton, T.P., Christopher, J.E., Hayes, B.J.R., Losert, J., Tittlemore, J., and Gilchrist, R.D., 1994, Jurassic and lowermost Cretaceous strata of the Western Canada Sedimentary Basin. In: Geological Atlas of the Western Canada Sedimentary Basin. G.D. Mossop and I. Shetsen (comps.). Calgary, Canadian Society of Petroleum Geologists and Alberta Research Council, chpt. 18.

Project Pioneer., 2012, Retrieve October 18, 2013: <http://www.projectpioneer.ca/>

Project Pioneer., 2013, Retrieve October 18, 2013: [http://www.transalta.com/sites/default/files/Project%20Pioneer\\_Final%20Report\\_Executive%20Summary\\_2013.pdf](http://www.transalta.com/sites/default/files/Project%20Pioneer_Final%20Report_Executive%20Summary_2013.pdf)

ProMAX., 1997, a reference guide for the ProMAX geophysical processing software. Landmark, a Halliburton Company. Vol. 2.

Russell, B., and D. Hampson., 1991, Comparison of poststack inversion methods: 61St Annual International Meeting, SEG, Expanded Abstracts, 10, 876-878.

Sheriff, R. E., 2001, Understanding the Fresnel zone: Search and Discovery Article, N° 40014.

Sheriff, R.E., 2002, Encyclopedic Dictionary of Applied Geophysics: SEG, 4th ed.

Smith, D.G., 1994, Paleogeographic evolution of the Western Canada Foreland Basin. In: Geological Atlas of the Western Canada Sedimentary Basin. G.D. Mossop and I. Shetsen (comps.). Calgary, Canadian Society of Petroleum Geologists and Alberta Research Council, chpt. 17.

- Smith, D.G., Cameron, A.R., and Bustin, R.M., 1994, Coal resources of the Western Canada Sedimentary Basin. In: Geological Atlas of the Western Canada Sedimentary Basin. G.D. Mossop and I. Shetsen (comps.). Calgary, Canadian Society of Petroleum Geologists and Alberta Research Council, chpt.33.
- Sparlin, M., Meyer, J., Bevc, D., Cabrera, R., Hibbitts, T., and Rogers, J., 2010, Seismic analysis and characterization of a brine reservoir for CO<sub>2</sub> sequestration: 80<sup>th</sup> Ann. Internat. Mtg: Soc. of Expl. Geophys, 2304-2308.
- STRATA user guide., 2009, Hampson-Russell Assistant: STRATA Theory. Hampson-Russell Software, a CGG Company.
- Switzer, S., Holland, W., Christie, P., Graf, G., Hedinger, A., McAnley, R., et al., 1994, Devonian Woodbend - Winterburn strata of the Western Canada Sedimentary Basin. Geological Atlas of the Western Canada Sedimentary Basin . (G. Mossop, & I. Shetsen, Eds.) Canadian Society of Petroleum Geologists and Alberta Research Council.
- Vera, V. C., 2012, CO<sub>2</sub> Seismic modelling of CO<sub>2</sub> in a sandstone aquifer, Priddis, Alberta: M.Sc. Thesis, Univ. of Calgary.
- Wang, Z., Cates, M., & Langan., 1998, Seismic monitoring of a CO<sub>2</sub> flood in a carbonate reservoir: A rock physics study: Geophysics, 63, 1604-1617.
- WASP., 2010, Wabamun Area CO<sub>2</sub> Sequestration Project, University of Calgary. Retrieved July 3<sup>rd</sup>, 2013: [www.ucalgary.ca/wasp](http://www.ucalgary.ca/wasp)

- Watts, N., 1987, Carbonate sedimentology and depositional history of the Nisku Formation in south-centra Alberta. In F. Krause, & O. Burrowes (Eds.), Devonian lithofacies and reservoir styles in Alberta (pp. 87-152). 2nd International Symposium of the Devonian System: 13th CSPG Core Conference.
- Widess, M.B., 1973, How thin is a thin bed?: *Geophysics*, **38**, 1176-1180.
- Williams, G.D., 1963, The Mannville Group (Lower Cretaceous) of central Alberta: *Bulletin of Canadian Petroleum Geology*, **11**, 350-368.
- Wood, J.W. and Hopkins, J.C., 1989, Reservoir sandstone bodies in estuarine valley fill: Lower Cretaceous Glauconitic Member, Little Bow Field, Alberta, Canada: *American Association of Petroleum Geologists, Bulletin*, **73**, 1361-1382.
- Yilmaz, Ö., 2001, *Seismic data analysis (Vol. I and II)*. Tulsa: Society of Exploration Geophysicists: *Investigations in Geophysics*, No. 10.